Analysis of Dynamic Surface Instabilities in Soft Hydrogel Cylinders Subject to Laser-Driven Shock-Loading

by

Daniel Pickard

B.S., Massachusetts Institute of Technology (2020)

Submitted to the Department of Aeronautics and Astronautics
in partial fulfillment of the requirements for the degree of

Master of Science in Aeronautics and Astronautics

at the

MASSACHUSETTS INSTITUTE OF TECHNOLOGY

May 2022

Author .....
Department of Aeronautics and Astronautics
May 17, 2022

Certified by .....
Raúl Radovitzky
Professor of Aeronautics and Astronautics
Thesis Supervisor

Accepted by .....
Jonathan P. How
R. C. Maclaurin Professor of Aeronautics and Astronautics
Chair, Graduate Program Committee

Analysis of Dynamic Surface Instabilities in Soft Hydrogel Cylinders Subject to Laser-Driven Shock-Loading

by

Daniel Pickard

Submitted to the Department of Aeronautics and Astronautics
on May 17, 2022, in partial fulfillment of the
requirements for the degree of
Master of Science in Aeronautics and Astronautics

Abstract

Soft materials subject to both static and dynamic loading are known to exhibit a variety of mechanical instabilities which may lead to intricate surface deformation patterns. In particular, creases and wrinkles have been found to play an important role in the morphogenesis of soft tissues and tumor growth. Soft matter instabilities are also relevant to a number of manufacturing and engineering applications such as the fabrication of microlenses, and the development of soft robots, actuators and flexible electronics. Static instabilities in soft matter have been well studied theoretically, and they are known to result from bifurcations of equilibrium due to loss of convexity of the nearly-incompressible elastic strain energy function in the large deformation range. Under dynamic loading, soft solids exhibit many instabilities that are well known in fluids, including Rayleigh-Taylor, Faraday and Richtmyer-Meshkov instabilities.

This thesis is concerned with the analysis and mechanistic explanation of a new elastodynamic instability that was recently discovered at MIT. Laser-driven experiments performed at the MIT Institute for Soldier Nanotechnologies have demonstrated undulations along the surface of pressurized cylindrical specimens of soft hydrogels which develop on an intermediate timescale in between what is expected from classic static and dynamic instability mechanisms. In contrast to prior work, the novel instabilities have been observed only along external, as opposed to internal, soft solid boundaries. The new instabilities have not been observed in experiments using pure water and appear to be a unique and novel phenomenon. Motivated by these intriguing differences between the new observations and instabilities considered in the past, we aim to develop a theoretical and numerical framework geared towards understanding the fundamental dynamics leading to the complex mechanical deformations discovered at the Institute for Soldier Nanotechnologies. Among the insights obtained, it is found that the ability of a soft material to sustain large tensile hydrostatic stresses plays a pivotal role in generating the new surface undulations. The observation of tension-driven, shock-induced surface instabilities in hydrogels is indicative of hydrogel's enhanced resistance to high strain rate cavitation when com-

pared to pure water and may be of technological interest to a number of soft matter applications such as the design of protective equipment or the development of impulse resistant sealants, insulators and adhesives.

Thesis Supervisor: Raúl Radovitzky
Title: Professor of Aeronautics and Astronautics

Acknowledgments

First, I would like to express my deepest gratitude to my advisor Professor Raúl Radovitzky, for his encouragement, guidance and support. His passion for engineering and commitment as a mentor and educator are inspirational. Thank you Raúl for believing in my potential and helping me set and reach higher goals in research and life.

I would also like to thank the past and current members of the Radovitzky Research Group including Anwar Koshakji, Professor Bianca Giovanardi, Christopher Quinn, Giulia Pozzi, Grégoire Chommette, Michelle Xu, and Zhiyi Wang for making the group a fun and collaborative environment. My thanks also go to my collaborators at the MIT Institute for Soldier Nanotechnologies: Jet Lem, Dmitro Martynowych, Shaoting Lin, Professor Keith Nelson and Professor Xuanhe Zhao for their invaluable experimental work and guidance in this endeavor. I am grateful for my peers in the Department of Aeronautics and Astronautics as well as Marie Stuppard, Beata Shuster, Beth Marois and Professor Carmen Guerra-Garcia. I am thankful for their consistent patience, support and help, and am fortunate to have found such a strong and supportive community in the aerospace department at MIT.

Finally, thank you to my brothers Aaron, Joshua and David for your love and sense of humor and to my amazing parents for your constant encouragement and support. Both my parents have shown my brothers and me how to work hard and maintain a passion for learning and continuing education for which I am grateful. They have instilled in us the famous Jewish perspective on learning: ‘ it is not required that you complete the work, but neither may you refrain from it’ (Rabbi Tarfon, Ethics of the Fathers) which has been instrumental in shaping my approach to my studies and this thesis.

Contents

List of Figures

List of Tables

Chapter 1

Previous Research on Soft Material Interfacial Instabilities

Soft solids are characterized as possessing a small shear modulus compared to their bulk modulus. These materials are ubiquitous in nature where a wide array of soft biological tissues are found due to the high water content of living organisms. Mechanical studies of human skin for instance report poisson ratios of 0.48 which corresponds to a ratio of shear to bulk moduli or a 'compressibility ratio' of 4 % [1]. Many other naturally occurring materials have still smaller compressibility ratios. Engineered soft solids are also extensively used as sealants, insulators, bearings and adhesives [2–4].

Due to their lack of shear stiffness, it is common to find complex morphologies along the surface of soft solids. For instance, the formation of gyri and sulci in the cerebral cortex of the brain [5] results from mechanical instability due to the softness of cortical tissue and is illustrated schematically in Fig. 1-1. Wrinkles and folds can also form along the surfaces of other organs in humans [6] and animals [7]. Notably skin [8], esophagi and airways [9] frequently display wrinkles. Tumor growth can demonstrate complex surface morphology and shape changes due to the softness of cancerous tissues [10–12]. Surface wrinkles naturally arise in a variety of soft foods such as the morphology of baking dough which develops as it rises [13] Fig. 1-2. The familiar wrinkles on raisins, peas [14] and other dried fruits and vegetables have

also been widely studied theoretically and numerically. Engineered soft solids often demonstrate surface instabilities such as the solvent swelling induced wrinkles [15] or Schallamach wave surface patterns [16] shown in Fig. 1-3 which are often found near contact lines on rubber or elastomer surfaces.

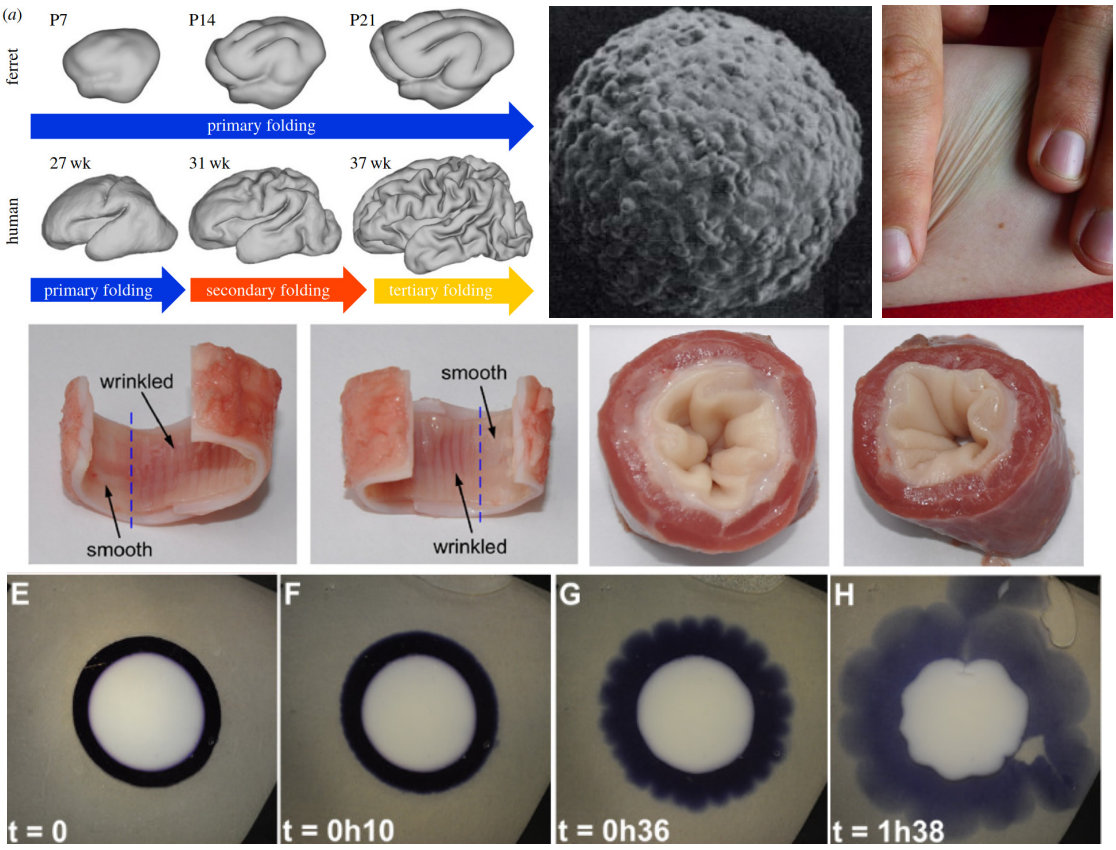

Figure 1-1: From left: illustration of brain sulci formation [5], morphology of spheroid cervical tumor [12], human skin wrinkles [8], bovine airway and esaphogus wrinkles [9], and artificial wrinkle formation which mimics typical morphology of tumor growth [11].

In addition to explaining curious surface patterns, the study of soft solid surface morphology provides many practical benefits. Manipulation of the geometric characteristics of surface deformation patterns in engineering materials can be exploited for the fabrication of microlens arrays [17, 18] and the development of soft robots [19], actuators [20, 21] and flexible electronics [22–24]. In the biological sciences, the study of elastic instability has provided a means to predict defects during the formation of optic vesicles [25]. Such defects in the optic cup are known to cause a variety of

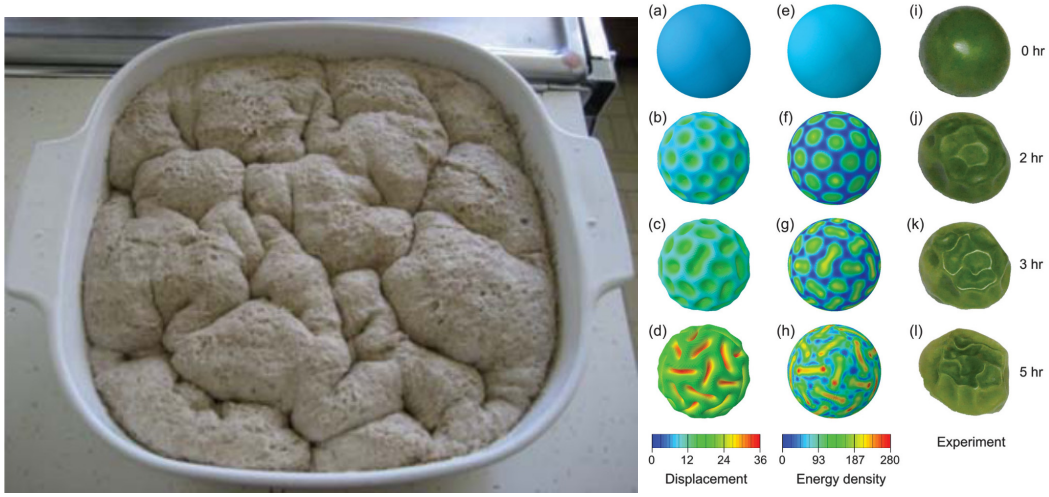

Figure 1-2: Left: Wrinkle formation along the surface of rising dough occurs due to differentials in humidity [13]. Right: computer and experimental investigation of the wrinkling of spherical fruits and vegetables such as peas as they dry [14].

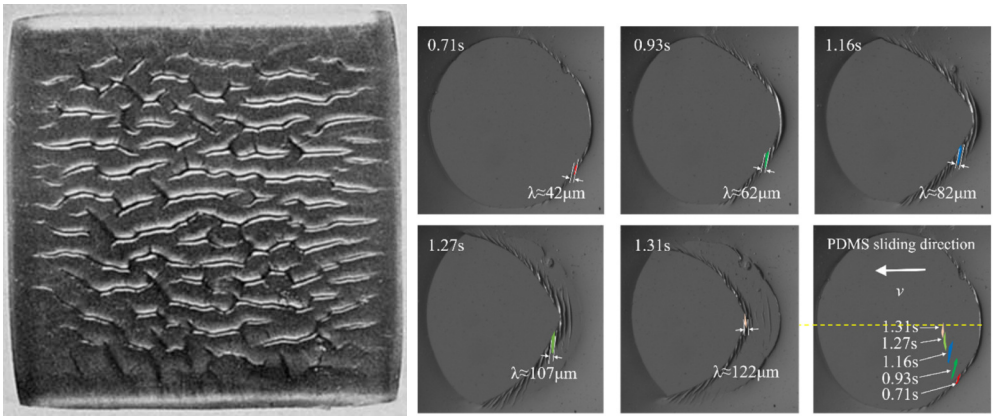

Figure 1-3: Left: swelling of rubber in hydrocarbon solvents induces surface morphology [15]. Right: Schallamach waves found where a sliding rigid body contacts a soft silicone, in this case Polydimethylsiloxane or PDMS [16].

important congenital eye disorders [26–28].

The complex and often multifaceted nature of soft solid surface instability mechanisms has motivated a number of mathematical and experimental studies over the past seventy years. Theoretical efforts to understand elastic surface instabilities date as far back as the 1950's when Biot studied the formation of wrinkles along the surface of an elastic half space under tangential compressive strain [29, 30]. Biot considered the incremental elasticity relations for an incompressible elastic half-space

with neo-Hookean deviatoric response. He found analytically that at a critical in-plane compressive strain the incremental shear modulus vanishes which implies a loss of stability of the homogeneous solution to the boundary value problem. The stress associated with this critical strain is 3.08 times the shear modulus which highlights that Biot type wrinkling instabilities occur when the shear modulus is small relative to the applied loads. From a theoretical viewpoint, Biot's instability can be viewed as resulting from a vanishing wave speed due to a loss of the incremental stiffness in a particular direction, but it is fundamentally a global bifurcation that results from the loss of convexity of the hyperelastic strain energy function due to the incompressibility constraint [31]. It is well known that real materials cannot possess a strain energy function which is both objective and convex [31–33] and that loss of convexity allows for the non-monotonic mechanical response [34] commonly observed in many soft solid and buckling instabilities [2, 35].

Wrinkle formation occurs in multiple settings due to different driving mechanisms such as differential changes in temperature, humidity, pH and electric field in addition to the mechanical compression studied by Biot [6]. These stimuli induce wrinkles by producing heterogeneous or anisotropic growth that leads to compressive stress tangential to the free surface. Homogeneous growth can also cause wrinkling if the elastic body is spatially constrained [11]. In addition to parallel sinusoidal wrinkles, complex two-dimensional wrinkling patterns have been described theoretically and observed in experiment. Thin films on soft, compliant substrates often wrinkle into herringbone patterns when the in-plane stress state is biaxial and compressive [36] Fig. 1-4. These more complex surface morphologies have been predicted by both numerical and analytical models [37]. Wrinkles can form on either flat or curved surfaces and can adopt a number of different morphologies such as: checkerboard, hexagonal, triangular and labyrinthine patterns [6].

Post-wrinkling, further morphological changes can occur along a free surface of a soft solid. For instance, period doubling of wrinkles occurs as soft solids are compressed beyond the initial bifurcation point. Period doubling causes the amplitude of alternating wrinkles to either grow or decay smoothly as the compression is increased

[38, 39]. The effect has been observed in soft PDMS substrates and has also been simulated numerically [6, 38]. This process may occur repeatedly and lead to period quadrupling [6, 38]. In contrast to the periodic and distributed nature of these effects, a thin film floating on a Newtonian fluid typically produces a single fold [6, 39].

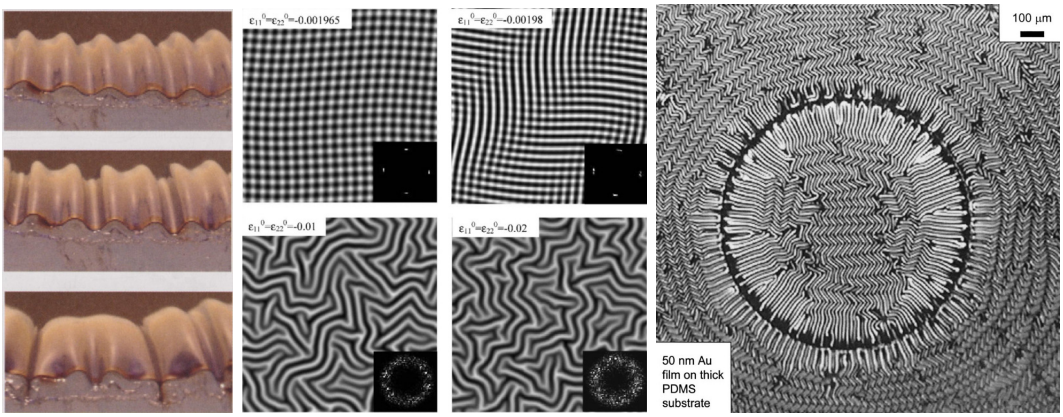

Figure 1-4: Period doubling [39], simulation of transition to herringbone and labyrinthine wrinkles [37], and experimentally observed herringbone patterns forming in thin gold films on PDMS substrates [36]

Contrary to the smooth post-bifurcation period doubling that may occur after wrinkling, crease formation does not typically evolve smoothly. A crease is defined by a sharp cusp at a free surface, located where the surface comes into contact with itself. Crease formation is sensitive to surface defects and does not occur after wrinkling. Furthermore, crease-induced deformations are spatially localized while wrinkle formation produces smooth and fairly uniform deformation throughout a material [6].

Surface instabilities can also appear along cylinders of soft solids subject to axial stretching. Such instabilities have been observed on rectangular and circular cylinders of different aspect ratios and are termed 'fringe' and 'fingering' instabilities [2, 35] Fig. 1-5. Fringe instabilities are manifested as surface undulations near the ends of a long cylinder under axial tension. Fingering instability develops as flatter specimens of soft solid are stretched and is manifested as surface undulations along the boundary near the middle of the cylinder. These instabilities arise due to the loss of convexity of the elastic strain energy in the large deformation regime. Numerical experiments

indicate that fringe instabilities develop under monotonic loading, while elastic fingering is a distinct phenomenon that yields more complicated load-displacement curves with a variety of snap-backs and snap-throughs [35]. Dynamic simulations of soft material axial stretching indicate that these classes of instabilities form in the quasistatic setting when the strain rate is smaller than unity. Experimental demonstrations of fringe and fingering instabilities use still smaller strain rates [2]. These instabilities do not depend strongly on the shear modulus so long as the hydrogel is sufficiently soft. It is important to emphasize that the fingering of elastic materials is different from the dynamic fingering that occurs between two viscous fluids of dissimilar properties.

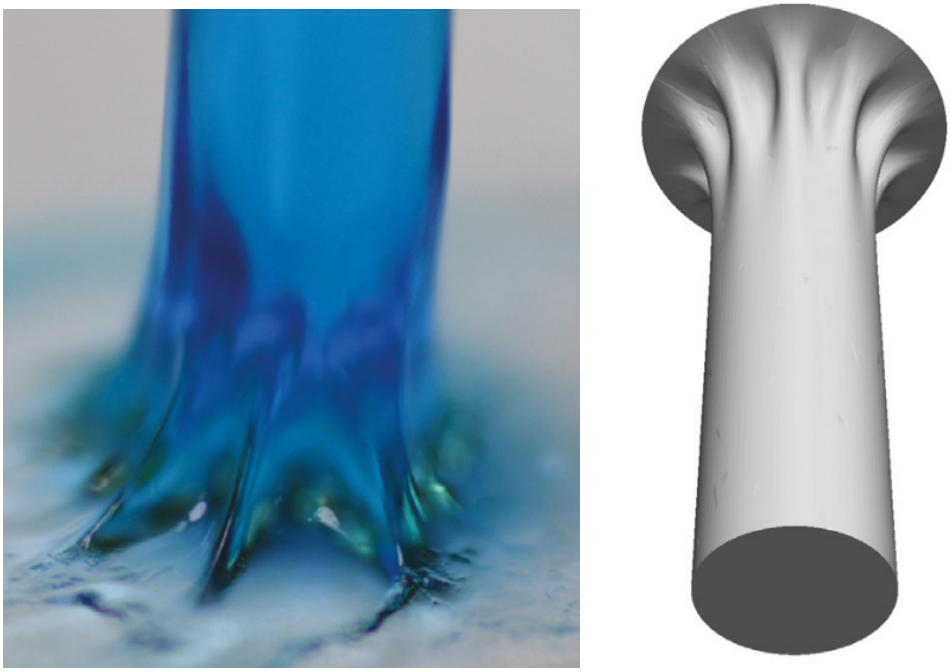

Figure 1-5: Fringe instability in experiment (left) and simulation (right) [35].

Another difference between soft solid instabilities and fluid instabilities is that some dynamic instability mechanisms in fluids can find equilibrium configurations in soft solids. The elastic Rayleigh-Taylor instability is a quasi-static version of the dynamic Rayleigh-Taylor instability of fluids which was discovered and explained by G. I. Taylor as a type of instability that occurs at the interface of two fluids subject to acceleration [40]. Taylor's original paper stated that an interface between two fluids ρ_a and ρ_b with sinusoidal corrugation of amplitude $a(t)$ and wave-number k will evolve

in the presence of acceleration $g(t)$ according to Eq. 1.1:

$$\frac{\partial^2}{\partial t^2}a(t) = kg(t)a(t)\frac{\rho_a - \rho_b}{\rho_a + \rho_b} \tag{1.1}$$

The relative density difference term $\frac{\rho_a - \rho_b}{\rho_a + \rho_b}$ is known as the Atwood number. For positive Atwood number and acceleration, corrugations will grow. In soft solids, this instability mechanism has been observed on the bottom side of unconstrained, hanging layers of soft matter Fig. 1-6. Gravity provides a constant acceleration $g(t)$ in the direction away from the heavier soft material and into the lighter air beneath the hanging layer. Elastic Rayleigh-Taylor instabilities often find equilibrium configurations that have hexagonal symmetry [41] though other morphologies have also been observed [42].

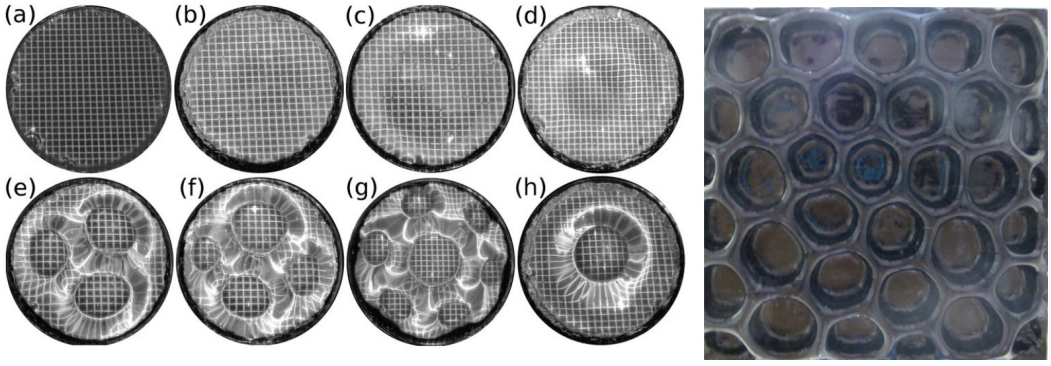

Figure 1-6: Left: View from below a soft layer as gravity pulls material down and induces elastic Rayleigh-Taylor instability [42]. Right: hexagonal symmetry in elastic Rayleigh-Taylor instability [41].

Another example of a fluid dynamic instability which finds equilibrium configurations in soft solids is the elastic Rayleigh-Plateau instability which causes a thin stream of liquid to break up into a sequence of droplets. In this instability mechanism, surface tension drives the breakup of fluid streams by pushing fluid away from narrow regions. The effect is described mathematically by the Young-Laplace equation shown in Eq. 1.2:

$$\Delta p = -\gamma(\frac{1}{R_1} + \frac{1}{R_2}) \tag{1.2}$$

The Young-Laplace equation relates the pressure difference Δp between the fluid

inside the cylinder and the surrounding atmospheric pressure to the interfacial surface tension γ and the two principal radii of curvature R_1 and R_2. For sufficiently thin cylinders of fluid, any slight variation in the radius of the cylinder can produce significant variation in ΔP. Thin necks in the fluid cylinder have small radii of curvature in the angular direction which produces high pressure in the neck and pushes fluid away from the thinned region. Eventually, this causes the cylinder to separate into two separate fluid domains. The dependence of Δp on the other radius of curvature in the axial direction prevents the growth of high wave-number instabilities. Consequently, fluid columns often break up into droplets of a typical size. Along thin columns of soft solid, surface tension effects can produce similar necking type instabilities, but the elastic stresses become significant as the neck thins and ultimately prevent the instability from breaking up soft solids. Instead, thin columns of soft solids typically form into undulating columns [43] Fig. 1-7.

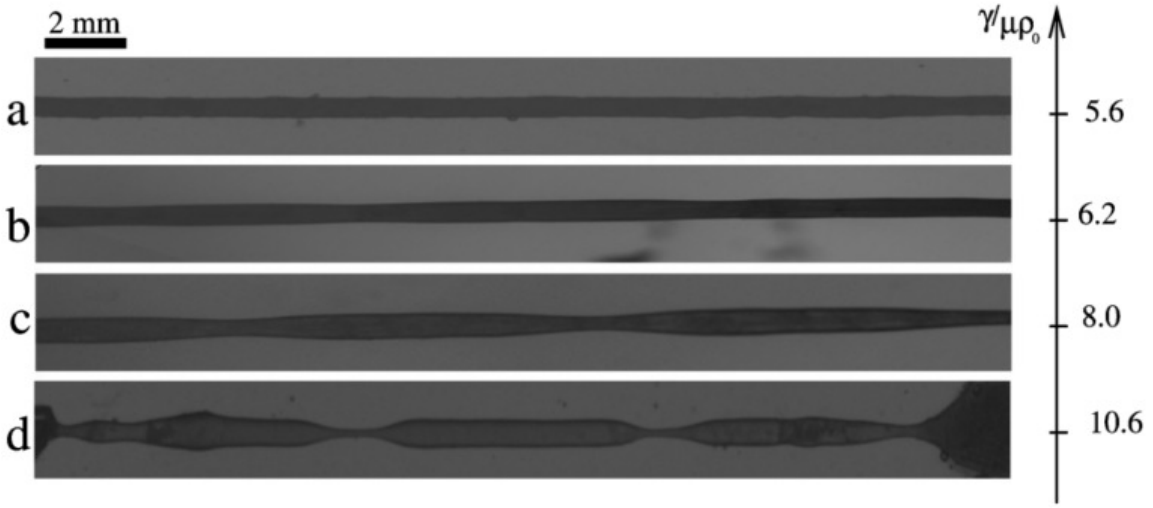

Figure 1-7: Elastic Rayleigh Plateau instability induces undulations along thin columns of soft materials [43].

Soft matter can exhibit true dynamic instability mechanisms as well. Recent research into soft solid dynamics has highlighted elastocapillary waves and Faraday instabilities in soft gels [44, 45]. These phenomena are dynamic counterparts to the Rayleigh-Plateau instability in that they are also governed by surface tension and

the Young-Laplace equation. Many of the other dynamic instability mechanisms of interest are related to extensions of the Rayleigh-Taylor mechanism. For instance, George Bell expanded on the Rayleigh-Taylor instability and derived analytical equations governing the evolution of small amplitude disturbances along incompressible inviscid fluid domains in the cylindrical and spherical setting [46]. Bell studied incompressible flows using the classic technique of considering velocity fields that are the gradient of a harmonic potential function. The divergence of these flow fields is the Laplacian of the harmonic function (zero by construction) which enforces the incompressibility constraint. Bell's findings were significant in that his results indicated the rate of instability growth scales with the domain curvature. He extended his analysis to the setting of compressible flow by assuming homogeneous volumetric strain. Interest in obtaining more realistic results for compressible flows led researchers to utilize numerical methods and computer simulation.

Robert Richtmyer used computer simulation to consider an extension of the Rayleigh-Taylor instability to settings when the interfacial acceleration $g(t)$ considered in Eq. 1.1 varies extremely rapidly and approaches an impulsive acceleration [47]. Gases moving through a shock wave experience violent accelerations which are well approximated by the assumption of a sudden and discrete change in the velocity field. Richtmyer started his analysis by considering Eq. 1.1 in the limit of $g(t) \propto \delta(t)$ which produces the following result:

$$\frac{\partial}{\partial t}a(t) = kGa(t_0)\frac{\rho_a - \rho_b}{\rho_a + \rho_b} \tag{1.3}$$

Here G represents the time integral of the acceleration field $\int g(t)\partial t$, which is finite for an impulsive acceleration. Taylor's theory predicts that the amplitude of a corrugation along an interface experiencing an impulsive acceleration should grow at a constant rate after the passage of a shock. Richtmyer-Meshkov instability as the shock-driven, impulsive limit came to be called is not necessarily governed by the above relation for the following reasons highlighted by Richtmyer.

First, the growth rate of the interface $\frac{\partial a}{\partial t}$ will be zero until there has been sufficient

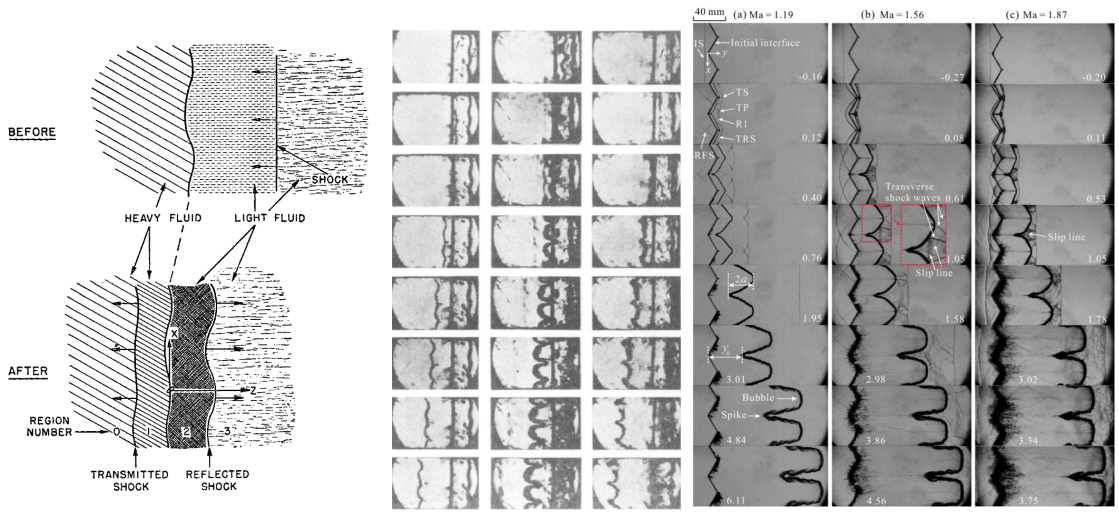

Figure 1-8: Left: Graphics from Richtmyer's 1960 paper describing shock induced instability of fluid interfaces [47]. Middle: Experimental results of Meshkov in 1969 [48]. Right: recent experimental study of Richtmyer-Meshkov instability along Air/SF_6 interface [49].

time for acoustic waves to travel from the crest to the trough along the corrugated interface. The shock passing the interface will affect the crest and trough in the same manner unless acoustic waves have had time to pass between the crests and troughs. Second, a shock passing through a fluid compresses it which causes the amplitude of a fluid interface to decrease immediately following shock transmission. Such a compressibility effect does not occur in classic Rayleigh-Taylor instability, and motivated Richtmyer to study the impulsive limit numerically in his 1960 paper. He concluded that Eq. 1.1 is actually the correct asymptotic expression for the rate of growth of a shocked, corrugated interface, but that there is ambiguity regarding if the densities in Eq. 1.3 should be the values just prior to, or just after the passage of the shock. His study showed that the right-hand side of Eq. 1.3 should be evaluated with the amplitudes and densities expected after the passage of the shock. For the gas dynamics problems of interest to Richtymer, this approach was found to be correct to within an error of 5 to 10 %. Neglecting the compressive effects of the shock and using the above relation as is led to errors an order of magnitude larger [47]. In essence, Richtmyer showed that the Atwood number after the passage of the shock can vary

significantly depending on the shock strength and the particular equations of state for the two fluids which has a dramatic impact on the evolution of perturbations along shocked interfaces. This dependence on the particular equation of state is absent in the incompressible Rayleigh-Taylor instability.

Experimental investigation of the problems considered by Richtmyer was reported in 1969 when Meshkov showed that the linear growth rate predicted in Richtmyer's study is correct to leading order Fig. 1-8 [48]. Crucially, he also observed that instability can develop in the case of shock waves passing through interfaces in either direction irrespective of the sign of the Atwood number. This had not previously been considered by Richtmyer and marks another fundamental difference between Richtmyer-Meshkov instability and Taylor type mechanisms. In the case of shock passage from a heavy into a light fluid, interfacial corrugations actually invert prior to continued growth which causes a 180 degree shift in the corrugation phase [50]. From a practical engineering perspective, this appears to be instability growth because the inversion of the corrugated interface occurs rapidly and is not consequential compared to the growth of large protrusions that develop after phase reversal. Phase reversal typically occurs if the Atwood number is negative. Richtmyer-Meshkov instability was originally considered in the setting of gas dynamics, but has been studied extensively in a variety of other geometries and materials [49, 51–59].

Additional relevant experimental studies of interface instability consider the dynamics of Newtonian and viscoelastic fluid droplets and bubbles [60, 61]. In particular, recent results by Ohl et al. on the study of laser-induced spherical Rayleigh-Taylor instability along fluid droplet surfaces [62] have shown that jets form as droplet surfaces accelerate radially inward. The authors note surface acceleration depends on the sign of the pressure gradient and that as droplets retract, the pressure gradient switches direction and begins to push the boundary outward which results in flipping of troughs along the surface into crests. This behavior is similar to the phase reversal of Richtmyer-Meshkov instability [50]. Additionally, Ohl et al. found that sufficiently large laser energy was needed to produce jet formation and that low Reynolds and Weber number droplets produced smaller wave-number instabilities. Aside from their

experimental observations, the authors presented an analytical model and a detailed numerical modeling approach based on finite volume methods for multiphase flows which captures some key features of their experiment. A number of other scholars have considered similar jet formation on the surface of other curved fluid domains [63–66], but this study is notable in that the authors describe oscillatory undulation growth and phase inversion as the fluid boundary acceleration changes sign.

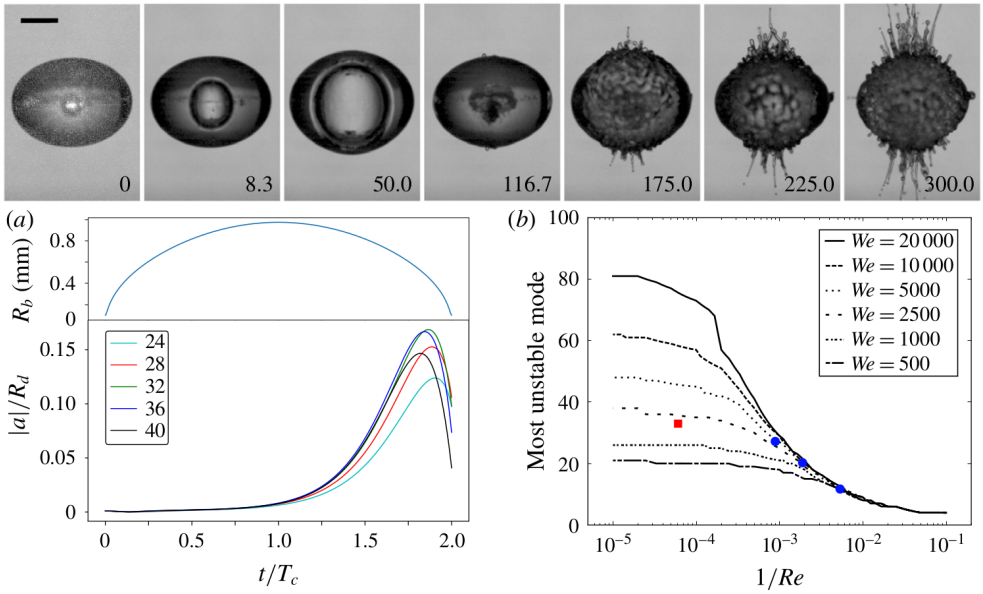

Figure 1-9: Top: Experimental results form Ohl et al. Bottom: Numerical results from Ohl at Al. Undulation amplitude growth over time and the most unstable wavenumber as a function of Reynolds and Weber number.

In contrast to compressible flows which are not easily studied analytically and require numerical or experimental methods to investigate in detail, the incompressible Rayleigh-Taylor instability has been the subject of continued mathematical investigation since Bell's extension to curved domains [46]. The approach of considering divergence free velocity fields (or isochoric deformation mappings) which arise as the gradient of a harmonic velocity potential has been used repeatedly in the literature. This approach leads to a number of well known results for the linear modal growth rates of corrugations along bubbles and droplets in inviscid fluids [67, 68], viscous fluids [69, 70] and more recently in elastic solids described in the Eulerian frame [71, 72]. It is worth mentioning that not all the literature on this topic is consistent and

follows this method identically. For instance, the recent publication by Franck et al. presented a linear stability analysis of cavities in soft solids, but considered only the evolution of purely radial (though non-symmetric) perturbations [73]. Their approach considered an incompressible flow field, but they did not analyze the full space of incompressible perturbations that are possible. In general, the incompressible flows or deformation mappings obtained from a potential function are not necessarily purely radial and this additional restriction on the perturbation mode shape led to disturbance evolution equations that are inconsistent with previous results [68, 69]. It is interesting to note that the approach considered by Franck et al. is not applicable to modeling interior domains which lack compressible inclusions. There are no nontrivial, isochoric, purely radial deformations of a disk or ball.

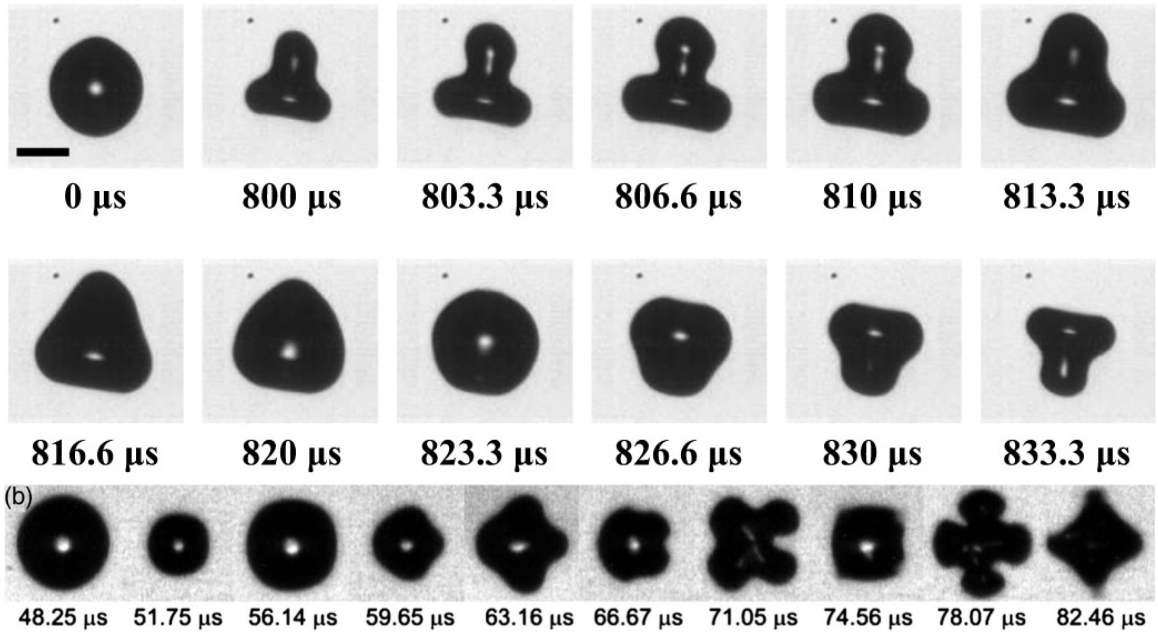

Figure 1-10: Top: Parametric instabilities in soft solids produced induced by ultrasound waves with amplitudes on the order of 10 kPa [74]. Scale bar is 100 μm. Bottom: Parametric instabilities in a 36 μm radius water bubble generated by approximately 10 times larger ultrasound wave amplitudes [75].

Instabilities described by linear modal growth equations are easily excited by low amplitude oscillatory forcing and are termed 'parametric instabilities.' Bubbles in water [76, 77] and soft solids [71, 72, 74, 75] have been shown to demonstrate the

parametric instabilities shown in Fig. 1-10. The wavelength of the forcing pressure signal used in this type of instability experiment significantly exceeds the length scale of the bubble so that pressure waves do not interact or scatter off the bubble. These instabilities are excited using signals with amplitude below 10 kPa in soft solids though larger amplitudes have been used in pure water. Typically these instabilities are categorized as distinct from the Rayleigh-Taylor type mechanisms [72, 76], but they are described mathematically by assuming periodic motion with disturbances governed by linear evolution equations similar to Taylor's Eq. 1.1. A Mathieu equation follows from these assumptions with nontrivial solutions described by Floquet theory [72, 78, 79], however, the underlying physics of parametric instabilities is ultimately based on similar mechanics to Rayleigh-Taylor mechanisms.

1.1 New Instabilities Observed in Laser-Driven Shock Experiments

Since the pioneering work of Biot, a wide variety of static and dynamic surface instability mechanisms have been considered. Surface instabilities can lead to either bifurcations of equilibrium or complex dynamical responses that exhibit surprising asymmetry or inhomogeneity. Soft solids in the strongly nonlinear shock-loaded regime, however, have received comparatively little attention. This thesis is concerned with a new class of instability that arises along soft solid boundaries due to strongly nonlinear pressure loading. The new instabilities were first demonstrated in recent experiments using a new approach proposed by Professor Keith Nelson's Research Group at MIT for the study of material response to large amplitude pressure waves on small length scales [80, 81]. In this experimental approach, a circular converging geometry is used to focus wave energy and allow for direct visual observation of material response over a large pressure range. Prior studies using this experimental setup have investigated shock propagation and cavitation growth in thin layers of water [82]. The particular experimental setup considered in this thesis is depicted schematically in Fig. 1-11. It

is a 50 μm-thick specimen of the soft hydrogel sandwiched between two 300 μm-thick glass plates.

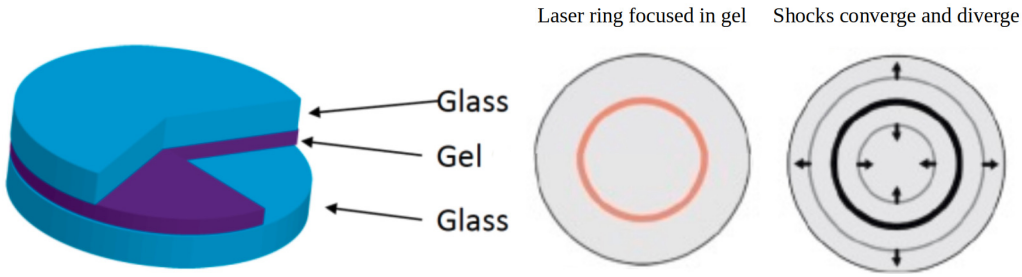

Figure 1-11: Left: schematic of hydrogel specimen sandwiched between glass plates. Center: detail of the initial circular 180μm-diameter laser ring. Right: waves emanated from laser-ablated ring.

The particular hydrogel used in these experiments was prepared by mixing 10 ml aqueous solutions of 12% wt. acrylamide (A8887 Sigma-Aldrich), 5% wt. Epson 522 printer ink, 2.5% wt. sodium alignate (A2033 Sigma-Aldrich), 0.023 % wt. N,N-methylenebisacrylamide (146072 Sigma-Aldrich) and 0.043% wt. ammonium persulphate (A3678 Sigma-Aldrich) and 0.03% wt. N,N,N',N'-tetramethylethylenediamine (T9281 Sigma-Aldrich). The mixture was poured onto a glass slide and covered with a second slide. Crosslinking of the polyacrylamide network was induced using 254 nm UV light exposure with an energy deposition rate of 6 W/m^2 for one hour. The N,N-methylenebisacrylamide acted as the crosslinker. Ammonium persulphate acted as a thermal initiator. N,N,N',N'-tetramethylethylenediamine was used to accelerate the crosslinking. This hydrogel mixture has been studied previously in the quasistatic setting [83]. The printer ink was needed to absorb the laser energy that generates shock waves.

Pressure loading was induced by a laser pulse of 8 ns duration containing 230 μJ of energy focused on a 180 μm-diameter ring of the specimen using the experimental setup described in [80]. The laser energy melts material along the boundary of the cylinder of hydrogel inside the ring and produces an intense pressure wave along the circumference that propagates towards the center. A second, diverging wave also moves outwards away from the ring, but the region of interest is on the interior of

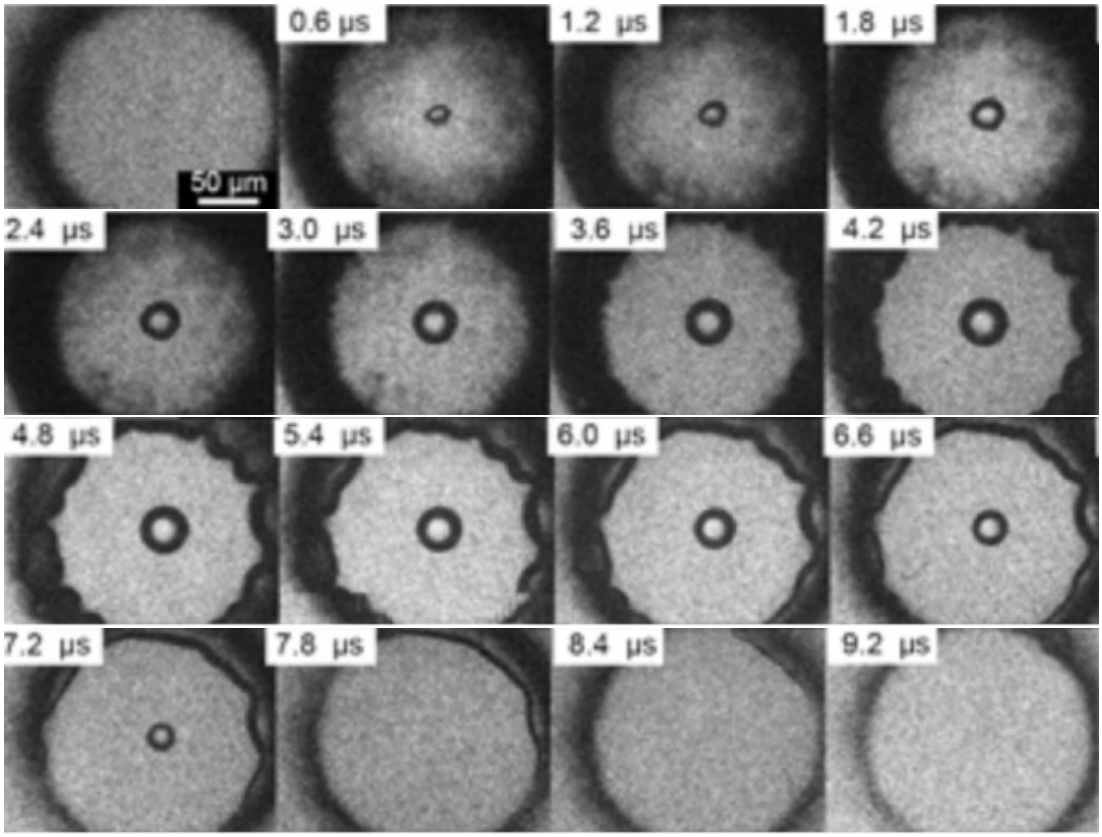

Figure 1-12: Time sequence of images obtained in laser-shock experiment on hydrogel. Pronounced unstable deformation patterns appear on the surface at some time between 2.4 and 3.0μs.

the ablation zone. Soft material-laser interactions have been studied for material characterization purposes via inertial cavitation [84, 85], but typically these studies use circular or spherical cavities. The approach developed at the MIT Institute for Soldier Nanotechnologies is unique in the use of a cavity with toroidal topology confined between stiff glass slides. In particular, this approach separates the elastic layer into two distinct domains, which is different from the typical method of producing circular or spherical laser ablation zones inside a single elastic body [73, 84, 85].

A high-frame-rate camera (SI-LUX640, Specialized Imaging) was used to acquire sixteen images spaced equally in time. As an illuminating probe, a 640 nm wavelength laser (Cavilux, Cavitar Ltd) of 30 μs pulse duration, which is longer than the total time required to acquire the sixteen frames with the high-frame-rate camera. Fig. 1-12 shows images obtained with a spacing in time of 0.6μs.

Experimental results obtained at the ISN are presented in Fig. 1-12 and clearly depict the new class of surface instability. In the first frame at $t = 0$, a dark ring along the laser ablated zone is clearly visible. High temperature gases and plasma absorb light and appear dark, obscuring the view in this region. At $t = 0.6$ μs, an elliptical cavitation bubble is apparent in the center of the specimen. Cavitation is a consequence of dilatational stress exceeding the tensile strength of the gel after the shock initially focuses and begins to diverge [82]. This bubble grows to a radius on the order of approximately 25 μm over the next 3.6 μs. At 3.0 μs, the ablated zone has cooled off and surface undulations emerge along the sides of the cylindrical specimen. The undulations look sharper and larger between 4.2 and 6.0 μs, but they do not seem to move noticeably along the boundary. By 6.6 μs, only the largest eruptions along the boundary are still visible, and the high wave-number instabilities have all but disappeared. Simultaneously, between 4.2 and 4.8 μs the central cavitation bubble retracts. By 7.8μs, the bubble has vanished leaving the center of the domain visibly undamaged. At no time during the course of the experiment are undulations observed along the external boundary of the darkened, laser ablation zone. Additional experimental results obtained using varying laser pulse energies and temporal spacing between the images are presented in appendix C. Also included are results from an identical experiment using pure water. Generally, hydrogels exhibit interesting boundary undulations of the kind shown in Fig. 1-12, but pure water does not.

The images shown in Fig. 1-12 are in stark contrast with previous research on analogous experiments in pure water [82]. The primary difference between the recent experiment and the prior experiments using water is that the recent experiments have replaced the 10 μm thick layer of water studied in the past with a thicker 50 μm layer of hydrogel. In addition, the new results use slightly weaker laser pulses and smaller domains. In [82], 500 μJ laser pulses were applied to domains of radius 95 μm, while in the recent experiments a variety of laser pulse energies were applied to slightly smaller 90 μm rings. Finally, the laser pulse duration of 8 ns is significantly longer than the 0.15 ns pulses considered previously. As a consequence of these differences, the images shown in Fig. 1-12 differ greatly from prior results reproduced in Fig. 1-13.

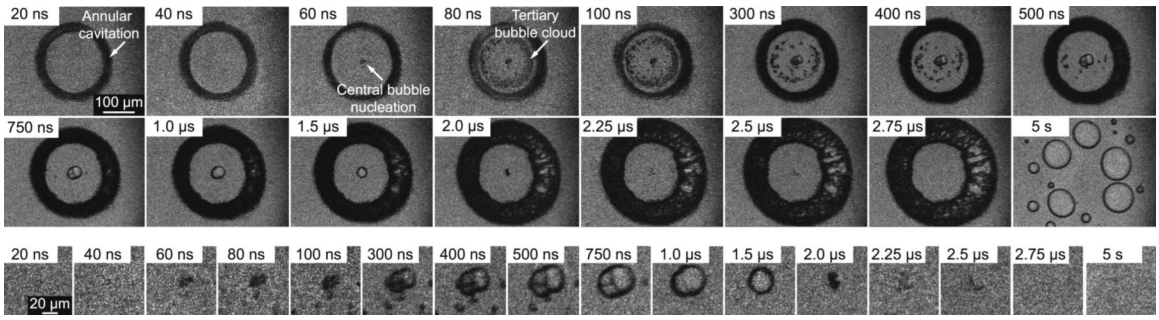

Figure 1-13: Experimental results from [82] obtained with a 500 μJ laser pulse.

In particular, in [82], the higher energy density causes the ablation ring to expand significantly. Additionally, the central cavitation bubble forms and decays in less than 2.5 μs, while in hydrogels the bubble grows more slowly and persists for longer. Finally, in water a 'tertiary bubble cloud' is formed along the interior ablation zone boundary which is absent in the hydrogel experiments.

When one analyzes the new experiment a few important features are evident. In this material the shear and bulk acoustic wave speeds vary widely and are given in terms of the density ρ, the bulk modulus κ and the shear modulus μ by: $c_{bulk} = \sqrt{\frac{\kappa}{\rho}} = 1414.2$ meters per second and $c_{shear} = \sqrt{\frac{\mu}{\rho}} = 2.236$ meters per second. The separation of scales in the acoustic wave speeds implies that the characteristic time for linear wave propagation across the experimental domain is also well separated. Bulk acoustic waves traverse this domain in a time of 127.27 ns while shear waves require 80.498 μs to cross the domain. Instability formation occurring on a timescale of microseconds as shown in Fig. 1-12 is slow compared to the timescale of acoustic pressure wave propagation, but is fast compared to the timescale of shear wave propagation. Nevertheless, the characteristic acoustic time for bulk wave propagation is not small enough to consider these quasistatic instabilities. Experimental measurements in pure water have confirmed that acoustic pressure waves propagate multiple times back and forth across the ablation ring during the first microsecond when undulations may be developing. The MIT Institute for Soldier Nanotechnologies has discovered a new impulse-driven instability which arises due to cycles of reflecting large amplitude pressure waves. The new instability is clearly different from both the typical

parametric instabilities that are found in the acoustic range and the variety of nonlinear, shock wave instabilities that occur in bubbles or laser vaporized fluids which form well before multiple wave reflections have occurred [86–88]. Additionally, the instability formation of the kind observed in the new experiments only occurs along the interior boundary of the laser ablation zone. Previous studies have found that gas pressure inside a cavity can cause quasi-static elastic fingering in soft solids [89, 90], but the one-sided nature of the undulation growth along the interior ablation zone boundary which is shown in Fig. 1-12 has not been reported. The intermediate timescale, single sided nature of undulation formation, and lack of reproducibility in pure water indicate a new type of dynamic instability which has not been observed previously.

Motivated by these intriguing and unexplained characteristics of the new phenomenon discovered at MIT, in this thesis we propose a mechanistic explanation for the essential features of this class of instabilities which will explain the major differences between the new experiment and prior studies. It will be shown that the instability formation arises due to a combination of cylindrical Rayleigh-Taylor mechanisms and Biot type wrinkle formation. In stark contrast to previous work, the latter, dominant mechanism is regulated by the material response under hydrostatic tension. To illustrate the mechanics of the new instability as well as its agreement with the observations shown in Fig. 1-12, a modeling approach for strongly nonlinear waves in soft solids is proposed. Starting from a large deformation, Lagrangian finite element framework which has been shown to adequately model the full range of material compressibility ratios including fluid-like behavior [91], a material frame indifferent shock capturing scheme is implemented which resolves shocks without spurious oscillations or impeding acoustic propagation section 2.1—section 2.3. The generality of the approach is demonstrated via simulations of the classic Richtmyer-Meshkov instability in soft solids in section 2.4. The computational framework is applied to the new experiments and excellent agreement with experimental observations is obtained section 3.1—section 3.2. Salient features of the numerical model that underscore the novelty of the instability mechanism are shown to be the development of

both compressive circumferential hoop stress and negative radial acceleration due to radial tension in the core of the computational domain section 3.3. A nondimensional parameter study of the instability is performed which reveals a critical dependence on the softening of the equation of state under hydrostatic tension section 3.5. We conclude by discussing in turn each of the novel features of the new instabilities and their relation to our computational results.

Chapter 2

Computational Framework for Modeling Shock Driven Instabilities in Soft Materials

Modeling approaches geared toward the study of shocked soft solids have been presented by a number of authors. On the analytical modeling side, shock dynamics of Newtonian fluids have been widely studied [92] and may be applicable to extremely soft materials with negligible shear stiffness. Shocks in fluids in converging, diverging geometries are discussed extensively in Barenblatt's textbook on scaling laws [93] and are known to have drastically different stability characteristics when converging or diverging. The simplest analytical approaches capturing this behavior describe diverging shocks using the dimensional analysis famously advanced by Taylor, but model converging, imploding shocks with a nonlinear eigenvalue problem. Additional analytical studies and discussions of shock dynamics in fluids of particular relevance to this thesis are found in Chapter 4 of Ben-Dor's textbook on shock reflection phenomenon which covers unsteady shock dynamics in detail [94].

For applications to materials possessing shear stiffness, the theory is also well-developed [95], though useful analytical models for engineering applications are more complicated than for shocks in fluids. Additionally, interest in the complex spatial temporal evolution of the new instabilities necessitates models which are capable of

predicting inhomogeneous and asymmetric waves and deformations. Numerical methods are preferable for this reason, and Eulerian finite volume methods have been used extensively within the fluid mechanics community for this purpose [62, 96]. Difficulties with the Eulerian depiction of solid mechanics arise when shear stiffness is incorporated. In Eulerian solid mechanics, the stress state depends on temporal integrals of the spatial gradients of the primal variable, which adds considerable complexity to either analytical [71] or numerical approaches. In some applications, it may be beneficial to consider such integral formulations of mechanical response, for instance variational approaches to the Navier-Stokes system may utilize integrals in time [97]. But for many practical applications, it is preferable to consider the Lagrangian picture which is also applicable even in the limit of no shear stiffness [91]. Difficulties encountered in the simulation of flowing solids or liquids using Lagrangian mechanics can be overcome by recourse to remeshing [98], but in this thesis deformations are limited to a range acceptably simulated on a single mesh which allows for easy and explicit integration of the mechanical response using the standard solid mechanics finite element procedures.

2.1 Governing Equations

The framework considered in this thesis is based on large deformation kinematics as described in [99, 100]. Material points in an undeformed body are mapped to a deformed configuration by the mapping $x = \phi(X, t)$. The deformation gradient is given in terms of the referential differentiation operator ∇_0 by Eq. 2.1:

$$\mathbf{F} = \frac{\partial \phi}{\partial X} = \nabla_0 u + \mathbf{I} \tag{2.1}$$

The compatibility constraint requires $\nabla \times \mathbf{F} = 0$. The equilibrium equation for large deformation dynamics is Eq. 2.2:

$$\nabla_0 \cdot \mathbf{P}(\mathbf{F}) = \rho a(t) \tag{2.2}$$

Here the acceleration field is $a(t) = \frac{\partial^2 u(t)}{\partial t^2}$, the referential density is ρ and $\mathbf{P}$ is the first Piola-Kirchhoff stress tensor. Conservation of angular momentum requires symmetry of the Cauchy stress given by $\sigma = J^{-1}\mathbf{P}\mathbf{F}^T$.

The material model for hydrogel utilized in this work is a compressible neo-Hookean hyperelastic model. It bears emphasis that many researchers have modeled extremely soft solids as idealized incompressible elastic bodies [71–74, 85, 101, 102]. More detailed descriptions of bubbles in soft solids often follow the approach of Keller and Miksis which provides a first order correction to the incompressible assumption that allows for energy transfer from acoustic pressure waves [84, 103–105]. When describing a material in either manner, the particular elastic equation of state which describes nonlinear volumetric material response is not significant because large volume changes do not occur. As discussed in chapter 1, the new experiments of interest involve strongly nonlinear pressure waves and significant volume changes which require an accurate equation of state to model appropriately. The volumetric constitutive response of the gel considered here is modeled using the Tait equation of state which is justified given the material's large water content ($\sim 85\%$) Eqs. 2.3–2.4.

$$W_{vol} = \frac{\kappa}{\bar{\gamma} - 1}\left(\frac{J^{-\bar{\gamma}}}{\bar{\gamma}} + J - \frac{\bar{\gamma} + 1}{\bar{\gamma}}\right) \tag{2.3}$$

$$P(J) = \frac{\partial W_{vol}}{\partial J} = -\frac{\kappa}{\bar{\gamma} - 1}\left(J^{-\bar{\gamma}-1} - 1\right) \tag{2.4}$$

Here J indicates the Jacobian of the deformation gradient $\mathbf{F}$. The two required model parameters κ and $\bar{\gamma}$ define the infinitesimal bulk modulus at the origin and the degree of stiffening in the nonlinear response. We adopt a bulk modulus κ at the origin of 2 GPa and a stiffening exponent $\bar{\gamma}$ of 6.15 [106], which correspond approximately to the volumetric response of water. To simulate the deviatoric response of hydrogel a neo-Hookean strain energy function is utilized Eq. 2.5:

$$W_{dev} = \frac{\mu}{2}\left(\frac{I}{J^{\frac{2}{3}}} - 3\right) \tag{2.5}$$

I is the first invariant of the right Cauchy-Green tensor $\mathbf{C} = \mathbf{F}^T\mathbf{F}$. Neo-Hookean

elastic models have been shown to effectively describe the quasistatic response in hydrogels [35, 41, 107–110]. The required model parameter is selected so that the shear modulus at the origin μ matches the stiffness of our specimen in its reference configuration at 5 kPa. The complete elastic strain energy function is given in terms of the Jacobian of the deformation gradient J and the first invariant of the right Cauchy-Green tensor I:

$$W = W_{vol} + W_{dev} = \frac{\kappa}{\bar{\gamma} - 1}\left(\frac{J^{-\bar{\gamma}}}{-\bar{\gamma}} - J + 1 + \frac{1}{\bar{\gamma}}\right) + \frac{\mu}{2}\left(\frac{I}{J^{\frac{2}{3}}} - 3\right) \tag{2.6}$$

From this hyperelastic energy function the first Piola-Kirchoff stress is defined as:

$$\mathbf{P} = \frac{\partial W}{\partial \mathbf{F}} = (-\frac{\kappa}{\bar{\gamma}+1}(J^{-(\bar{\gamma}+1)} - 1) - \frac{\mu}{3}(\frac{I}{J^{\frac{5}{3}}}))J\mathbf{F}\mathbf{C}^{-1} + \frac{\mu}{2J^{\frac{2}{3}}}\mathbf{F} \tag{2.7}$$

Note that the relation $\mathbf{F}^{-T} = \mathbf{F}\mathbf{C}^{-1}$ implies that all terms above are multiples of the deformation gradient or its inverse transposed.

2.2 Numerical Discretization

Detailed finite element simulations of shock loaded soft solids are conducted using our research code $\sum$MIT [111]. As is typical in finite element programs [112, 113], the compatibility equation and constitutive model are enforced strongly at each quadrature point while the equilibrium equation (Eq. 2.2) is enforced weakly using the following standard weak formulation.

$$\sum_{e=1}^{E} \int_{\Omega_0^e} \mathbf{P}(\mathbf{F}) \cdot \nabla_0 N_a^e + a(t)\rho_0 N_a^e dV_0 = \sum_{e=1}^{E} \int_{\Omega_0^e \cap S_2} \bar{T} N_a^e dS_0 \tag{2.8}$$

The space of the trial and test functions N_a^e is the same and is the space of continuous piece-wise linear functions that are linear over each element in the mesh.

The system of ordinary differential equations arising from the spatial discretization is integrated in time using second-order explicit Newmark time integration with mass lumping [114, 115]. The time integration scheme is implemented in $\sum$MIT, see

Eq. 2.9 - Eq. 2.11 below.

$$\mathbf{x}_i^{n+1} = \mathbf{x}_i^n + \Delta t \dot{\mathbf{x}}_i^n + \Delta t^2 \left[\left(\frac{1}{2} - \beta \right) \ddot{\mathbf{x}}_i^n + \beta \ddot{\mathbf{x}}_i^{n+1} \right] \tag{2.9}$$

$$\dot{\mathbf{x}}_i^{n+1} = \dot{\mathbf{x}}_i^n + \Delta t[(1-\gamma)\ddot{\mathbf{x}}_i^n + \gamma \ddot{\mathbf{x}}_i^{n+1}] \tag{2.10}$$

$$\ddot{\mathbf{x}}_i^{n+1} = \mathbf{M}_i^{-1}[\mathbf{f}^{ext} - \mathbf{f}^{int}]_i^{n+1} \tag{2.11}$$

where $\mathbf{M}$, $\mathbf{f}^{ext}$, and $\mathbf{f}^{int}$ are the lumped mass matrix, the external force, and the internal force, respectively. The subscript i represents the spatial discretization and the subscript n is the temporal discretization. The Newmark parameters γ and β are set to 0.5 and 0 respectively which reduces the Newmark equations to the explicit central difference scheme Eq. 2.12 - Eq. 2.14. A conventional predictor corrector scheme provides a simple implementation where the first the predictor evaluates Eq. 2.12 and Eq. 2.13 assuming that $\ddot{\mathbf{x}}_i^{n+1}$ is zero and then Eq. 2.14 is evaluated to obtain the correct accelerations $\ddot{\mathbf{x}}_i^{n+1}$. Eq. 2.13 is then corrected accordingly. A CFL number of one half is used in the selection of the integration time step to guarantee numerical accuracy and stability.

$$\mathbf{x}_i^{n+1} = \mathbf{x}_i^n + \Delta t \dot{\mathbf{x}}_i^n + \frac{\Delta t^2}{2} \ddot{\mathbf{x}}_i^n \tag{2.12}$$

$$\dot{\mathbf{x}}_i^{n+1} = \dot{\mathbf{x}}_i^n + \frac{\Delta t}{2}[\ddot{\mathbf{x}}_i^n + \ddot{\mathbf{x}}_i^{n+1}] \tag{2.13}$$

$$\ddot{\mathbf{x}}_i^{n+1} = \mathbf{M}_i^{-1}[\mathbf{f}^{ext} - \mathbf{f}^{int}]_i^{n+1} \tag{2.14}$$

2.3 Shock Capturing Scheme

As commonly required in simulations of shock-wave propagation, we add deviatoric artificial viscosity for shock stabilization using both linear and nonlinear viscosity [116]. The artificial viscosity scheme is a natural extension of the work by von Neumann and Richtmyer for shock capturing in fluids [117]. Viscosity is added based on a suitable scalar shock sensor that is chosen to satisfy material frame indifference. In this work,

viscosity is a function of the Jacobian of the deformation at each time step and is only added when $J = \det \mathbf{F}$ is decreasing. The artificial viscosity parameter ν_{art} is given at time step $n+1$ by

$$\nu_{art} = \frac{3}{4}\frac{h\rho}{J^{n+1}}(\bar{c}_2 a - \bar{c}_1 h \frac{\log(\frac{J^{n+1}}{J^n})}{\Delta t}) \tag{2.15}$$

Here the time step is Δt, the element length scale is h, the density is ρ and the acoustic wave speed is a. The viscosity parameters $\bar{c}_1$ and $\bar{c}_2$ are set to 1.0 and 0.1 respectively. Note that the acoustic speed a varies with the deformation. The contribution to the first Piola-Kirchoff stress provided by the viscosity, $\mathbf{P}_{visc}$, is computed from the velocity gradient $\mathbf{l} = \frac{\partial \mathbf{F}}{\partial t}\mathbf{F}^{-1}$ and the stretch tensor $\mathbf{d} = \frac{1}{2}(\mathbf{l}+\mathbf{l}^T)$ in the typical manner of linear viscosity.

$$\mathbf{P}_{visc} = 2J\nu_{art}\mathbf{d}_{dev}\mathbf{F}^{-T} \tag{2.16}$$

Here the deviatoric stretch is defined as $\mathbf{d}_{dev} = \mathbf{d} - \mathbf{I}\frac{tr(\mathbf{d})}{3}$. For stability purposes, the spatial velocity gradient utilized is not the typical spatial velocity gradient. $\mathbf{l}$ is computed from the current and previous deformation gradients $\mathbf{F}_{n+1}$ and $\mathbf{F}_n$ in the following manner:

$$\mathbf{l} = \frac{\mathbf{F}_{n+1} - \mathbf{F}_n}{\Delta t}\mathbf{F}_n^{-1} \tag{2.17}$$

In the $\sum$MIT implementation of constitutive models, the constitutive law is typically enforced implicitly at the current time step which would imply a calculation of the form $\mathbf{l} = \frac{\mathbf{F}_{n+1}-\mathbf{F}_n}{\Delta t}\mathbf{F}_{n+1}^{-1}$. By instead using the alternative spatial velocity gradient $\mathbf{l}$ defined by Eq. 2.17, the nonlinear dependence of the viscosity model on the current state is entirely due to the nonlinearity of the function $\nu_{art}(J)$ and geometric pull-back terms defined in Eq. 2.16 because $\mathbf{l}$ and hence $\mathbf{d}$ are linear functions of $\mathbf{F}_{n+1}$.

A final consideration for the purposes of numerical stability is that time independent loads along the domain boundary are stated in the deformed configuration. Dead loads stated in the reference configuration as is typical in finite element modeling led to spurious numerical instabilities when considering strong loads on soft elements.

Instead, the pressure loading along the boundary in the deformed configuration is computed by calculating the deformed area of all boundary faces and applying a force normal to that face proportional to the area times the pressure. This force is lumped one third to each node on the boundary face for first order triangular faces. This procedure allows the model to sustain far larger amplitude waves without numerical instabilities. In two dimensions the deformed edge length is considered instead of a face area and the force is lumped one half to each boundary edge node. Proper computation of the boundary normal vectors and edge areas or lengths should be performed during the computation of the mechanical residual in between the Newmark predictor and corrector defined by Eq. 2.11. For this thesis, these calculations are performed prior to the predictor. This nuance does not significantly alter the computational results and sufficiently enhances the ability of the computational framework to simulate large amplitude waves on soft elements when compared to the application of dead loads.

2.4 Application of Computational Framework to Soft Solid Richtmyer-Meshkov Instability

The framework considered in this thesis is based on Lagrangian mechanics which can accurately simulate a wide variety of solid and fluid mechanical responses [91]. The capabilities of the numerical approach are demonstrated by simulations of Richtmyer-Meshkov instabilities along shocked interfaces in three dimensions. The simulations model free surface interfaces which correspond to an Atwood number of negative one. As is typical in studies of this kind, an initial corrugation along the surface of the domain is introduced. In this case, the corrugation selected has spatial wave-numbers of 1 and 2 in the x and y directions respectively.

Snapshots of simulation results are presented in Fig. 2-1. At 10 ns, the shock capturing scheme stabilizes the shock as it advances towards the free surface. At 20 ns, the shock is midway through reflecting off the free surface. The troughs in the

interface have clearly interacted with the shock front and are placed under tension by the reflected wave. The dark blue regions of the free surface are under compression due to the shock front, and the peaks of the corrugations are unstressed because have not yet met the compression wave. By 30 ns, the Richtmyer-Meshkov instability has started to form. At this point in time, the four distinct red regions are visible on the surface of the domain where the four corrugation peaks were previously. These regions are under significant tension due to a geometric focusing effect which concentrates the reflected wave beneath the protrusions and pulls them downwards. In contradistinction, the four dimples in the free surface are under significant hydrostatic pressure and are being driven outwards by the instability. By 40 ns, these effects are clearly visible as sharp jets emerge from what were previously four dimples in the free surface. The jets in the bottom left and top right correspond to the locations of dimples in the reference configuration. It is noteworthy that the simulation framework presented here adequately captures a wide variety of complex dynamics not found in two-dimensional Richtymer-Meshkov instabilities. Sharper protrusions form along the high wave-number direction as compared to the lower wave-number dimension. Additionally, at 40 ns on the bottom left of the figure, a curved reflected pressure wave is apparent. The shock capturing scheme adequately captures the large negative pressures which form at triple points of curved three-dimensional shock fronts.

2.5 Extensions to the Computational Framework

A number of additional refinements to the model were considered in this research but have not proved necessary to capture the soft solid dynamic instabilities of primary interest. In particular, a variety of schemes were implemented to model the softening of the material response that is expected to occur in the vicinity of cavitation bubbles. It was found that setting the equation of state to be piecewise-defined so that the pressure becomes zero if J is excessively large produced unacceptable strain localization and led to a single large element. Attempts to regularize this behavior by defining a smooth equation of state which asymptotically approached zero as J

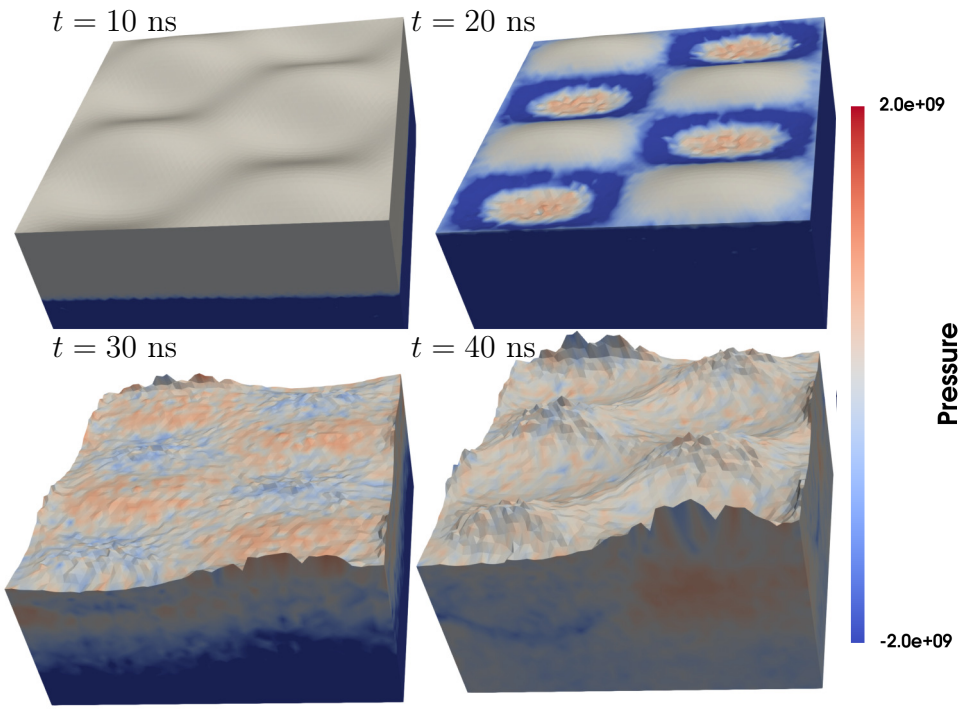

Figure 2-1: Three-dimensional Richtmyer-Meshkov instability using $\sum$MIT computational framework [111].

becomes large but reverts to the Tait equation under compression were unsuccessful. This approach also leads to strain localization because W is no longer convex in J.

In order to regularize strain localization, two similar phase field gradient damage models are implemented in $\sum$MIT. The first model is a modification to the formulation presented in [118] which is intended to model the quasistatic rupture of elastomeric materials. This approach describes a microforce balance that regulates the evolution of a damage variable d which varies between zero and one. The damage variable multiplies the stresses by a factor of $(1-d)^2$ to soften the constitutive response of an elastomeric material. The evolution equations of the model are given by the following equations Eq. 2.18 and Eq. 2.19.

$$\zeta \dot{d} = 2(1-d)H - \epsilon_R^f (d - l^2 \Delta d) \tag{2.18}$$

$$H = \max < W - \frac{\epsilon_R^f}{2} > \tag{2.19}$$

In this formulation, Macaulay brackets in Eq. 2.19 ensure that the history variable H remains nonnegative. In particular, when the elastic energy exceeds one half the material parameter ϵ_R^f, the history variable first becomes positive. The history dependent source term on the right side of Eq. 2.18 acts to increase damage when H is nonzero, i.e. in regions of the domain that have at some point in their history had elastic energies in excess of $\frac{1}{2}\epsilon_R^f$. The source term remains positive until total damage at $d = 1$ which drives stresses in these regions toward zero. The term $\epsilon_R^f l^2 \Delta d$ diffuses damage into nearby elements. Even undamaged elements with $H = 0$, may attain nonzero d due to diffusion. This effect ensures that sharp gradients do not appear in the damage variable and hence in the deformation.

A similar phase field model for brittle fracture was also described in [119]. In this approach the damage variable begins at one and declines to zero and multiplies the stresses by a factor c^2. The microforce balance equation presented in this paper is an elliptic equation with no dynamic terms and is given by:

$$2cW - G\epsilon \Delta c - \frac{G}{\epsilon}(1-c) = 0 \tag{2.20}$$

Both these damage models satisfactorily regularize strain localization and allow the stress field to decay when J becomes large. They do so by modeling the damage and softening response as nonlocal dissipative mechanisms which introduce additional characteristic length scales $l\sqrt{\epsilon_R^f}$ and $\sqrt{G\epsilon}$ respectively. These models explicitly account for the energy lost due to damage using ϵ_R^f and G respectively. They were implemented in $\sum$MIT using the following weak formulations Eq. 2.21 and Eq. 2.22.

$$\sum_{e=1}^{E}\int_{\Omega_0^e}\zeta\dot{d}-2(1-d)H+\epsilon_R^f d)N_a^e\partial V_0=-\epsilon_R^f l^2\sum_{e=1}^{E}\int_{\Omega_0^e}\nabla_0 d\nabla_0 N_a^e\partial V_0) \tag{2.21}$$

$$\sum_{e=1}^{E}\int_{\Omega_0^e}(2cW-\frac{G}{\epsilon}(1-c))N_a^e+G\epsilon\nabla_0 c\nabla_0 N_a^e\partial V_0=0 \tag{2.22}$$

These formulations are linear in d and c respectively and are easily solved in $\sum$MIT using either Crank-Nicolson or backward Euler time integration. Implicit time integration is necessary to ensure that suitably large time steps can be taken. The characteristic length scales in the model need to be larger than the element size (approximately five times larger) to smooth out the damage field sufficiently. Large characteristic length scales cause the maximum stable explicit time step for the integration of the parabolic equation Eq. 2.21 to be prohibitively small which necessitates the proposed implicit time marching schemes. In addition, the elliptic problem defined by Eq. 2.22 also requires solving a linear system. The linear systems arising from these discretizations were solved using the PETSc library [120] implementation of the conjugate gradient algorithm with an incomplete LU decomposition preconditioner. Data is passed between the mechanics and damage evolution equations in a staggered fashion so that only W and either d or c is passed between the two systems of equations. This approach was found to satisfactorily regularize the problem at the expense of increased simulation time.

In this thesis, extensive results from these refined models of the material response are not presented because they do not provide additional mechanistic insight into the essential features of the elastodynamic instabilities of interest. Nevertheless, the gradient damage models considered here can successfully regularize numerical insta-

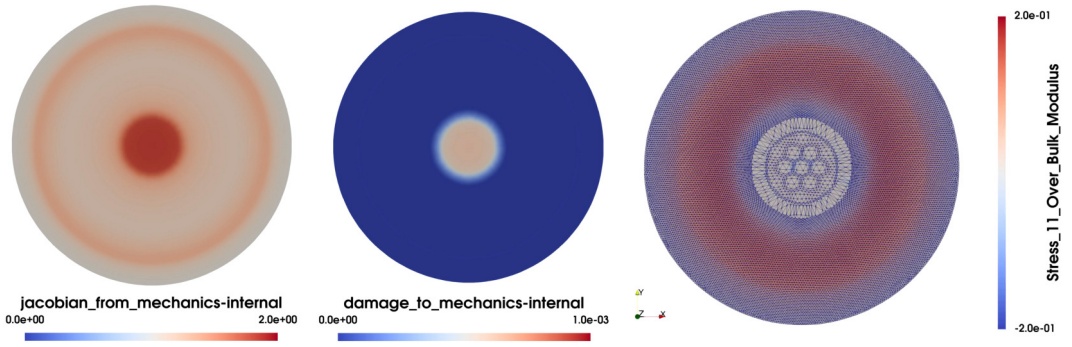

Figure 2-2: Left and Middle: illustration of coupled implementation in $\sum$MIT based on the model of Talamini et al. [118]. Right: illustration of strain localizing in seven distinct regions as the center approaches total damage using the model proposed in [119].

bilities which arise due to loss of hyperbolicity of the elastodynamic problem and are a promising area of research for modeling soft solid damage. In Fig. 2-2, the capability of these approaches to distribute damage into multiple elements and thereby smooth out strain localization is highlighted. Increasing the length scale of the damage equations will further regularize the damage zone but increases the computational cost. Besides these promising model refinements, there is an extensive body of literature describing additional improvements which might be added to describe the response of polymeric materials more accurately. Of particular interest, variationally consistent porous plasticity models have been used to model dissipative mechanisms and damage in soft solids and tissues [121]. Such an approach, or a more common rate dependent rheological model such as a Kelvin-Voigt [73, 85] or a Prony series, could easily be integrated into the computational framework and studied in the future.

Chapter 3

Application to Laser-Driven Shock Experiments

The aforementioned computational framework is used to simulate the new experiments in the following chapter. In order to model these shock driven experiments, one could contemplate describing the initial laser energy deposition process in detail using the equations of Magneto-Hydrodynamics [122, 123], but our interest in the evolution of the material deformation long after energy deposition motivates consideration of mechanical boundary conditions which reproduce the effects of laser ablation. The energy deposition process is represented by injecting mechanical energy into the finite element mesh using a pressure boundary condition. A variety of extensions to this first order model of the ablation cavity can be found in the literature on large amplitude bubble dynamics [105, 124, 125] though they are unnecessary for describing the instabilities of interest. Furthermore, the single sided nature of undulation formation indicates that the details of the energy deposition process can be safely neglected because the instabilities are related to dynamics inside the cylindrical domain. This approach is similar to prior studies of laser induced pressure waves which have mechanically modeled a laser energy deposition process using an updated Lagrangian scheme [80]. In this thesis, only the domain inside the circular ablation ring is simulated which allows for specifying the pressure wave using Neumann boundary conditions and alleviates the need to model the material in the ablation zone with

such an updated reference configuration.

3.1 Simulation Setup

In the present study, Gaussian profiles along with piecewise-defined linear and piecewise-defined quadratic profiles are considered for the particular functional form of the applied boundary pressure loading, however, it is found that the particulars of the boundary condition are insignificant because the wave rapidly steepens into the saw-tooth shock front which is typical of large amplitude pressure waves. For simplicity, the pressure pulse is taken to be a square wave with the duration t_{pulse} set to match the 8 ns duration of the applied laser excitation.

Accurate modeling of the new instability requires selection of an appropriate pressure pulse amplitude which excites a comparable dynamic response to what is observed in experiment. Specifically, the energy injected into the computational domain must be of a similar scale to the energy deposited by the laser. Applied laser energies considered in the new experiments ranged from 230 to 850 μJ, but no more than 50 % of the laser energy enters the interior of the ablation zone because the converging wave is assumed to have the same energy as the wave which diverges away from the ablation zone. In this thesis, the applied pressure pulse amplitude is tuned via an iterative procedure wherein simulations are performed using various pulse amplitudes until agreement is obtained with experimental results. Specifically, the evolution of the total energy within the simulation domain is monitored as a post-processing step and the boundary condition is selected to maintain approximate agreement with the energy injection expected in the new experiment. The following results are obtained with a pulse amplitude P_{pulse} of 2 GPa which deposits approximately 75 μJ of energy into the model Fig. 3-5. Additional studies of the impact of the applied pressure loading and hence the total model energy are presented in section 3.5.

Plane strain deformations are assumed within the simulation domain and the validity of this assumption is discussed in detail in appendix B. The particular spatial discretization considered in this section is a circular mesh with initial radius R_0 equal

to 90 μm consisting of 16,526 first order, triangular elements. The computational framework presented in chapter 2 is capable of modeling three-dimensional shocks in soft solids, but simpler two-dimensional calculations adequately demonstrate the instabilities from the new experiments. The particular discretization used here is generated using unstructured mesh generation software and is manually selected to avoid unintentional symmetry in the computational mesh [126].

3.2 Pressure Wave Dynamics and Eruption Formation

In this section detailed results of the numerical simulation are presented. To visualize the sequence of interesting events that take place during the various reflections of the stress waves, snapshots of the evolution of the relevant mechanical fields are presented at times of particular interest in Figs. 3-1—3-4. Upon loading, an initial hydrostatic stress wave develops and shocks up as it converges towards the center. Convergence of the wave in the center of the domain is achieved at 29 ns by which point the entire domain is in compression Fig. 3-1. Immediately afterwards, the stress wave diverges radially outwards and the center is placed under tension, a condition which persists until 202 ns. At 50 ns, the diverging pressure wave approaches the boundary while simultaneously the domain center remains in tension, as evidenced by the red center of the computational domain in Fig. 3-1. Counterintuitively, tension develops in the center even when the boundary is displaced inward. 'Tension tails' often follow planar shocks and induce tension on the order of 10 MPa [121]. In this converging-diverging geometry still larger stresses are attained.

At 55 ns, the shock wave reflects off the boundary, accelerating it radially outward. Subsequently, a tensile stress wave is reflected back towards the center of the domain Fig. 3-2. The reflected, tensile wave moves far slower than the shock because the bulk modulus decreases when under tension Fig. 3-3. It takes 147 ns for the tension wave to focus into the center of the domain while the shock traversed the same distance in

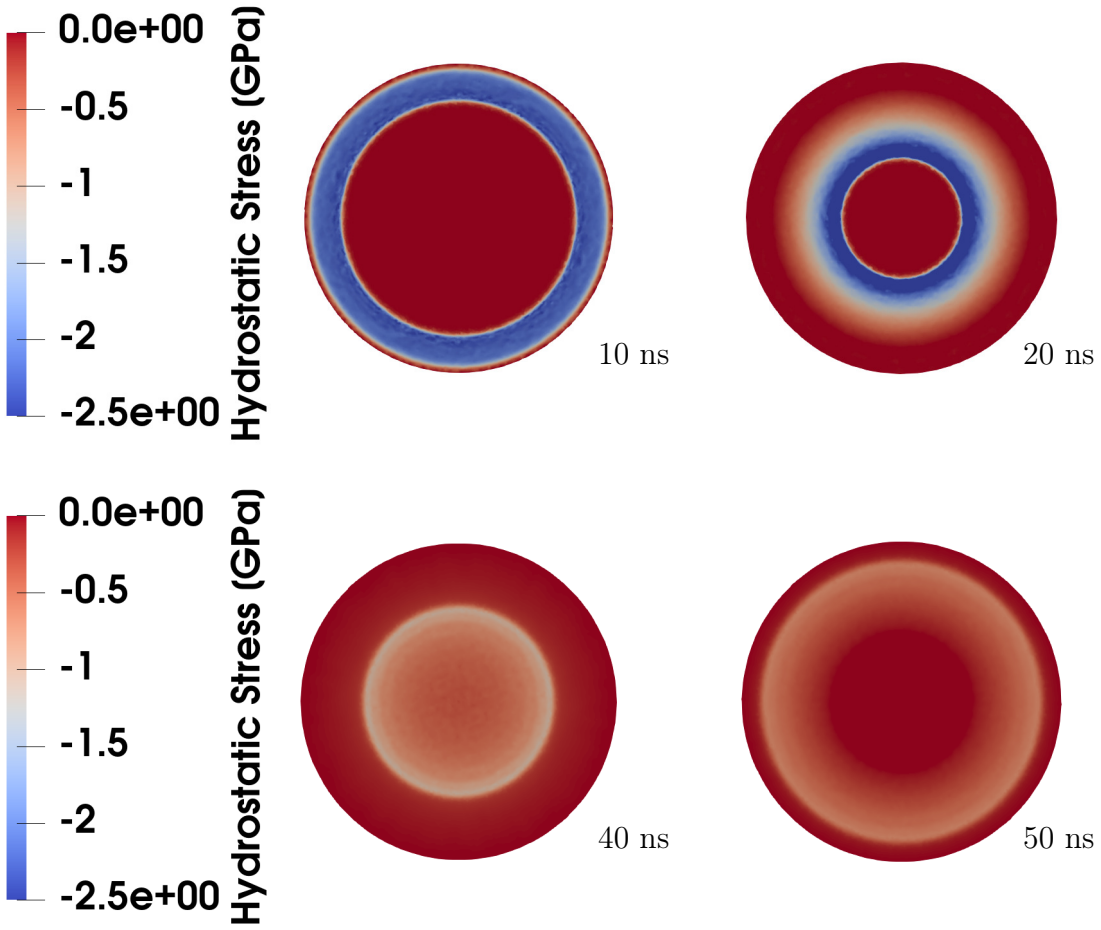

Figure 3-1: Hydrostatic stress contours on a scale from -2.5 to 0 GPa at 10, 20, 40 and 50 ns. The artificial viscosity scheme captures a steep shock front without numerical oscillations.

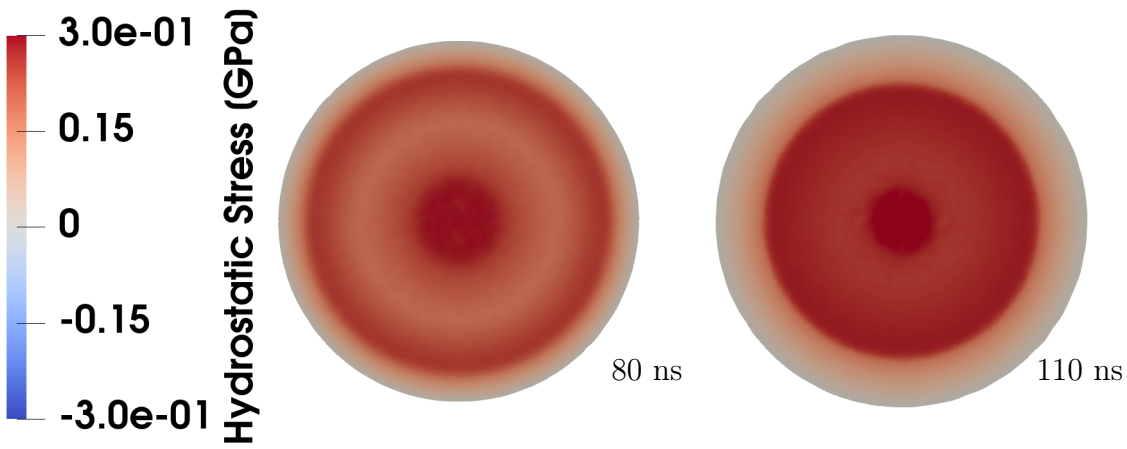

Figure 3-2: Hydrostatic stress contours plotted at times 80, 110 ns. on a ±0.3 GPa scale. The tensile wave travels radially inwards.

26 ns. The central tensile region and the reflection stress wave join into a common, shrinking tensile core. Outside this region the hydrostatic stress is still positive, but significantly smaller.

At 202 ns, the central tensile region contracts to a point and the continued motion of material inwards causes hydrostatic compression at the center which drives a second diverging shock wave. This concludes one complete cycle of pressure oscillations. Multiple additional cycles occur in the simulation until viscous effects damp them out. Subsequent shock reflections are found at 233, 428, 612, and 788 ns. The sequence of highly nonlinear vibrations leads to the formation of eruptions along the boundary of the computational domain Fig. 3-4.

A few features of the post-processed evolution of the energy distribution merit further discussion. Energy decays monotonically after loading due to dissipative effects, and it is apparent that the damping is increased when the domain contains a shock which results in periodic variation of the energy decay rate Fig. 3-5. Even as energy dissipates, salient features of this highly nonlinear mechanical system are evident in the total kinetic and elastic energy curves. For instance, the two minima in the elastic energy curves at 565 ns and 640 ns are closer in time than the minima around 640 ns and 745 ns. The two different periods correspond to elastic energy storage while the

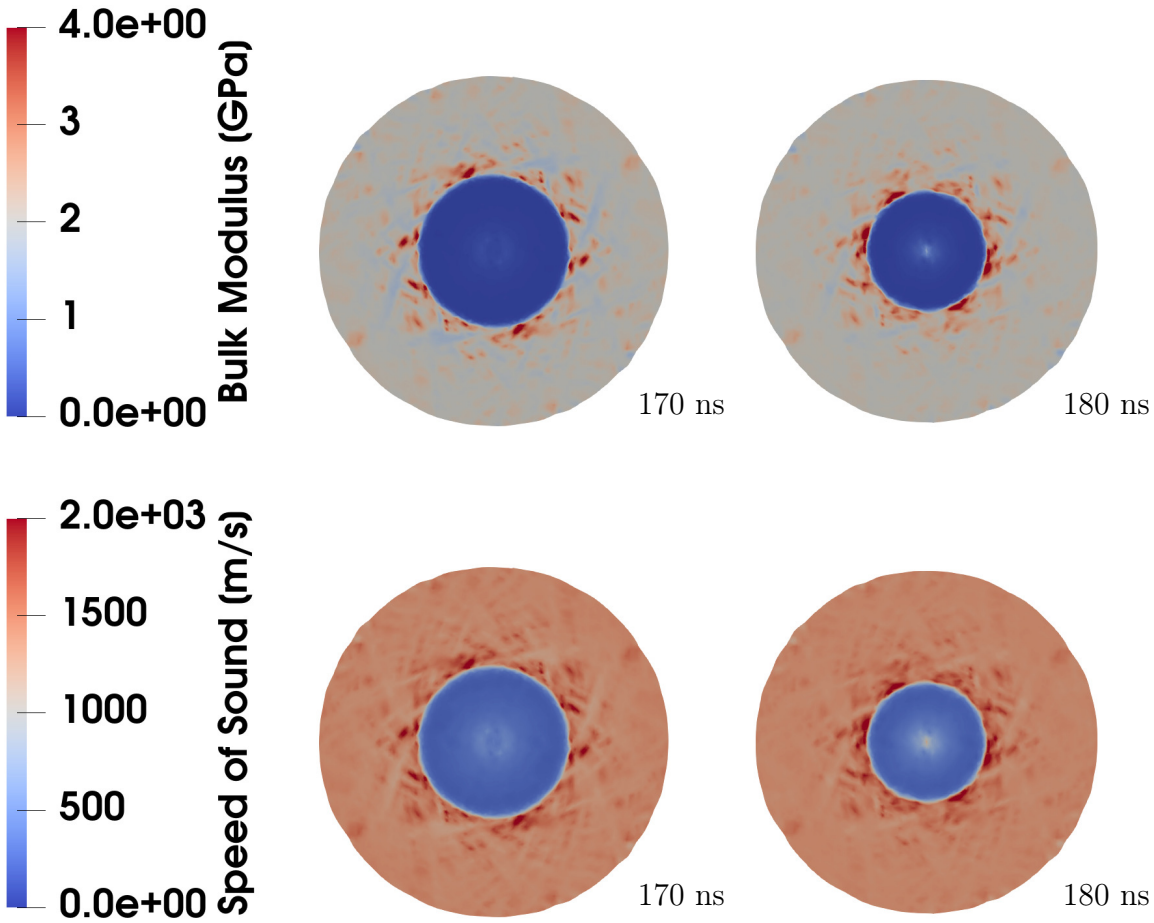

Figure 3-3: While under significant tension, the material model is highly nonlinear. The center of the disk softens significantly which leads to a decreased wave speed.

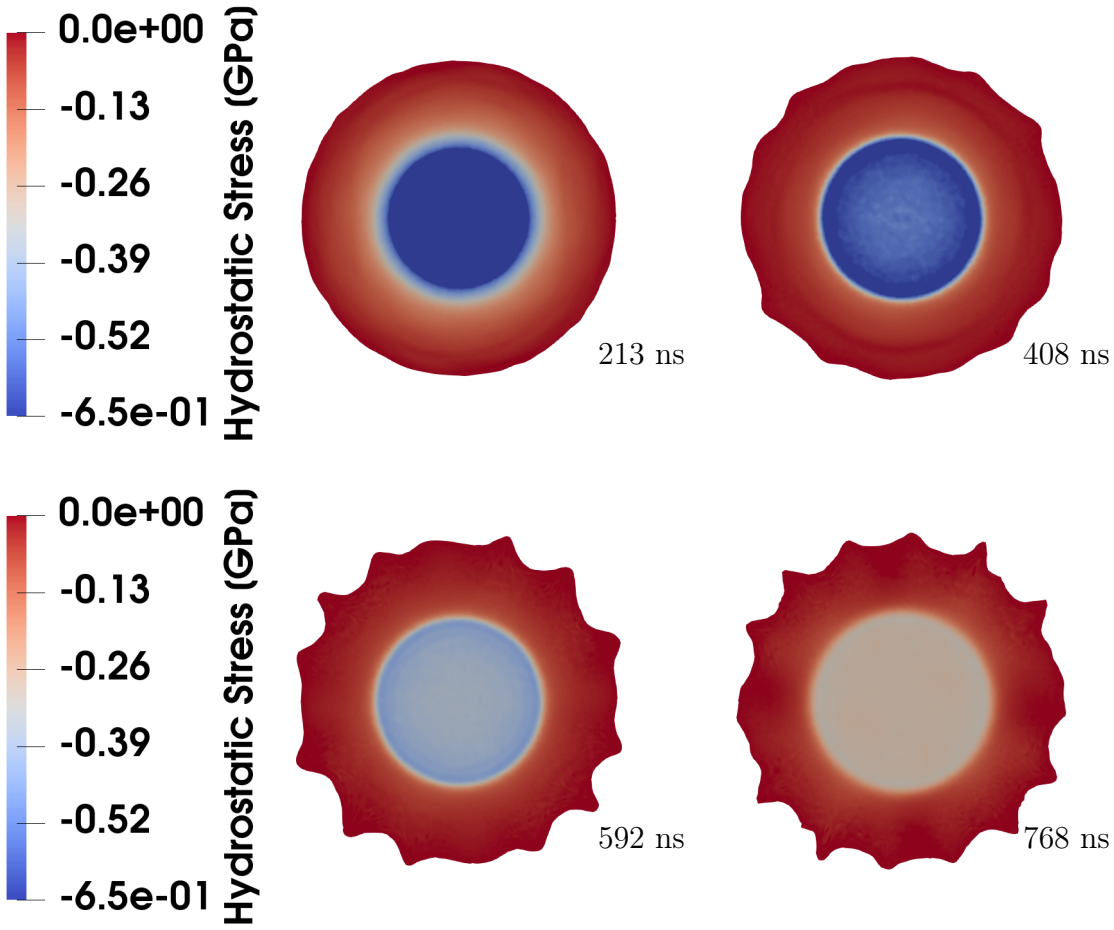

Figure 3-4: Hydrostatic stress contours on a scale from -0.65 to 0 GPa at 213, 408, 592, and 768 ns. A diverging shock is visible in these frames taken 20 ns prior to each of the final four reflections. The simulations capture eruption formation.

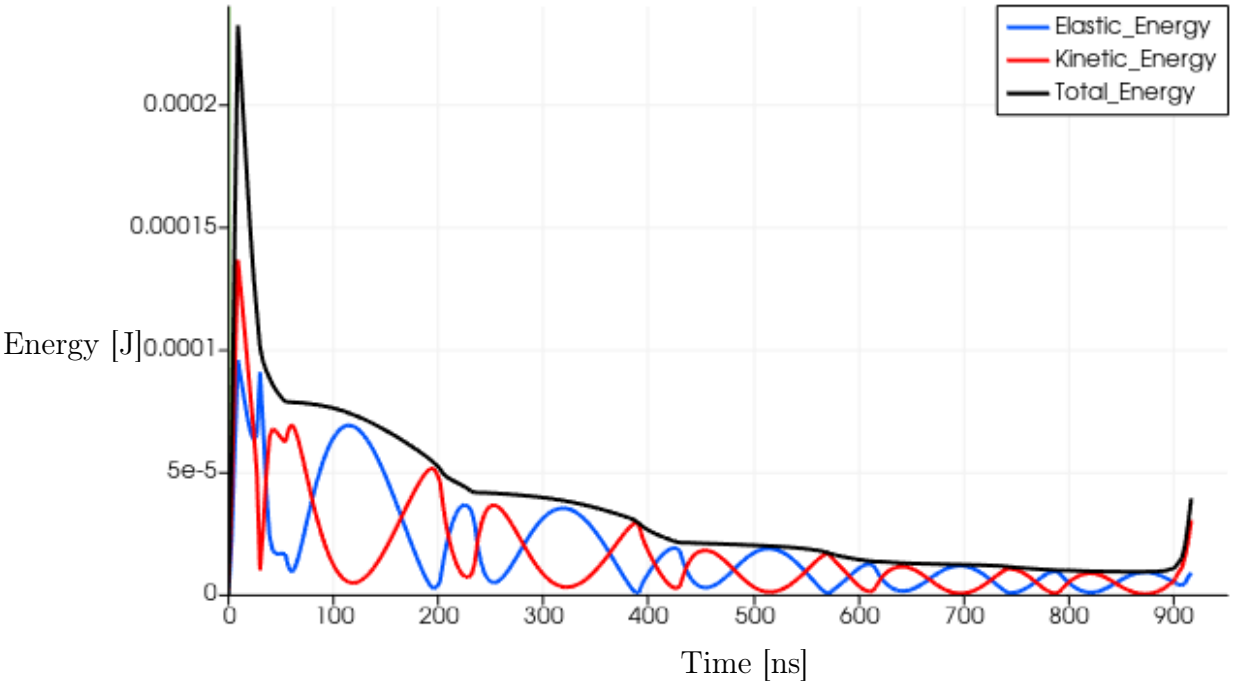

Figure 3-5: The evolution of the energy within the simulation domain. The boundary condition has been tuned to maintain the total energy at similar levels to what occurs in the new experiments.

domain is in compression, which is rapidly unloaded due to high shock speeds, and the elastic energy storage under tension which persists for longer due to softening.

3.3 Mechanistic Interpretation of Simulated Instabilities

An initial analysis of this simulation reveals a number of interesting features in addition to similar boundary undulations to those seen in experiment. To provide insight into the formation of undulations, the evolution of the minimum (blue) and maximum (red) radial displacements on the free surface is monitored in Fig. 3-6. For comparison purposes a scalar metric of instability amplitude $\bar{A} = \frac{max(r(R_0,\theta)) - min(r(R_0,\theta))}{R_0}$ is shown on the right axis. Here $r(R,\theta)$ denotes the radial component of the deformation mapping ϕ and R_0 is the initial radius of 90 μm.

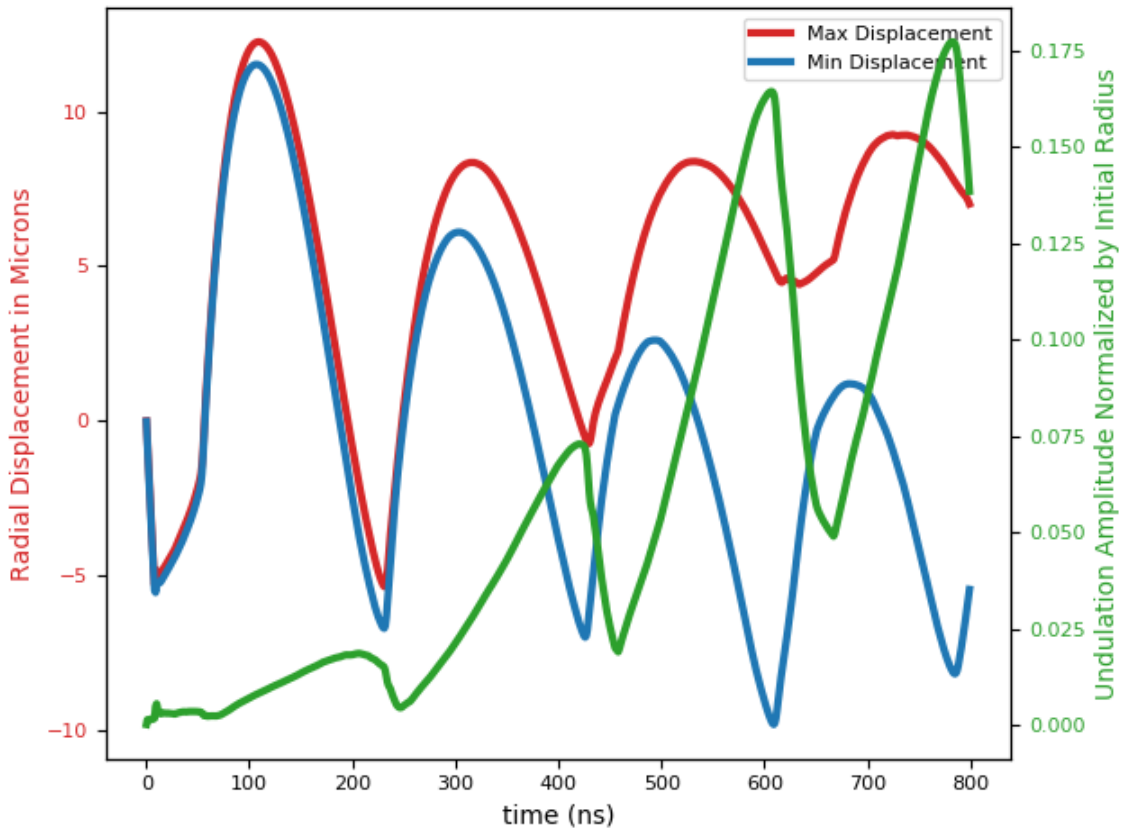

Figure 3-6: Maximum (red) and minimum (blue) radial displacement along the boundary plotted over time. The difference between the two has been normalized by the initial radius of 90 μm and is shown in green.

During the first 55 ns of the simulation, it can be seen that symmetry is almost preserved because the maximal and minimal radial displacements are similar. At this point, the compression wave is steepening into a converging shock front and then diverging towards the boundary. The maximal and minimal radial displacements steadily diverge only after approximately 80 ns as evidenced by the upward sloping green curve from 80 to beyond 200 ns in Fig. 3-6. This figure also shows that during this time interval, both the red and blue radial displacement plots have negative curvature. Undulations develop after the inflection point of the radial displacement curves when the curvature of the displacement as a function of time first becomes negative. The slope of the displacement as a function of time is not important and Fig. 3-6 indicates undulation growth both as the boundary expands and retracts. At 233 ns, the second shock reflection event occurs and imparts a large acceleration on the domain boundary as evidenced by the sharp corner of the red and blue plots around this time. The green curve measuring the maximum nondimensional undulation amplitude $\bar{A}$ decreases rapidly at 233 ns and then begins to rise steadily until after 420 ns. A preliminary decrease in undulation amplitude as the pressure wave meets the boundary is typical of the phase reversal effect common in Richtmyer-Meshkov instabilities of negative Atwood number which was discussed in chapter 1. A detailed illustration of these effects is provided in Fig. 3-7 where the simulated phase reversal that occurs during the third shock reflection is presented. Regularization is due to the focusing effect of the varying curvature of the boundary. The eruptions focus the reflected wave which causes large positive hydrostatic stress (red regions inside the dimples in Fig. 3-7). This tension pulls the eruptions back radially inwards.

The fourth and fifth shock reflections occur at 612, and 788 ns and cause analogous effects to the initial shock reflections in Fig. 3-6 even though the shock energy dissipates with time Fig. 3-5. Each compression wave initially reduces the undulation amplitude and accelerates the boundary outwards. Subsequent growth of instabilities occurs as the radial displacement plots again curve downward. This finding is consistent to first order with Bell's extension of the Rayleigh-Taylor instability to cylindrical domains [46] which has been shown experimentally to cause instability

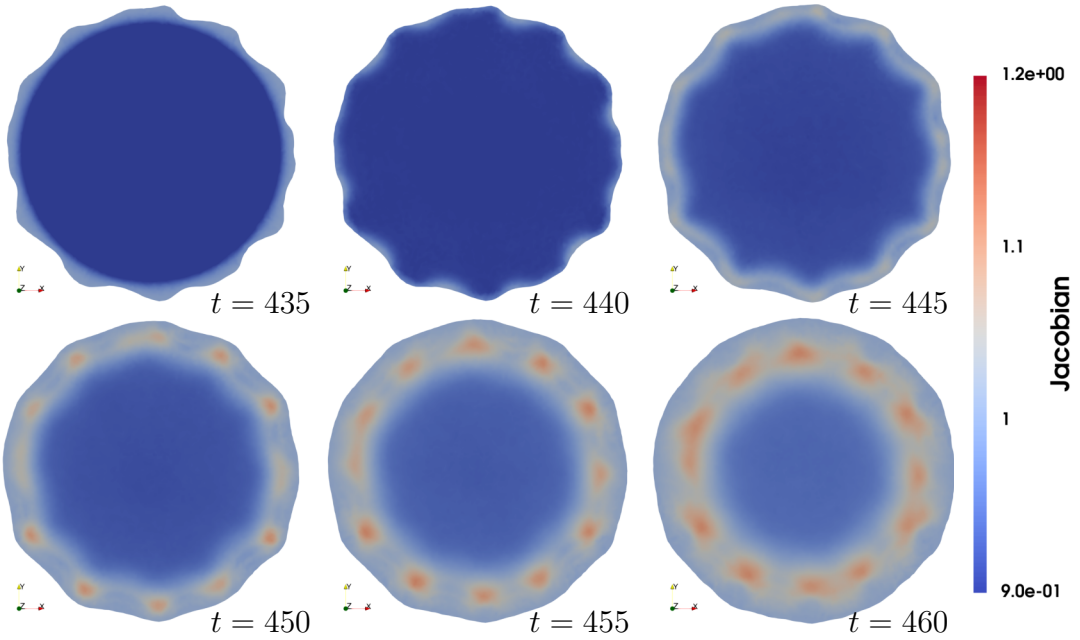

Figure 3-7: Jacobian every 5 ns during the third shock reflection. Observe that the protrusions are regularized. The next sequence of eruptions will form in the regions that were dimples prior to the shock reflection.

growth as curved domains retract [62]. A sine qua non condition for the formation of tension driven Rayleigh-Taylor instabilities is sufficient ultimate tensile strength to sustain the required radial acceleration that generates such instabilities. The low cavitation strength of pure water prohibits instability formation in the new experiments pure water as shown in appendix C. Specifically, the 'tertiary bubble cloud' shown in Fig. 1-13 indicates that upon shock reflection, water cannot sustain the concentrated tensile stress of the reflected wave [82]. The well known dependence of the critical cavitation stress on shear stiffness [127, 128] implies that the deviatoric material response may play a significant role in controlling this unique soft solid instability mechanism.

The undulation amplitude increases linearly as the boundary accelerates inwards, however, the proportional undulation growth shown here is different from that predicted by Richtymer's theory in Eq. 1.3. In Fig. 3-6, it is apparent that the slope of the green curve after the third and fourth shock reflections is approximately the same, even though these shocks meet corrugated boundaries with different initial cor-

rugation amplitudes. The slight viscous dissipation shown in Fig. 3-5 does not fully account for this apparently fixed proportional growth rate.

Instead, a second mechanism contributes to the growth of the surface instability, namely the development of a circumferential compressive stress, which occurs when the boundary is pulled radially inwards, Fig. 3-8. It bears emphasis that the hoop compression of interest here occurs under radial tension and therefore contributes a significant deviatoric component to the state of stress. The lack of deviatoric stiffness of the material model allows the boundary to form undulations in these conditions. The maximum hoop compression that occurs due to radial tension along the boundary is 11 MPa at 180 ns, but megapascal-scale hoop compression is also found in subsequent pressure cycles. Although these hoop stresses are diminutive compared to the GPa-scale pressures arising from shock compression, they are large when compared to the 5 kPa shear modulus of the soft hydrogel. The hoop stress induced eruption growth is a dynamic version of the Biot type wrinkling instability that occurs along the surface of an elastic half-space [30]. This effect requires the model to enter the large deformation regime and necessitates large amplitude shock-induced vibrations. The curved nature of the domain is essential because it is the retracting of the domain boundary under tension which reduces the hoop strain and causes compressive circumferential stress. Similar computations modeling a flat boundary do not produce tangential stresses and consequently fail to induce large scale eruption formation.

Radial tension causes instability growth in two separate ways: first it provides the inwards acceleration which produces the incipient formation of instability growth via an inertial effect similar to cylindrical Rayleigh-Taylor instability and second it decreases the circumferential strain and leads to large compressive stress tangent to the free surface. The first effect is possible along planar interfaces, though it has not been reported in the literature on soft solids under shock loading, and it causes only moderate instability growth. The second effect requires both a curved domain boundary and large amplitude waves, but leads to far larger undulations. To illustrate the combined effects, enlarged snapshots of the radial, hoop and von Mises stress during the third shock reflection when undulations are clearly noticeable are

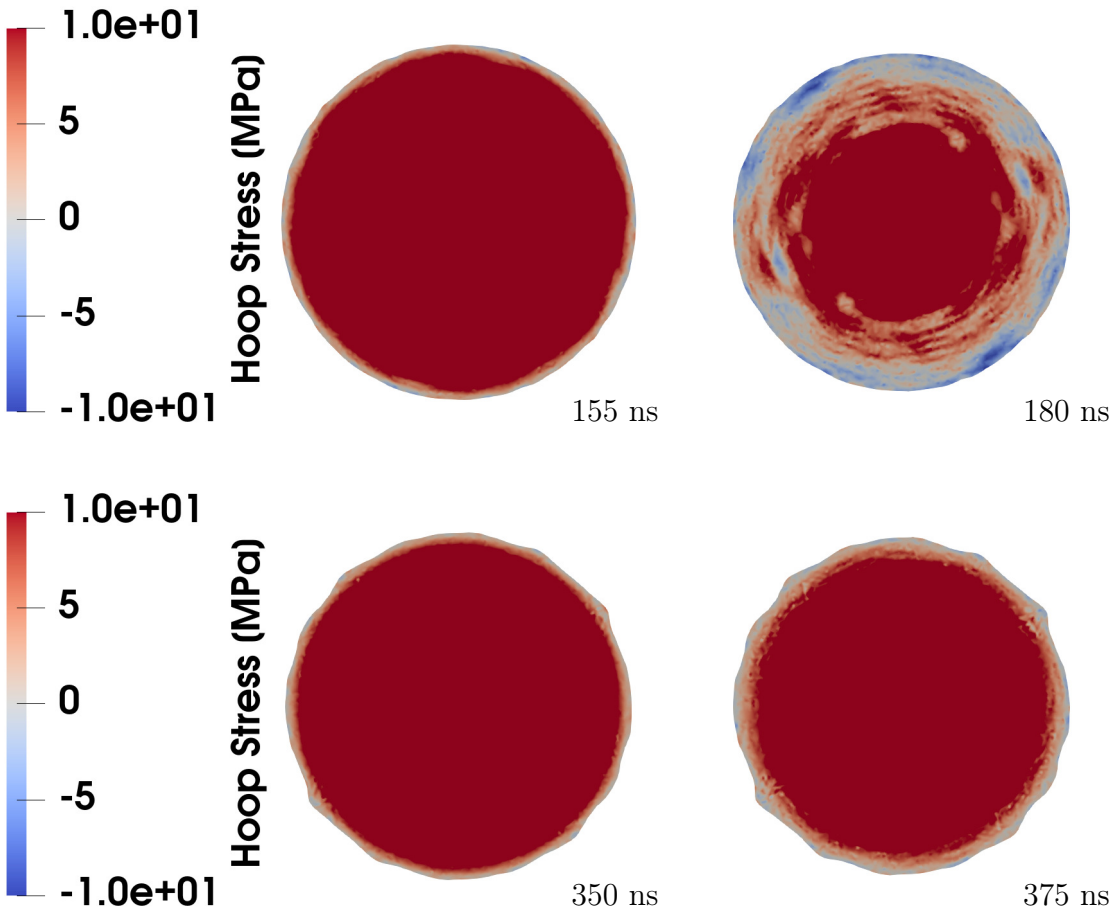

Figure 3-8: Top: Hoop stress on a ±10.0 MPa scale at 155 and 180 ns. Bottom: Hoop stress on a ±10.0 MPa scale at 350 and 375 ns.

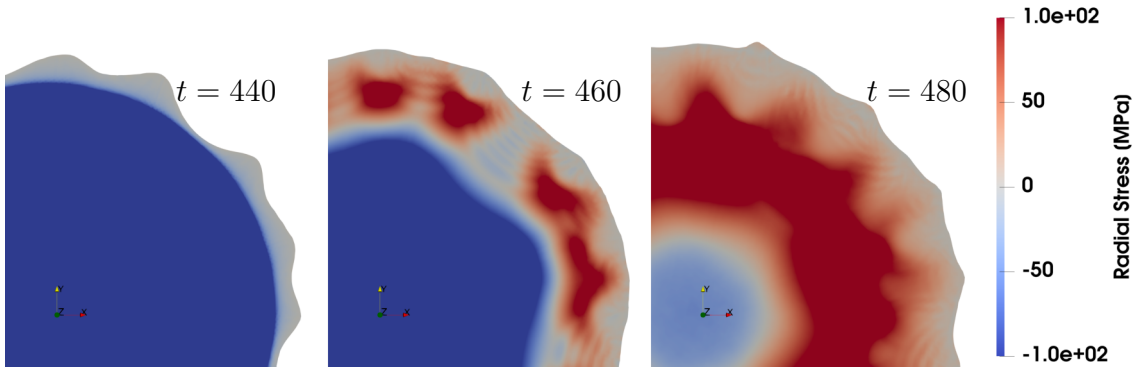

Figure 3-9: Radial stress at 440, 460 and 480 ns. Note that the diverging pressure wave is nearly circular, while the reflected wave shows the complex structure expected from reflections off of curved surfaces.

presented in Figs. 3-9—3-11.

The radial and hoop stress fields appear similar on the scale of 0.1 GPa, but their differences are evident on the scale of 10 MPa as evidenced by distinct regions of inhomogeneous von Mises stress Fig. 3-11. It is found that hoop stress is most negative near protrusions where it enhances undulation growth Fig. 3-10 and that the radial tension is non-uniform as is expected due to the presence of Rayleigh-Taylor type mechanisms of instability. Hydrostatic pressure is greatest near regions of higher surface curvature which motivates the additional studies of domains with non-constant surface curvature presented appendix A. It is evident from the snapshots of the third cycle of wave reflections that the diverging pressure wave is nearly perfectly circular as is typical of diverging shocks [93], but the reflected tensile wave lacks axial symmetry due to corrugations along the free surface.

Due to the softness of the shear response, the von Mises stress indicates significant viscous effects and deformation. Fig. 3-11 clearly shows that the breakdown of symmetry is not restricted to the surface of the computational domain because the von Mises stress is asymmetric even in the interior of the disk. The reflected waves display complex spatial and temporal inhomogeneity which induces oscillatory stress on the free surface and causes minute oscillations in the undulation growth rate.

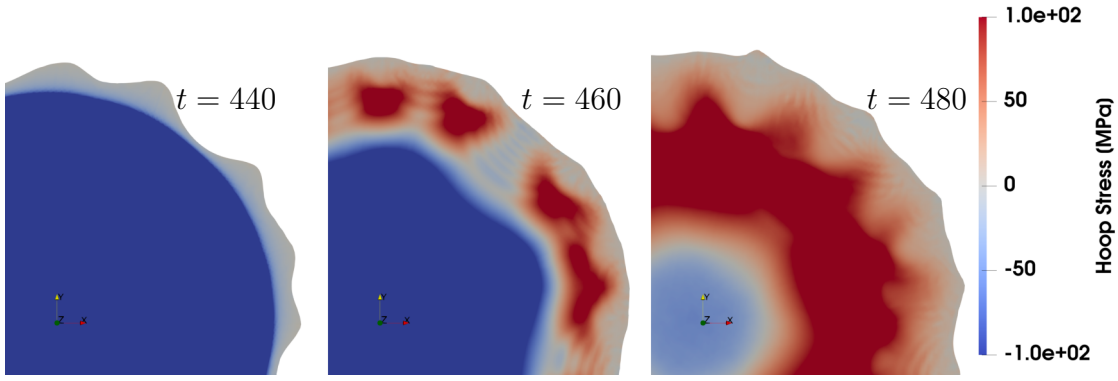

Figure 3-10: Hoop stress at 440, 460 and 480 ns.

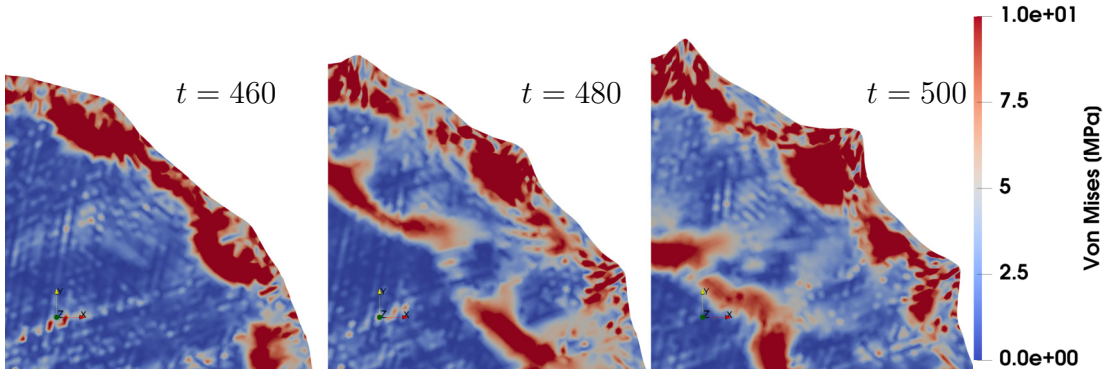

Figure 3-11: Von Mises stress at 460, 480 and 500 ns.

3.4 Modal Analysis of Undulation Formation

A striking feature of the computational results shown in Fig. 3-4 is the similarity between the computed and experimentally observed instability wave-numbers. In contrast to many works, which seed an initial instability mode of interest by studying a pre-corrugated interface's response to shock transmission [48–50], here a circular domain with no predetermined instability mode is utilized, and it is found that multiple Fourier modes are excited by the mechanisms described in section 3.3. In Fig. 3-12, the evolution of ten Fourier modes of the radial displacement profile along the boundary are plotted as a function of time. Analysis of the initial stages of instability growth just after the first inflection point of the radial displacement as a function of time at approximately 80 ns indicates that multiple modes are active and growing steadily at rates on the order of 10 m/s. The growth rates of the various modes are not constant due to the spatial and temporal oscillations in the reflected tensile wave which drives continued growth Figs. 3-9—3-11. The computed oscillations in the modal growth rate are analogous to oscillations reported by Richtmyer [47] in his numerical study of shocked gas interfaces. Richtmyer attributed his numerical oscillations to corrugations in the reflected and transmitted shocks that oscillate temporally long after the initial shock-interface interaction. In the simulations considered here there is no shock transmission across the interface, but corrugations in the tensile reflected wave are observed which induce comparable oscillations around the asymptotic modal growth rates.

As instabilities develop further, large wavelengths are preferentially amplified, but the largest wavelength undulations do not occur. In Fig. 3-13, two-dimensional colored plots are displayed which represent the amplitude of various Fourier components of the boundary radial displacement as a function of nondimensional time $\bar{t} = \frac{t}{R_0}\sqrt{\frac{\kappa}{\rho}}$. The simulation captures the growth of many wave-numbers during the initial phase when inertial instabilities arising from the radially inwards acceleration are dominant. The large scale undulations of interest are of a moderate wave-number on the order of 20, however, and they are preferentially amplified in later cycles when inertial ef-

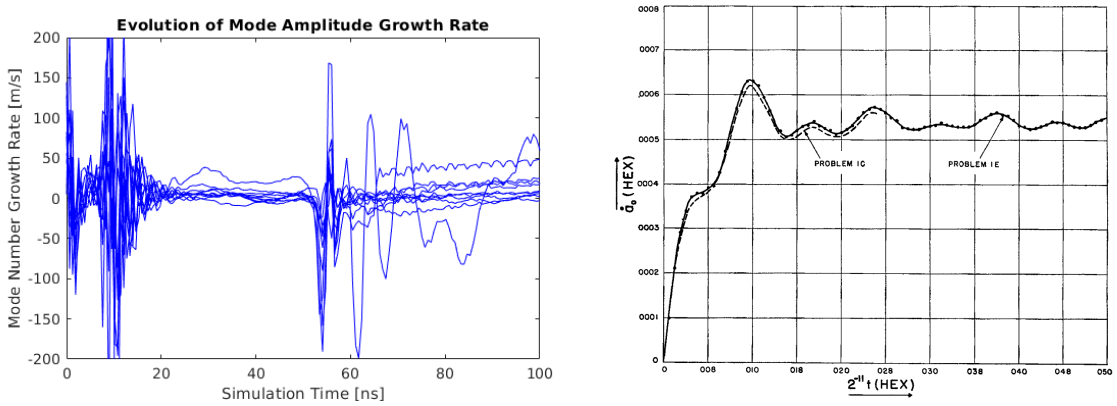

Figure 3-12: Left: The growth rates of Fourier modes 7-17 of the radial displacement field along the boundary. Rates are computed using finite difference estimates at 200 time steps. Right: For comparison the plot from Richtmyer's original paper is included which shows the growth rate of a particular mode that is present prior to instability [47]. Unlike in Richtmyer's study, the simulations presented in section 3.2 do not begin with any intentional asymmetry and a particular mode of interest cannot be isolated.

fects are less dominant, but the hoop compression effect is still significant Fig. 3-13. Consistent with the work of Biot [30], the radius of curvature of the domain imposes a characteristic length which restricts the formation of the largest wavelength undulations.

Though negative radial acceleration plays a key role in this and George Bell's cylindrical instability mechanism [46], the simulated instability modal evolution does not match closely with Bell's theoretical modal evolution equations due to the compressible nature of the simulations and the existence of strong shocks and nonlinear pressure waves. In Fig. 3-14, a direct comparison of the simulated rate of change of modal growth rates (computed with a second order finite difference scheme) with George Bell's incompressible theory is presented. Bell theorized that the rate of change of a growth rate should be proportional to the mode number, mode amplitude and the nondimensional surface acceleration given by the average value of $\frac{\ddot{r}(R_0,\theta)}{r(R_0,\theta)}$. His incompressible theory drastically overestimates the rate of change of the instability growth rate and fails to capture the preference for undulations of a particular wavelength. The rates of change of the growth rates are also found to oscillate considerably

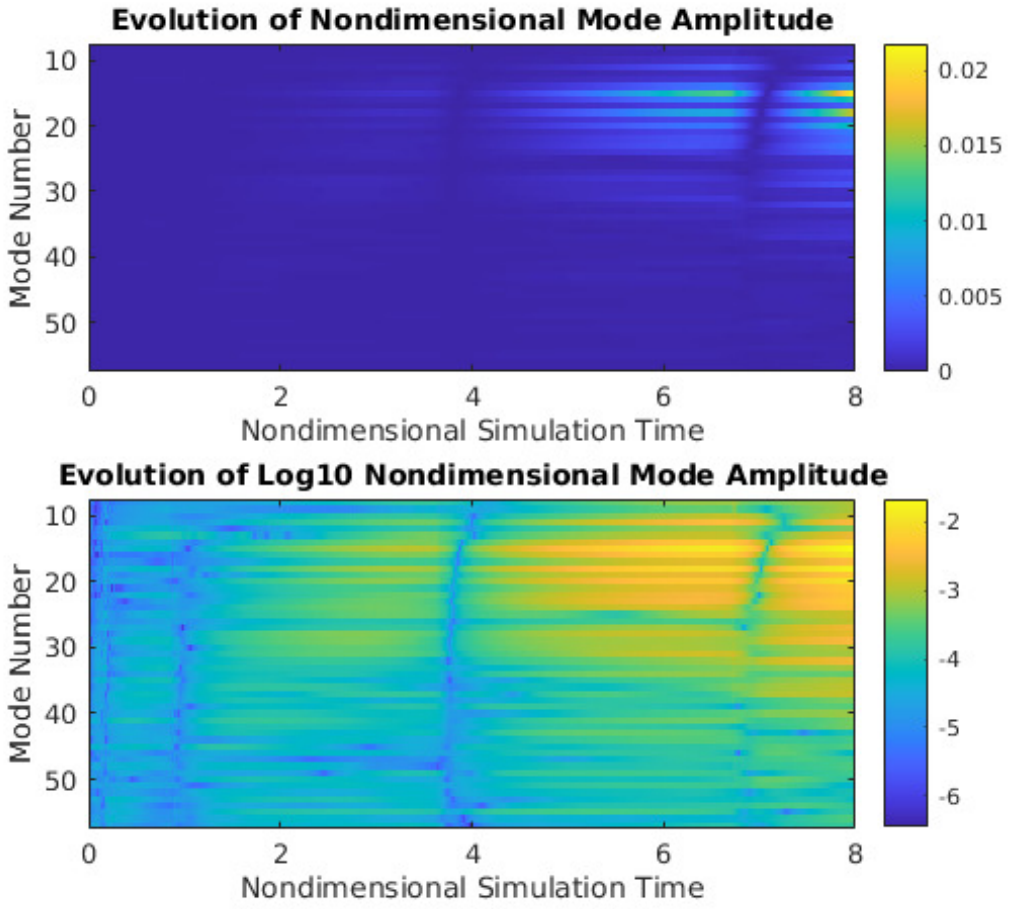

Figure 3-13: Evolution of the Fourier modes of surface undulation in our calculations (normalized by the domain radius $R_0 = 90$ μm) plotted against nondimensional time $\bar{t} = \frac{t}{R_0}\sqrt{\frac{\kappa}{\rho}} = 63$ ns. Observe that large scale hoop-compression driven instability produces undulations of wave-number on the order of 20.

due to the effects shown in Fig. 3-12. These oscillations are slightly out of phase which gives the appearance of curved diagonal streaks at a nondimensional simulation time of ≈ 7.5 and fainter streaks at a nondimensional simulation time of ≈ 4.1. Bell's theory does not account for such oscillations. The figure shows an additional similarity with Richtmyer's work; the shock compresses the interface and decreases the Fourier modes of the undulation amplitude [47]. This effect is most pronounced with regard to the most active mode numbers and is apparent during the second shock reflection at a nondimensional simulation time of ≈ 3.6. During the third reflection event at a nondimensional simulation time of ≈ 6 decreasing modal growth rates are observed for the lower wave-numbers before the higher wave-numbers because the domain boundary is no longer approximately circular. Large troughs around the boundary are met by the shock earlier which decreases the low wave-number modes associated to the large troughs before the higher modes.

Besides the discordant comparison with Bell's evolution equations, it is clear that additional mechanisms beyond the Rayleigh-Taylor instability are at play because no undulations are observed around the external ablation zone surface in the new experiments. According to Bell's theory, the external ablation zone should lose stability as it accelerates radially outward (as opposed to the negative acceleration driving undulation growth on the interior surface). The external ablation zone surface does accelerate radially outward, but shows no loss of symmetry because this is not the dominant mechanism for undulation formation. Hoop compression does not form along the external surface as the laser ablated material pushes radially outward which prohibits the new mechanism considered here from forming.

3.5 Nondimensional Analysis

The factors influencing instability formation have been described qualitatively and shown to be the radial acceleration and hoop compression which both result from hydrostatic tension inside the domain. In turn, prolonged hydrostatic tension is possible due to extensive softening of the equation of state under large dilatation. These

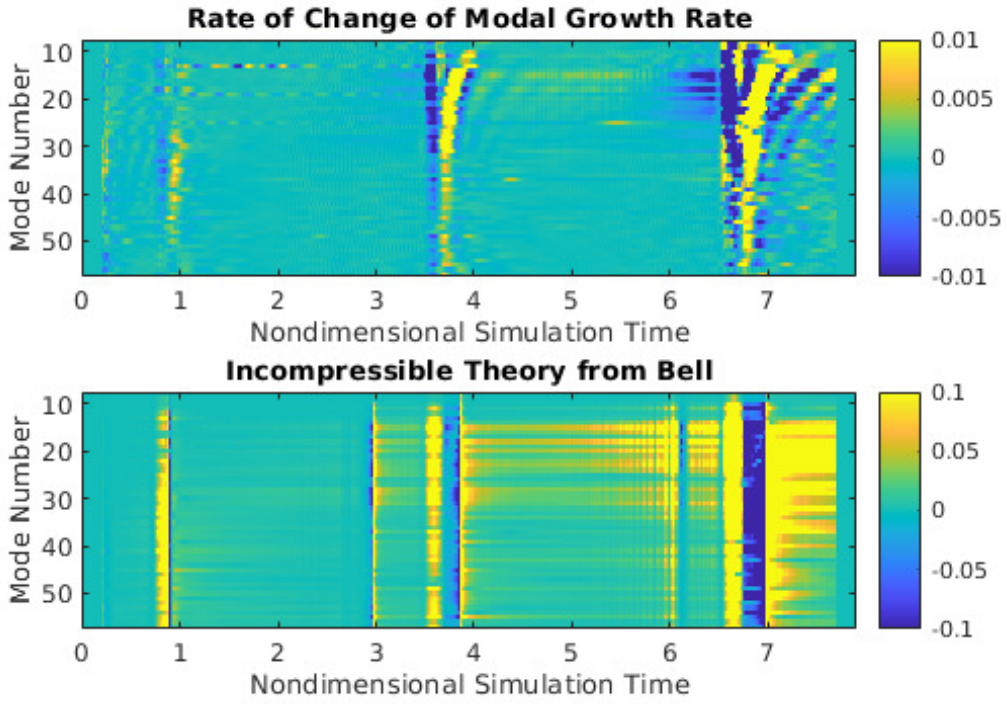

Figure 3-14: Comparison between the rates of change of the modal growth rates in our simulation and assuming the incompressible Rayleigh-Taylor theory from George Bell [46]. Finite difference estimates were used to compute time derivatives

findings are in contrast to typical large amplitude shock instabilities where the overall response depends on the post-shock stiffening of material properties [47]. To highlight this distinction and demonstrate the role of the two fundamental destabilizing effects, a nondimensional study of the relevant physical parameters is presented in this section. The following nondimensional groups span the space of parameters considered in the initial simulations. In addition to the stiffening parameter - $\bar{\gamma}$, and the two viscosity parameters $\bar{c}_1$ and $\bar{c}_2$, which are already nondimensional, a nondimensional wave amplitude - $\bar{P}$, nondimensional pulse duration - $\bar{t}_{pulse}$, and a compressibility factor - $\bar{\mu}$ are defined as follows:

$$\bar{P} = \frac{P_{pulse}}{\kappa}, \qquad \bar{t}_{pulse} = \frac{t_{pulse}}{R_0}\sqrt{\frac{\kappa}{\rho}}, \qquad \bar{\mu} = \frac{\mu}{\kappa} \tag{3.1}$$

Here κ is the bulk modulus, μ is the shear modulus, ρ is the density, R_0 is the radius of curvature, t_{pulse} is the duration of applied loading, and P_{pulse} is the amplitude of the applied loading. The simulation time is normalized by the same timescale as the nondimensional pulse duration. The nondimensional parameters took on the values $\bar{\gamma} = 6.15$, $\bar{P} = 1.0$, $\bar{t} = 0.1257$, $\bar{\mu} = 2.5 \times 10^{-6}$ in the initial calculations. Starting from these initial values, each parameter is explored in turn by varying them one at a time from 50 % to 150 % of their initial values.

3.5.1 Analysis of the Undulation Amplitude

Increasing $\bar{P}$ is the easiest parameter to control in the experiment and directly corresponds to depositing additional energy in the simulation. Fig. 3-15 shows the results of a parametric study performed using 61 simulations of the first cycle of the pressure wave. The color in the two-dimensional plot indicates the nondimensional undulation amplitude $\bar{A}$ as a function of time along the horizontal axis for a variety of nondimensional pulse amplitudes varied along the vertical axis. The 61 simulations are integrated in time until $\bar{t} = 4$, which corresponds to the time required for acoustic waves to cross the computational domain once, reflect, and return to their starting position. The nonlinear waves captured by these simulations can traverse this same

domain faster or slower depending on the value of $\bar{P}$.

It was found that raising $\bar{P}$, ceteris paribus, increases instability growth by prolonging the tensile phase of the oscillation cycle which drives instability growth. Notably, the stronger shocks produced with larger $\bar{P}$ are found to propagate faster, but also lead to such prolonged tensile phases of vibration that the overall oscillation frequency decreases Fig. 3-15. The increase in shock speed is indicated in the figure by a faint, darker streak starting at $\bar{t} \approx 0,75$ on the bottom of the chart, which slopes upwards towards $\bar{t} = 1$ at the top of the chart. This dark region marks the time when the first shock reflects and leads to the first decrease in undulation amplitude. In the baseline simulation this occurs at 55 ns, which is $\bar{t} \approx 0.87$. Larger amplitude waves traverse the domain in less time, while acoustic waves require more than 126 ns or $\bar{t} = 2$ to traverse this distance. The overall decrease in the oscillation frequency with $\bar{P}$ is indicated by the dark blue in the upper right of Fig. 3-15. This more noticeable region of the chart indicates the time when the second shock meets the boundary and decreases the undulation amplitude a second time. In the baseline simulation this second shock reflection occurs at 233 ns, which is when $\bar{t} = 3.66$. Notice that for larger values of $\bar{P}$ the second reflection occurs later in time while for smaller values the reflection occurs earlier. Bearing in mind that acoustic waves would reflect exactly when $\bar{t} = 4$, one finds that small amplitude nonlinear waves shown at the top of the chart actually have smaller oscillation periods than linear vibrations and hence have a higher oscillation frequency. In contrast, large amplitude waves shown at the bottom of the chart do not meet the boundary a second time prior to the end of these simulations at $\bar{t} = 4$. These stronger waves produce larger oscillation periods, even though large amplitude shocks travel faster because the tensile phase of vibrations is slowed significantly in this regime of the parameter space. The tensile phase of vibrations is what initiates instability growth, so the larger $\bar{P}$ produces larger undulation amplitude $\bar{A}$ as indicated by the brighter colors in the bottom of the plot.

Moreover, increasing $\bar{t}_{pulse}$ also correlates directly with the energy injected into the computational domain and enhances instability growth by prolonging the tensile phase of the oscillation cycle in the same manner as raising $\bar{P}$. A larger duration of

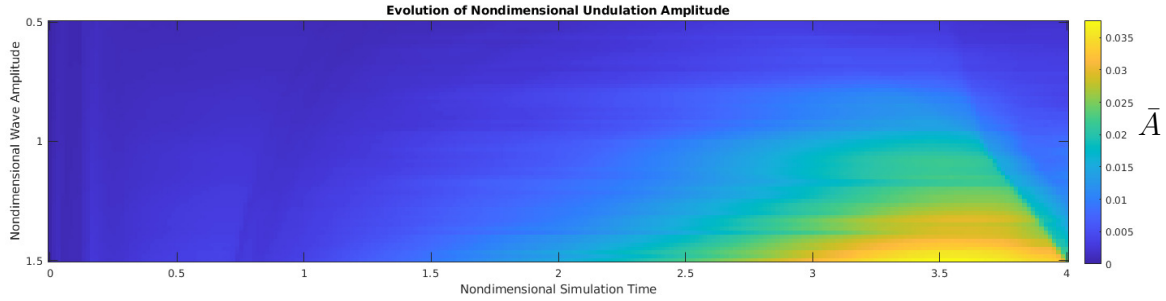

Figure 3-15: Undulation amplitude $\bar{A}$ plotted as a function of time $\bar{t}$ (horizontal axis) and nondimensional wave amplitude $\bar{P}$ (vertical axis). Increasing $\bar{P}$ increases the nondimensional undulation amplitude $\bar{A}$.

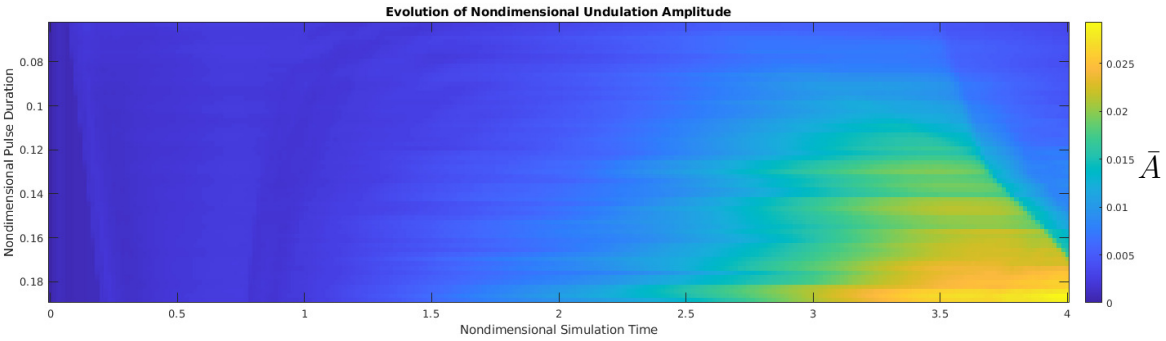

Figure 3-16: Undulation amplitude $\bar{A}$ plotted as a function of time $\bar{t}$ (horizontal axis) and nondimensional pulse duration $\bar{t}_{pulse}$ (vertical axis). Increasing $\bar{t}_{pulse}$ increases nondimensional undulation amplitude $\bar{A}$.

applied pressure produces stronger shocks and similar effects to directly increasing $\bar{P}$. Fig. 3-16. It is worth noting that the impact on the oscillation cycle period and frequency of $\bar{t}_{pulse}$ is qualitatively similar to $\bar{P}$, and if anything more dramatic. The dark blue region on the upper right has more gradually sloped boundaries in Fig. 3-16 than in Fig. 3-15 which indicates a stronger sensitivity of the cycle period to the pulse duration than the pulse amplitude. On the other hand, the maximal undulation amplitude excited in the latter chart is larger than in the former. A minor difference between Fig. 3-15 and Fig. 3-16 is the shape of the blue region on the left side of these figures. $\bar{t}_{pulse}$ increases linearly down the vertical axis in the second chart, leading to the triangular blue region, but is held fixed in the first study which has a rectangular dark blue region on the left side.

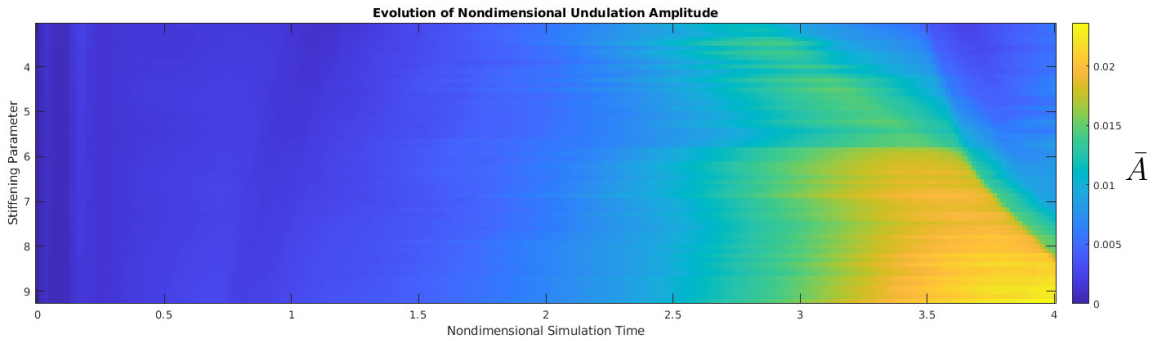

Figure 3-17: Undulation amplitude $\bar{A}$ plotted as a function of time $\bar{t}$ (horizontal axis) and stiffening parameter $\bar{\gamma}$ (vertical axis). Increasing $\bar{\gamma}$ increases nondimensional undulation amplitude $\bar{A}$.

Increasing the nondimensional stiffening parameter $\bar{\gamma}$ does not correspond directly to varying the loading conditions and is more challenging to study in an experimental setting because it requires modifying material properties. Nevertheless, the computational framework employed here easily allows for the study of this parameter which is found to play an important role in the ensuing dynamics. Similar to $\bar{P}$ and $\bar{t}_{pulse}$, enhanced stiffening produces shocks that propagate faster but also slows the tensile phase which leads to slower vibrations and more instability growth as shown in Fig. 3-17. Raising $\bar{\gamma}$ decreases the maximum hydrostatic stress that the material model can sustain $P_{max} = \frac{\kappa}{\bar{\gamma}+1}$ which counterintuitively enhances all the effects arising from hydrostatic tension. When large amplitude shocks reflect off the boundary, their reflected waves have to disperse or spread out because the constitutive law does not allow any elastic hydrostatic stresses larger than P_{max}. By decreasing P_{max}, dispersion and softening is enhanced while the maximal tensile stress in the simulation is reduced. Conversely, adding more energy increases the ratio of shock amplitude to P_{max} which also causes more dispersion and softening. The magnitude of the radial tension is ultimately of lesser significance, and it is the dispersive nature of the stress release waves converging after the shock reflections which induces the hoop stress that drives large scale eruption formation.

A number of features are apparent in Figs. 3-15—3-17 which merit further discussion. The time of the second shock reflection, as indicated by the appearance of

the blue regions in the upper right of the plots, seems to increase linearly with $\bar{\gamma}$, $\bar{P}$ and $\bar{t}_{pulse}$, however, in Fig. 3-17 for instance the impact of variations in $\bar{\gamma}$ changes noticeably after $\bar{\gamma} = \bar{\gamma}^* \approx 5.75$. This is indicated by a clear change in the slope of the division between the bright and blue region at the upper left of the plot. Similar behavior occurs in Fig. 3-15 and Fig. 3-16 when the pulse amplitude is greater than $\bar{P} = \bar{P}^* \approx 0.95$ or the pulse duration is greater than $\bar{t}_{pulse} = \bar{t}^*_{pulse} \approx 0.12$, all else being equal. For large nondimensional groups, the undulations appear to grow monotonically until the shock meets the domain boundary while for smaller values of the parameters, the undulations decrease in amplitude prior to the shock arrival. This trend is most clearly visualized in Fig. 3-17 where a green streak from the top of the chart at $\bar{t} \approx 2.8$ runs diagonally downwards and indicates the peak undulation amplitude. This peak occurs well before the arrival of the second shock which indicates undulation amplitude decrease prior to the shock arrival. If $\bar{\gamma} = 4$ for instance, $\bar{A}$ begins to decrease at $\bar{t} = 3.2$, but the second shock does not arrive until $\bar{t} = 3.5$. In contradistinction, toward the bottom of Figs. 3-15—3-17 instabilities grow in a periodic sawtooth manner which is exemplified explicitly by the green curve in Fig. 3-6.

Small values of these three nondimensional groups $\bar{\gamma}$, $\bar{P}$ and $\bar{t}_{pulse}$ produce weakly nonlinear waves which are weak in the sense that the celerity jump across the wave front is small. Due to the smaller celerity jump in the weakly nonlinear calculations, the boundary radial tension is relaxed prior to the arrival of the compression wave because the wave speed under tension is large enough to propagate stress release waves to the boundary prior to the next reflection. Relaxing the boundary radial tension before the diverging pressure pulse pushes the boundary outwards again slows the formation of undulations and allows instabilities to decrease prior to the shock arrival. By contrast to the blue and red curves in Fig. 3-6, the radial displacement varies nearly sinusoidally in such weakly nonlinear simulations. In the case of strong shocks when the parameters $\bar{\gamma}$, $\bar{P}$ and $\bar{t}_{pulse}$ are large, the celerity jump across the wave front is significant and waves cannot propagate to the boundary under tension due to the extreme softening of the equation of state. The compression wave front appears to

reach the boundary before radial tension has relaxed which is why undulation growth continues up until the shock arrives in these calculations.

Additionally, in the case of strongly nonlinear waves the boundary is typically displaced inwards while still under radial tension prior to the shock reflection. This situation corresponds to compressive hoop strain (and stress) while under radial tension, and it is this state of stress that leads to large scale undulation growth because it has a significant deviatoric component. Note that in Fig. 3-17 in particular, the strongly and weakly nonlinear wave simulations indicate comparable rates of undulation growth until $\bar{t} \approx 3.0$. At this point in time, the strongly nonlinear simulations begin to develop large deviatoric stress due to hoop compression which increases $\bar{A}$. In contrast, the weakly nonlinear simulations start to decrease their undulation amplitude since the model does not soften under tension sufficiently to maintain both radial tension and negative radial displacements. The loading parameters $\bar{P}$ and $\bar{t}_{pulse}$ exhibit similar effects on the model which are evident in Figs. 3-15—3-16, but increasing these parameters also increases the inertial mechanisms of instability as well by directly increasing the energy in the model.

In summary, increasing the first three parameters $\bar{P}$, $\bar{t}_{pulse}$ and $\bar{\gamma}$ pushes the equation of state farther into the nonlinear regime. All three parameters govern the softening material response under tension and determine whether the model exhibits strongly nonlinear dynamics that lead to the development of deviatoric stress which is manifest as hoop compression and simultaneous radial tension. For moderately nonlinear simulations the increased shock speed is the primary nonlinear effect, while for strongly nonlinear simulations softening under tension plays a dominant role. Nonlinear effects are necessary to excite these instabilities, and in contrast to the Richtmyer-Meshkov instability undulation growth is controlled primarily by the dispersion, or a lack thereof, in the tensile phase of the pressure cycle. As discussed in chapter 1, incompressible, acoustic and shock loaded surface instabilities have all been studied previously, but here we present a unique strongly nonlinear instability that relies on shock reflection induced dispersion.

A final observation from the consideration of these first three nondimensional

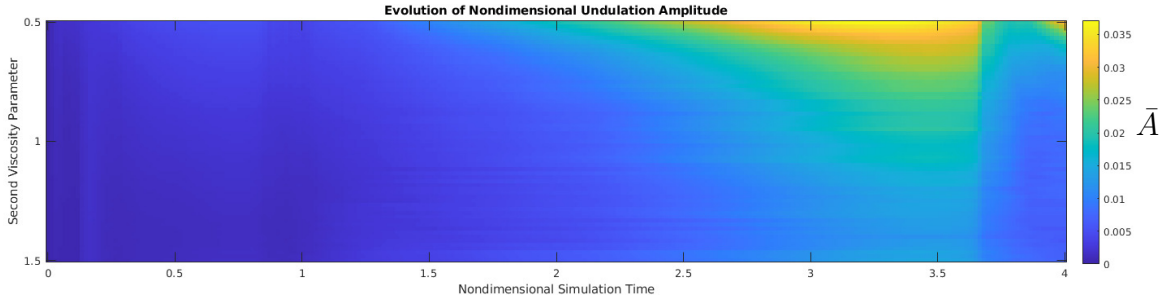

Figure 3-18: Undulation amplitude $\bar{A}$ plotted as a function of time $\bar{t}$ (horizontal axis) and second viscosity coefficient $\bar{c}_2$ (vertical axis). Increasing $\bar{c}_2$ decreases and slows instability growth.

groups is the general finding that increasing these groups increases undulation growth is not strictly true, but is generally the case. Considering Figs. 3-15—3-17 during the phase of undulation growth, it is not the case that these plots become strictly lighter as one moves toward the bottom of these figures. In particular, some light streaks in Fig. 3-16 indicate that in rare instances slight increases to the applied pulse duration may decrease the undulation amplitude at particular nondimensional times in the simulation. Similar effects are noticeable in Fig. 3-15.

One final parameter which plays a key role in regulating instability growth is the second viscosity parameter $\bar{c}_2$. Decreasing this parameter leads to enhanced instability growth because the artificial viscosity model is necessary to stabilize numerical oscillations due to the shock front Fig. 3-19. This parameter will not be considered further since it is a numerical modeling parameter and does not represent any physical effects.

Aside from the parameters which actively regulate physical and numerical mechanisms of instability growth ($\bar{P}$, $\bar{t}_{pulse}$, $\bar{\gamma}$ and $\bar{c}_2$), variations in $\bar{\mu}$ and $\bar{c}_1$ are also studied. These parameters are not found to play a role in controlling instability formation and varying them by $\pm 50\%$ has little impact on the simulations Figs. 3-19—3-20.

Fig. 3-20 indicates that for the small values of $\bar{\mu}$ considered here, shear stiffness does not actively control instability growth. This is a significant distinction from the finding in [59], that elastic Richtmyer-Meshkov instabilities oscillate periodically at frequencies that are proportional to the mode number divided by the shear wave

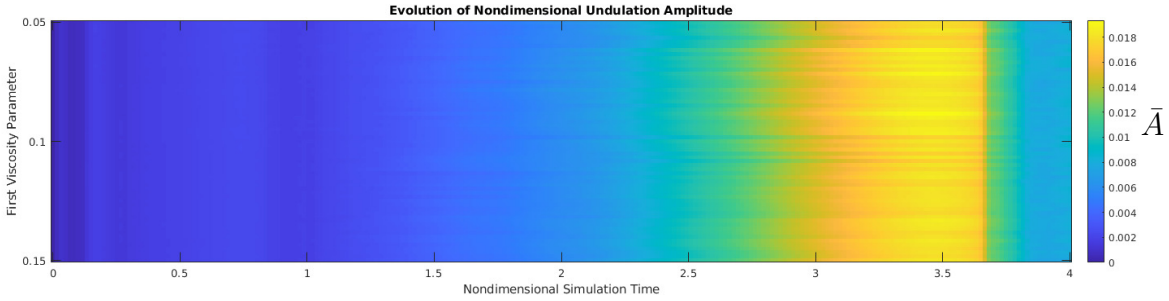

Figure 3-19: Undulation amplitude $\bar{A}$ plotted as a function of time $\bar{t}$ (horizontal axis) and first viscosity coefficient $\bar{c}_1$ (vertical axis). Increasing $\bar{c}_1$ has little effect on the simulation results.

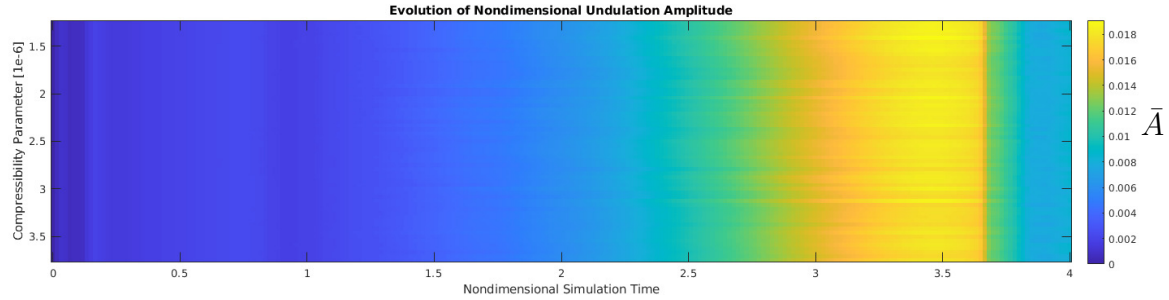

Figure 3-20: Undulation amplitude $\bar{A}$ plotted as a function of time $\bar{t}$ (horizontal axis) and compressibility ratio $\bar{\mu}$ (vertical axis). The vertical scale has been scaled by a million. Increasing $\bar{\mu}$ has little effect on the simulation results.

speed. In both these simulations and the new experiments, the pressure cycles far faster than this frequency expected from classic elastic Richtmyer-Meshkov instability because the domain curvature is large and the shear stiffness is small. In an elastic Richtmyer-Meshkov instability deviatoric elastic energy provides a restoring force to the boundary, but here the shock itself restores the boundary and hence the shear stiffness is not a controlling effect.

The finding that linear viscosity and shear stiffness do not actively regulate instability growth is consistent with prior studies of both dynamic droplet jet formation [62] and quasistatic elastic fingering [2]. These parameters are similarity parameters of the first kind and may be neglected if sufficiently small, but the importance of both the extremely soft elastic response and the significance of hoop compression found in our simulations is underscored by the finding that when the shear modulus exceeds

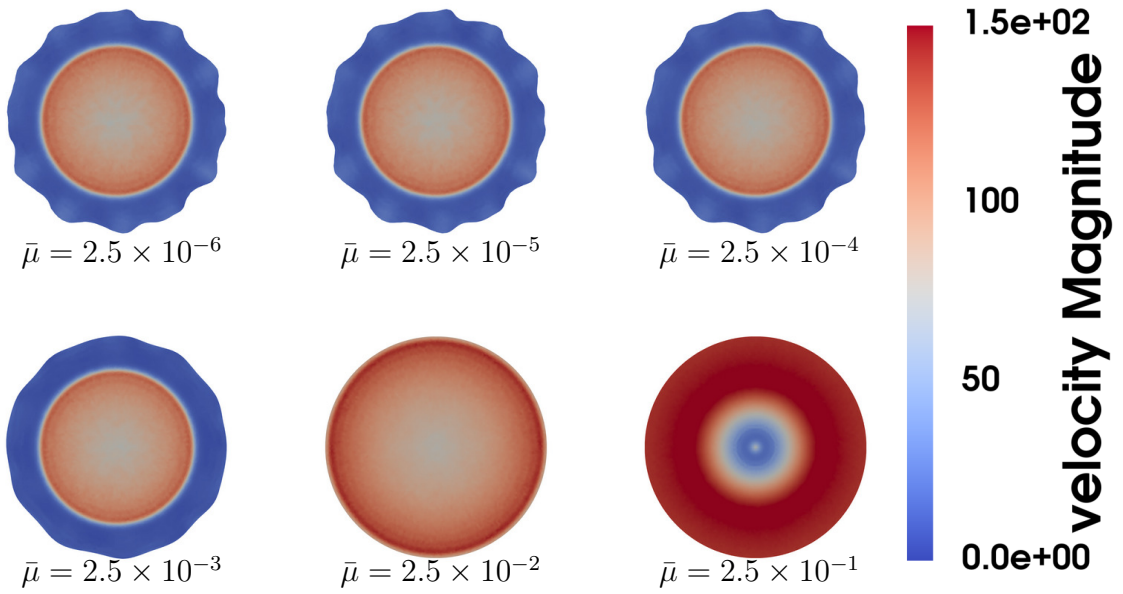

Figure 3-21: Velocity magnitudes taken from six different simulations at $t = 425$ns ($\bar{t} = 6.74$). $\bar{\mu}$ is successively increased by a factor of 10 at a time beginning from 2.5×10^{-6}.

approximately 5 MPa, instability growth is regularized Fig. 3-21. In other words, altering the shear modulus has no impact on the calculations until $\bar{\mu}$ is increased over a hundred-fold. Additionally, it is found that shear stiffness regularizes high wavenumber instabilities first. A similar regularization is obtained by increasing the linear viscosity parameter.

By raising the compressibility parameter by up to four orders of magnitude the importance of the role of hoop compression is clearly visible Fig. 3-22. When the hoop stress is of the same order of magnitude or larger than the shear modulus, undulations grow rapidly. In contrast, when the shear modulus exceeds the hoop compression, instabilities are regularized. Biot instability develops at a critical strain for all neo-Hookean materials and the critical stress is related to the strain by the shear modulus, but in the models shown here the value of the hoop stress is controlled by the parameters regulating the shock dynamics and the value of the shear modulus must be larger to regularize undulation growth.

The dynamics described in this thesis are similar to the two-step mechanism described in the recent work of Ohl et al. [62]. In this paper the authors describe droplet

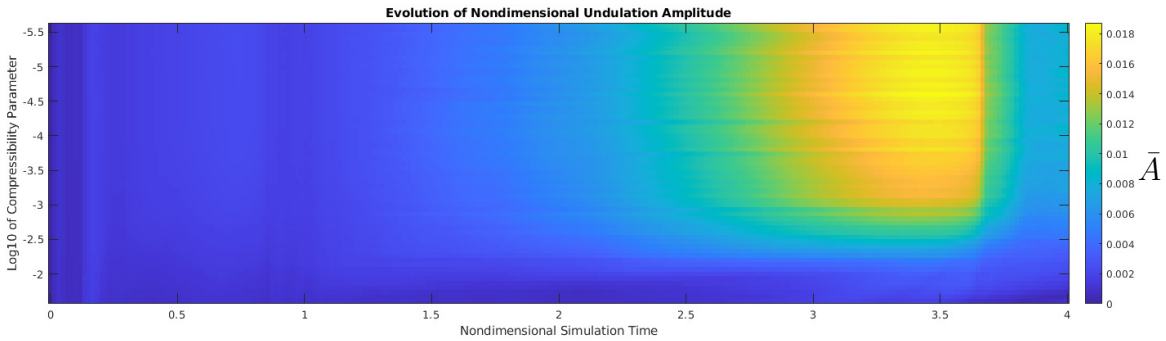

Figure 3-22: Increasing $\bar{\mu}$ has a significant regularizing effect on the simulations if $\bar{\mu}$ exceeds the nondimensional value of the hoop stress during the tensile phase of the vibrations.

jetting via a spherical Rayleigh-Taylor type mechanism that corresponds to the tension driven radial acceleration which initiates instability in our calculations. These authors also discuss the phase reversal along the boundary due to pressure wave reflections. Their findings are consistent with the present calculations and in particular their models of three-dimensional high Reynolds number, low Weber number droplets also produce instability wave-numbers of ≈ 20 Fig. 1-9. They model the cavitation zone in the center of the droplet explicitly, and select a low Weber number which corresponds to a large surface tension along the interior cavity of a small droplet. These effects combine to exert significant radial tension on the external boundary of the droplet which may lead to jet formation very similar to the findings of this thesis. Their mechanistic interpretation, however, focuses solely on the discussion of baroclinic instabilities which are common in the fluid mechanics literature. In this thesis, the importance of hoop compression is emphasized instead because it underscores the importance of the small radius of curvature and marks the critical value of the shear modulus beyond which the instability is regularized by deviatoric stiffness Fig. 3-22.

Having highlighted one at a time the role of the nondimensional parameters, the parameter space is studied in more detail by varying the active parameters together two at a time. Experimentally it is easiest to explore the space spanned by $\bar{P}$ and $\bar{t}_{pulse}$ simply by varying the applied laser loading. Increasing either of these parameters enhances undulation growth in the first pressure cycle. In Fig. 3-23 the peak

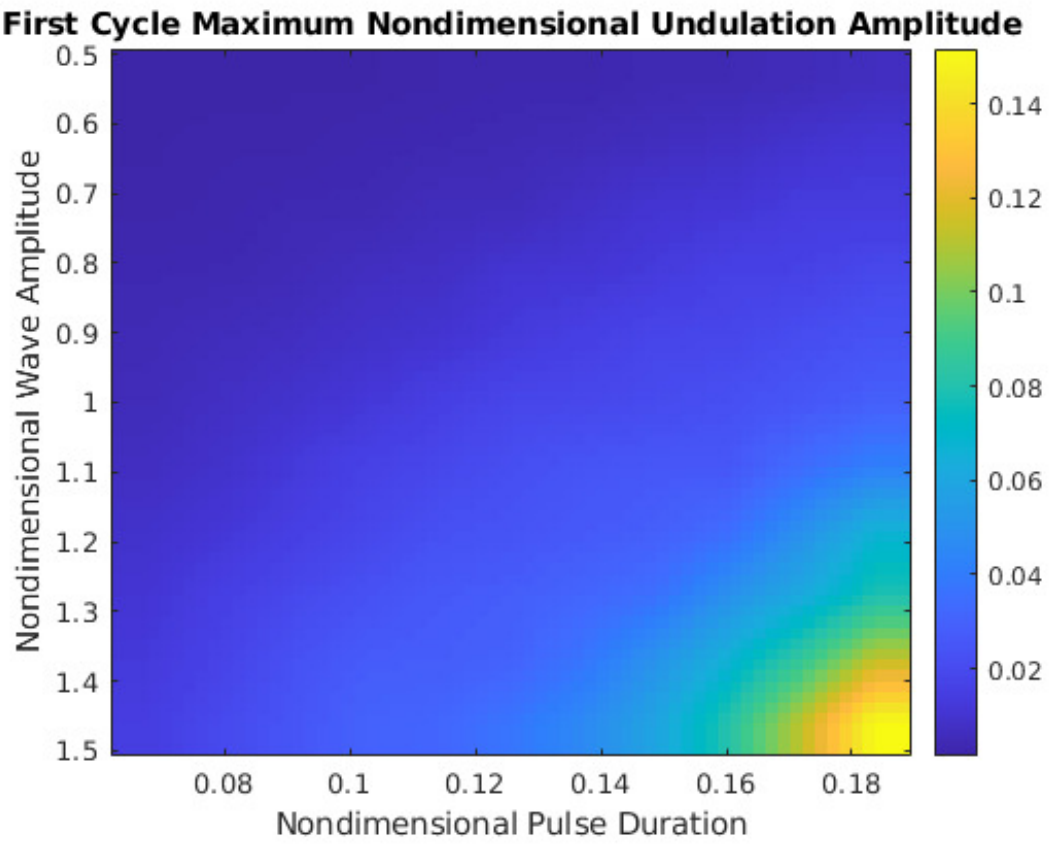

Figure 3-23: Maximal $\bar{A}$ during the first cycle ($\bar{t}$ between 0 and 4) as $\bar{P}$ and $\bar{t}_{pulse}$ varying independently. 121 simulations are used in this parameter study. Results shown using bilinear interpolation.

undulation amplitude $\bar{A}$ during the first pressure cycle ($\bar{t}$ between 0 and 4) is plotted as a function of the pulse duration $\bar{t}_{pulse}$ along the horizontal axis and the pulse amplitude $\bar{P}$ along the vertical axis. The profile of the colored region in the bottom right of this plot indicates the scaling of undulation amplitude with the product $\bar{P} \times \bar{t}_{pulse}$ which is to first order directly proportional to the energy injected into the simulation.

Besides this easily controlled parameter space, the spaces spanned by $\bar{\gamma}$ and either $\bar{P}$ or $\bar{t}_{pulse}$ are studied using our computational framework Fig. 3-24 and Fig. 3-25. It is difficult to tune the stiffening in a material's equation of state in a manner that would allow for exploration of this parameter space experimentally. Nevertheless, one can observe that increasing the boundary condition parameters $\bar{P}$ or $\bar{t}_{pulse}$ always increases undulation growth. Increasing $\bar{\gamma}$ at moderate levels of the boundary condition

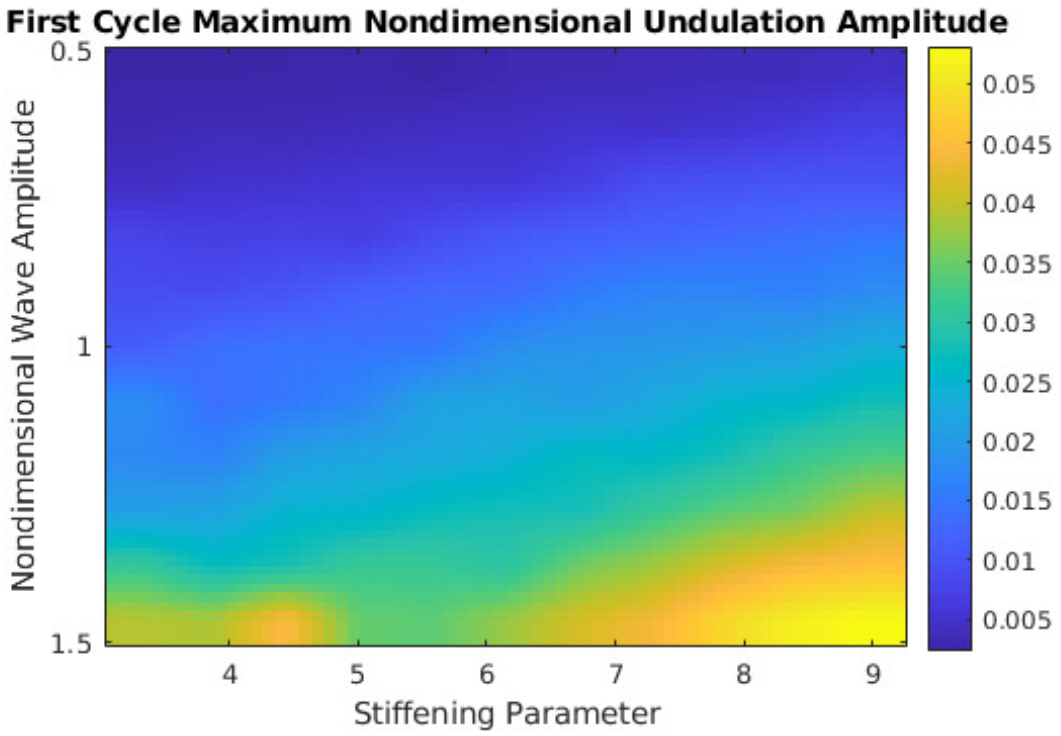

Figure 3-24: Maximal $\bar{A}$ during the first cycle ($\bar{t}$ between 0 and 4) as $\bar{P}$ and $\bar{\gamma}$ varying independently. 121 simulations are used in this parameter study. Results shown using bilinear interpolation.

parameters also increases undulation growth by decreasing P_{max} and enhancing softening effects. At large values of the boundary condition parameters the dependence on the stiffening parameter is non-monotonic. The shock capturing scheme likely needs to be retuned to stabilize such shocks.

3.5.2 Undulation Wavelength Dependence on Shock Parameters

Motivated by the apparent differences in amplitude and wave-number found in the experimentally observed instabilities for different laser pulse amplitudes shown in appendix C, variations in the loading parameters t_{pulse} and P_{pulse} are considered in more detail in this section. It is found that when increasing the parameter P_{pulse} the model produces larger instabilities with sharper, cusp-like features when compared with the smooth and fairly periodic protrusions found in the initial calculations and experi-

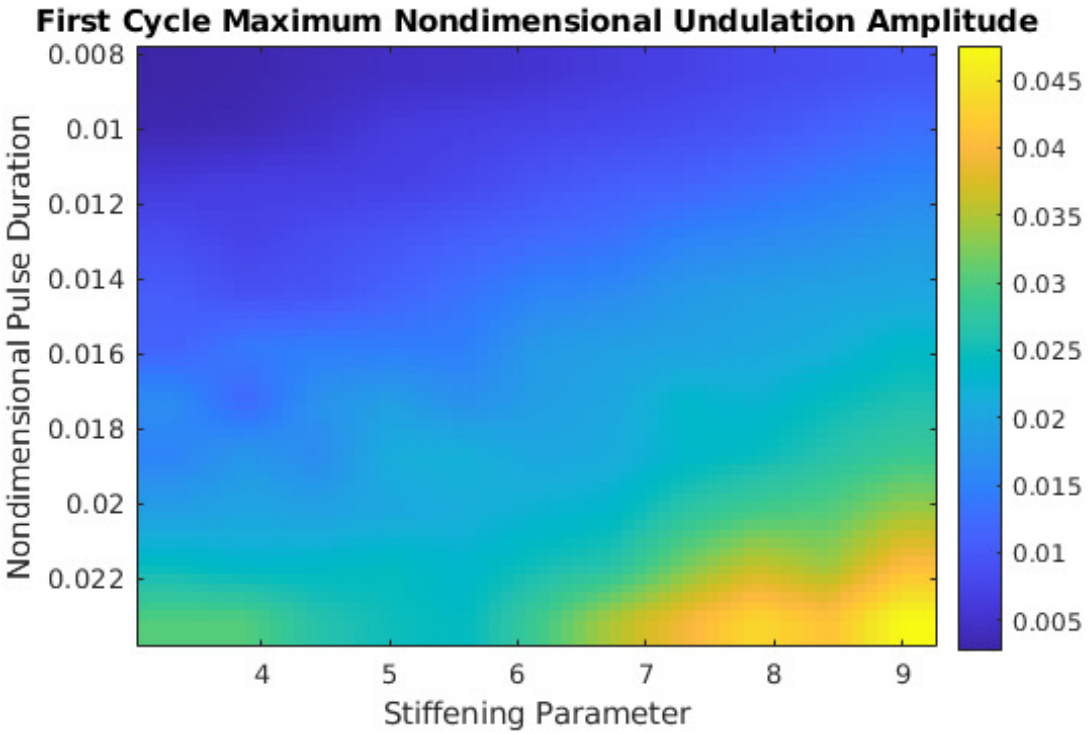

Figure 3-25: Maximal $\bar{A}$ during the first cycle ($\bar{t}$ between 0 and 4) as $\bar{t}_{pulse}$ and $\bar{\gamma}$ varying independently. 121 simulations are used in this parameter study. Results shown using bilinear interpolation.

mental results. In Fig. 3-26, sequences of snapshots taken from four simulations of various $\bar{P}$ are presented in descending order down the figure. Consistent with the finding of the previous section, instabilities increase noticeably as $\bar{P}$ is incremented geometrically across the figure. In particular, only the bottom right snapshot shows significant undulation formation. Additionally, it is found that at $\bar{t} = 5$ the largest amplitude shock simulation shows a larger tensile core than the weak shock simulations, which indicates that the larger amplitude shock model lags behind the weaker shock simulations due to softening upon wave reflection.

More, sharper undulations develop when $\bar{P}$ is large due to the activation of higher wave-number instability modes. At larger pulse amplitudes the preferential growth of wave-numbers near 20 is not nearly as apparent. Fig. 3-27 presents a direct comparison between the modal analysis of the initial model shown in Fig. 3-13 and the modal analysis obtained from simulations with a doubled pulse amplitude and highlights that instability wave-numbers are not clustered as closely in the case of the stronger shock. In particular, the first few most active Fourier modes in the initial simulation have wave-numbers below 20, but after doubling the pulse amplitude the most active mode number is over 20. Similarly, the modal growth rates at $\bar{t}$ between 2 and 3 are clustered around larger mode numbers.

Varying the boundary condition parameter t_{pulse} also demonstrates similar effects on the most active mode number Fig. 3-28. It is found that larger pulse durations produce larger shocks and larger high wave-number instability amplitudes. These additional and larger high wavenumber instability modes are prominent in the bottom right of Fig. 3-29 where more surface undulations with a cusp-like appearance are displayed. The original parameter was selected to correspond to the duration of the applied laser pulse, but it is conceivable that the ablation zone exerts mechanical loads on the interior region of the hydrogel for a prolonged time after the laser pulse ends. In contrast to the pulse amplitude parameter $\bar{P}$, when maintaining the applied loading for much larger durations it is found that the shock can traverse the entire domain multiple times before the pressure is released Fig. 3-29, yet instabilities do not form until $\bar{t}_p$.

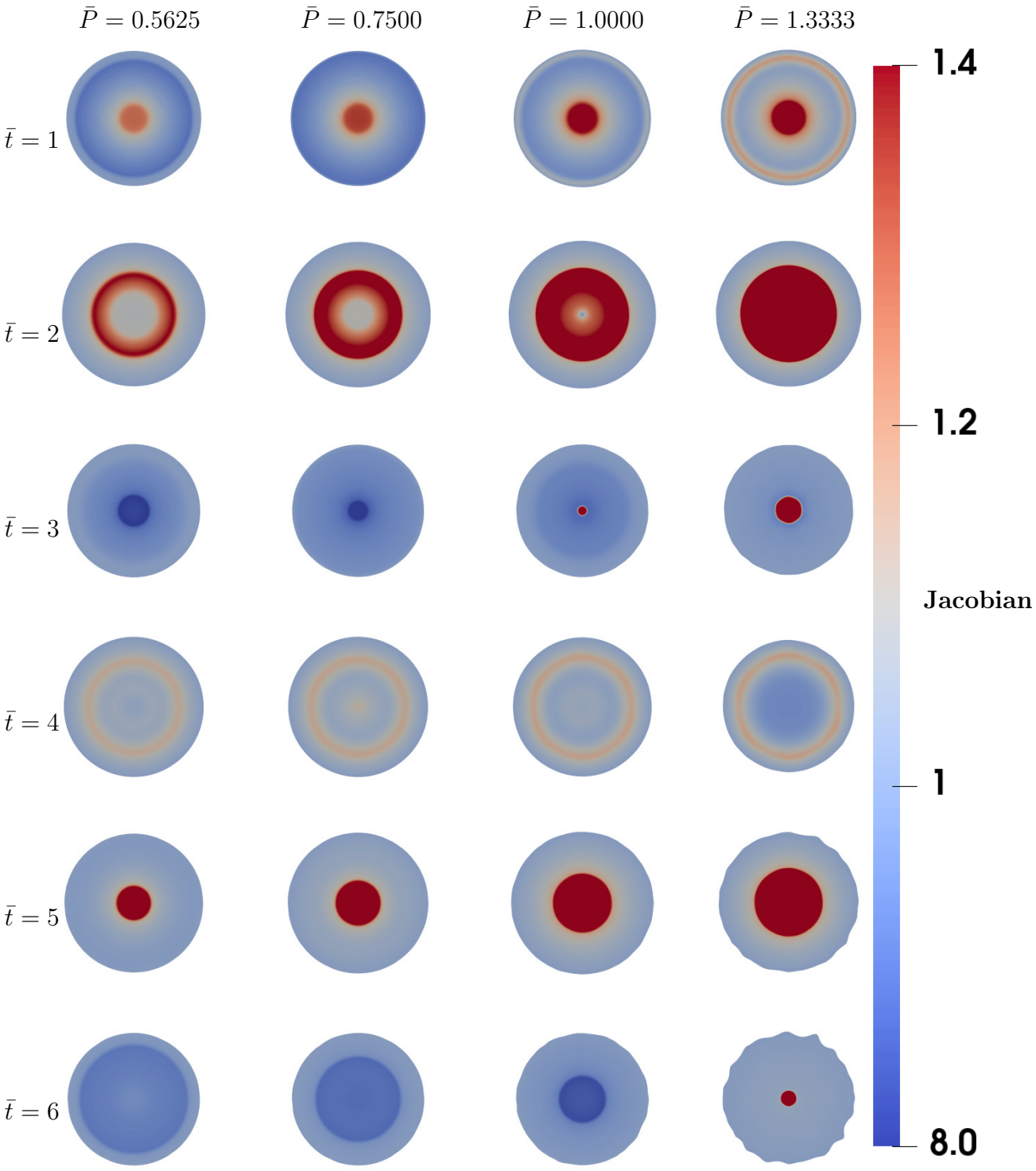

Figure 3-26: Jacobians plotted in the deformed configuration for a variety of times $\bar{t}$ and wave amplitudes $\bar{P}$. $\gamma = 6.15$ and $\frac{t_{pulse}}{R}\sqrt{\frac{\kappa}{\rho}} = 0.1$ From left to right the $\bar{P}$ increase geometrically by a factor of $\frac{4}{3}$ beginning at 0.5625. From top to bottom the nondimensional simulation times $\frac{t}{R}\sqrt{\frac{\kappa}{\rho}}$ increase by 1 starting at 1.

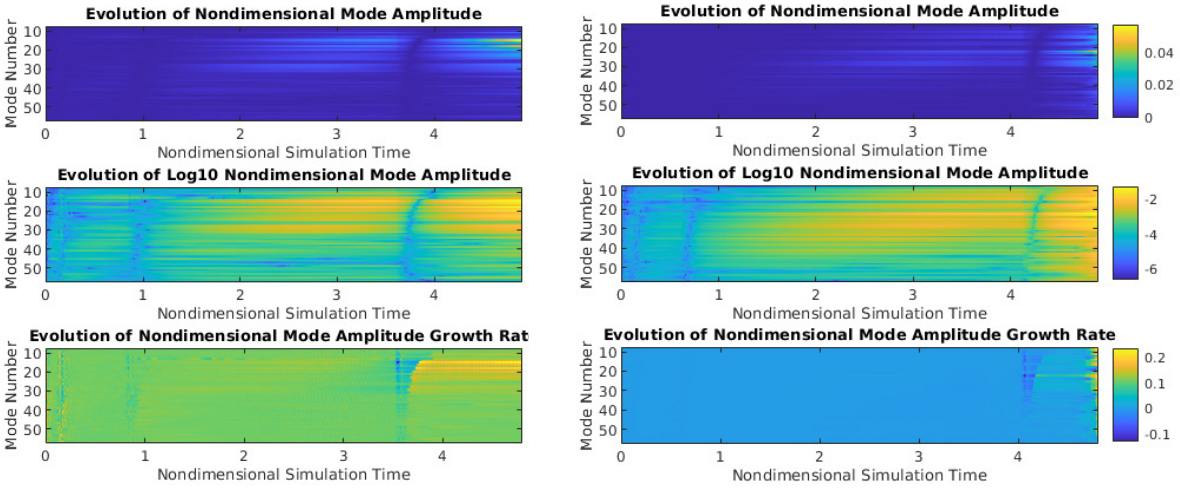

Figure 3-27: Left: reference modal analysis. Right: doubled pressure amplitude. Note that increasing the amplitude increases the wave-number and amplitude of surface undulations and also produces modal growth rates that are not clustered as tightly in a particular range. This manifests as numerous, sharp undulations along the boundary.

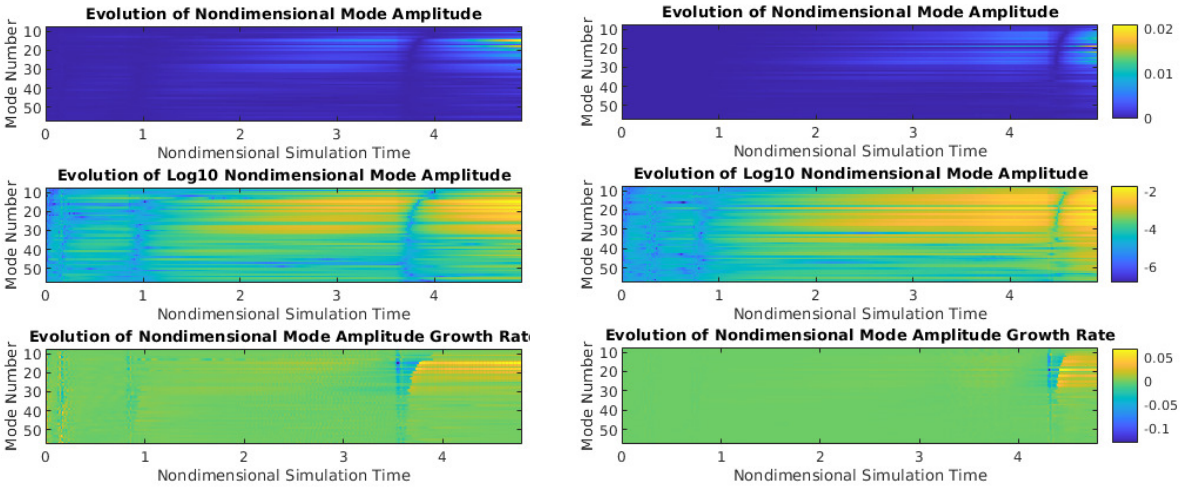

Figure 3-28: Left: reference modal analysis. Right: doubled pulse duration. Like in the case of doubling the pulse amplitude, the higher energy wave produces larger amplitude higher wave-number instabilities which are not as closely grouped in wave-number.

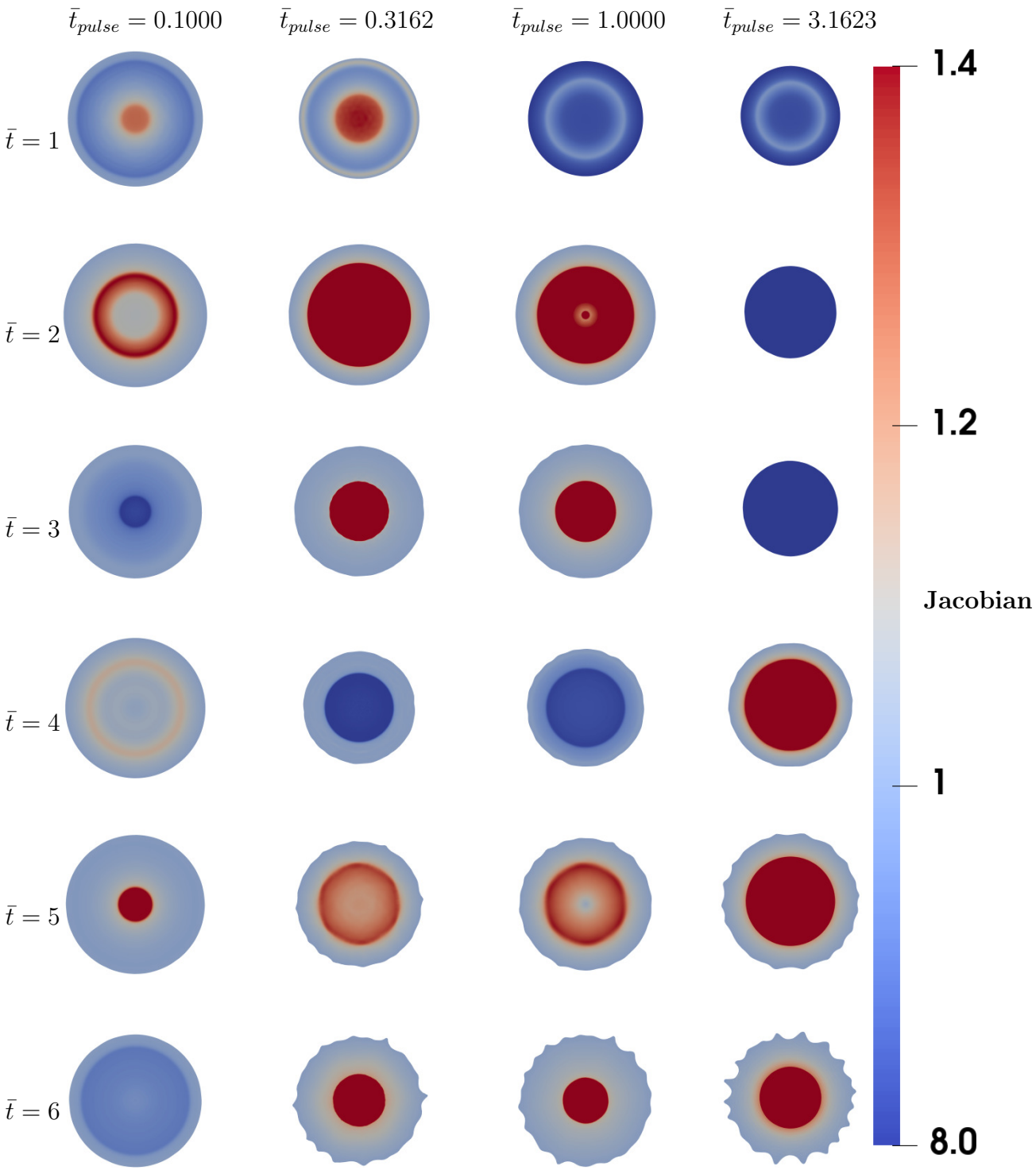

Figure 3-29: Jacobians plotted in the deformed configuration for a variety of times $\bar{t}$ and pulse durations $\bar{t}_{pulse}$. $\gamma = 6.15$ and $\bar{P} = 0.5625$. From left to right the $\bar{t}_{pulse}$ increase geometrically by a factor of $\sqrt{10}$ beginning at 0.1. From top to bottom the nondimensional simulation times increase by 1 starting at 1.

This finding highlights the importance of nonlinear softening and dispersion in our calculations. When pressurized, there is no significant softening leading to hoop compression under radial tension. Classic cylindrical Rayleigh-Taylor or parametric instabilities may develop regardless of the scale of the hydrostatic stress because these instabilities do not require nonlinear volumetric material response, but the instability shown in the present study requires sufficiently large pressures and waves to necessitate dispersion upon shock reflection. Conversely, Richtmyer-Meshkov instabilities also require a nonlinear equation of state but develop due to baroclinic effects induced by compressive shock waves. Even in the setting of 'reshocked' Richtmyer-Meshkov instability, where first a converging and then a diverging wave drive instability growth, the domain does not typically enter the tensile phase of vibrations [50, 96].

In summary, the wave-number of instability is typically of a moderate value near 20 because the hoop compression mechanism preferentially amplifies these modes. In the initial stages of the calculation when shocks are strong, many additional modes are activated. For increased values of the boundary loading parameters P_{pulse} and t_{pulse}, the inertial effects are enhanced and multiple, large wave-number instability modes are activated leading to cusp shaped instabilities. Increasing t_{pulse} sufficiently can delay instability formation by limiting the possibility of tensile softening until the loading is released.

Chapter 4

Summary and Conclusions

We have proposed and utilized a computational model for the simulation of a new class of elastodynamic instabilities which arise along the surface of curved soft materials experiencing internal shock reflections. These new dynamic instabilities appear after multiple shock reflections which endows them with a characteristic timescale of growth that exceeds the acoustic timescale. In contrast to parametric instabilities in soft solids [74, 75], the new mechanism relies on nonlinearity in the equation of state, in addition to geometric nonlinearity, to produce surface undulations. In particular, softening of the equation of state plays a pivotal role in generating instability formation. Typical shock-induced instabilities, such as Richtmyer-Meshkov, develop under the action of compression waves and are insensitive to a material's ultimate tensile strength.

The recent discovery by members of Professor Keith Nelson's research group at the MIT Institute for Soldier Nanotechnologies of laser-induced surface undulations along the boundary of soft hydrogel specimens motivated this study. The newly discovered instabilities form only along the external boundary of hydrogel cylinders because the new mechanism requires multiple internal reflections. The external laser ablation zone surface does not experience oscillatory loads or hoop compression and does not exhibit the new mechanism. Furthermore, the well known increase of the critical cavitation stress with shear stiffness allows a hydrogel to develop the new

instability whereas pure water cannot. It should be emphasized that this instability has only been described recently since it occurs along the boundary of shocked soft solids with small radii of curvature. The new experimental setup considered at the MIT Institute for Soldier Nanotechnologies is ideally suited for exploring this regime of mechanical response.

Soft material response to large amplitude loading has potential biomedical applications to the study of shock wave lithotripsy [101, 121, 129, 130], histotripsy cancer therapies [131–133], traumatic brain [134, 135] and other soft internal organ injuries [136]. Additionally, laser cavitation experiments similar to those modeled in this thesis have recently furnished a valuable tool for the characterization of soft material constitutive models, but only when such experiments maintain symmetry [84]. Observation and simulation of the new class of shock induced surface instabilities considered here motivates continued study of nonlinear waves in soft materials which may lead to progress in these important areas.

Appendix A

Calculation With Non-Circular Geometries

In this thesis, it is found that domain curvature plays a significant role in surface eruption. Motivated by this finding, a simulation of a simple geometry with non constant surface curvature is presented in this appendix. An applied pressure equal to the 2 GPa bulk modulus is sustained for 20 ns along the boundary of a 540 μm square domain with rounded corners of radius 90 μm. The same constitutive model and shock capturing scheme presented in chapter 2 is employed here. The simulation are presented in Fig. A-1 and they show that the pressure is amplified in regions of curvature which causes the curved part of the shock front to travel faster than the noncurved part [92, 137]. At 76.2 ns, transverse shocks form near triple points in the shock front. Experimental evidence indicates transverse shocks play a key role in focusing pressure inside the spike of a Richtmyer-Meshkov instability. Long, skinny spikes and rounder bubbles typically form in Richtmyer-Meshkov (as opposed to the sinusoidal instability of Taylor's instability) because transverse shocks focus the pressure into the spikes [49]. The faster speed of inwards curved shocks (and slower speeds of shocks which curve outwards) causes the superstability of shock fronts which Richtmyer attributes to Roberts [47] and which causes the cycles around the asymptotic growth rate on the right side of Fig. 3-12.

It is interesting to observe that from 25.4 to 50.8 ns, the higher pressures in

the corners causes the four corners to protrude outwards, but when the hydrostatic tension is focused in the corners these four protrusions are retracted leading to eight protrustions (two on either side of each corner) which persist from 101.6-203.2 ns. In the circular geometry, this effect is the phase reversal which causes a periodic sequence of protrusions to invert and become approximately the same instability modes 180 degrees out of phase. In this geometry, it is found that four protrusions become 8, and then at later times 16. To the best of our knowledge, such shock driven dynamic period doubling has yet to be reported.

Vorticity and rotation distribution at 50.8 ns are also presented in Fig. A-2. It is found that the shock distributes vorticity in its wake which curls material into the region of high pressure. Consistent with the theories from gas dynamics, shocks in soft solids also induce significant vorticity near regions of high shock curvature [138]. The shock capturing scheme stabilizes the rotation field better than the vorticity field which has some slight oscillations.

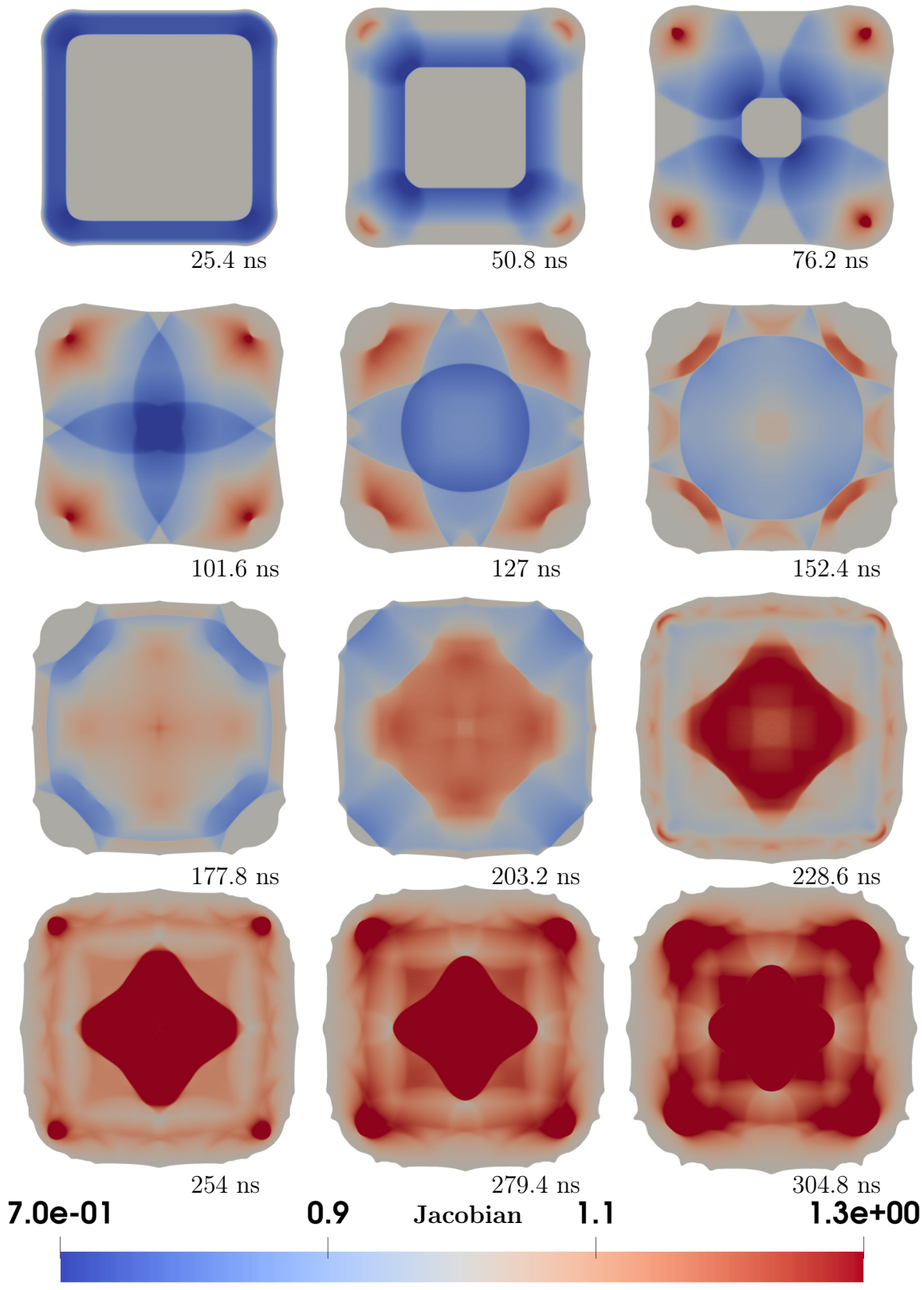

Figure A-1: Shock dynamics in a square domain. Frames show the Jacobian of deformation every 25.4 ns.

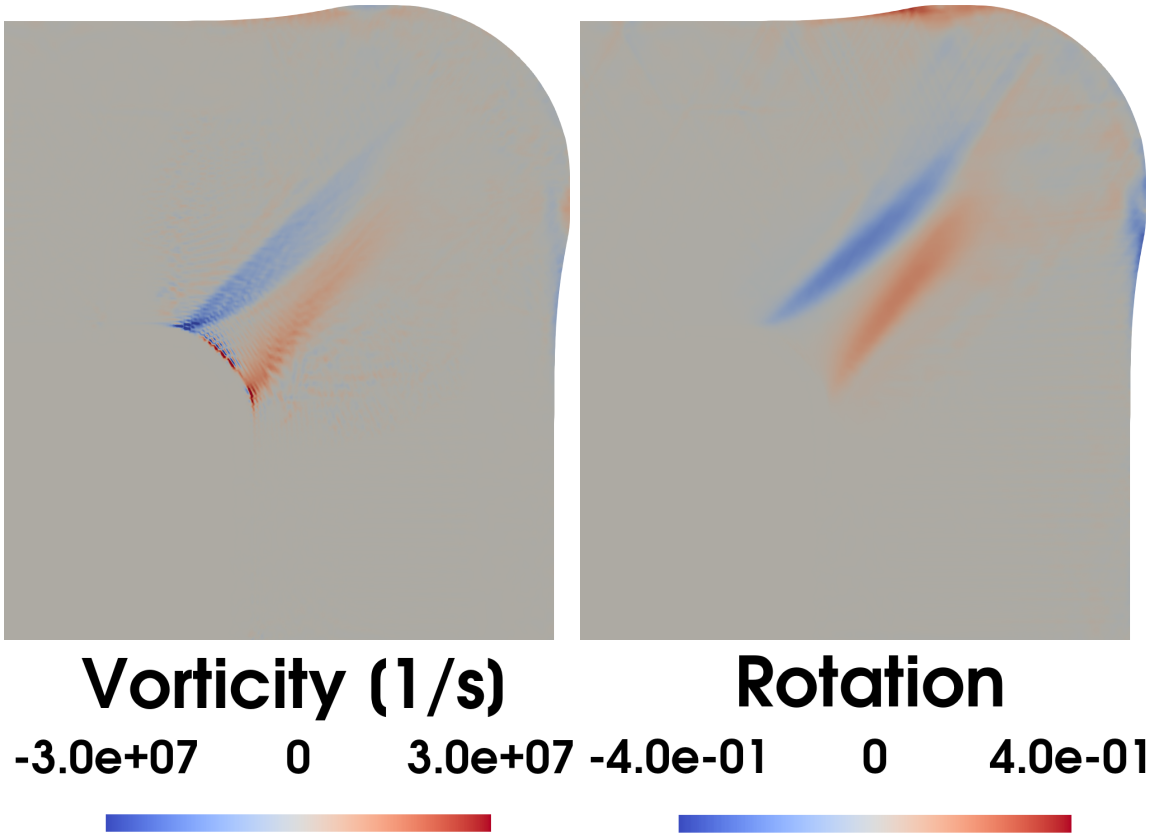

Figure A-2: Vorticity (curl of the velocity field) and rotation (curl of the displacement field) at 50.8 ns.

Appendix B

Validity of Plane Strain Assumptions

To determine the accuracy of the plane strain assumptions considered in chapter 3, axisymmetric calculations of the out of plane displacements of the glass slides were performed. The numerical models simulate the ablation zone as a Gaussian distributed vertical force with a square wave profile in time. Polyacrylamide hydrogels typically stick to glass slides [2], and it is possible that any deflection of the glass out of the plane of the experiment could be expected to strain the gel cylinder axially. It was found that the timescale for wave propagation across the slides is on the order of 100 ns. Since the bulk modulus of glass is far larger than the pressures observed in these simulations it is unlikely that out of plane deformation is significant early on in the experiment.

Nevertheless, if the loading in the ablation ring is sustained indefinitely at even moderate values such as 200 MPa, then vertical velocity in the glass is expected to be on the order of 3 or 4 meters per second which could cause axial strains in the hydrogel on the order of 10 % in less than a microsecond. Snapshots of the numerical simulation with this indefinitely sustained pressure boundary condition are presented in Fig. B-1. It is likely that the gel would delaminate off the glass (which is observed in some experiments) under such large stretching. In any event dynamic models of elastic fringe and fingering instability have shown high strain rate stretching is does not form elastic instabilities [35]. Furthermore, if the new experiments were strongly impacted by out of plane effects they should demonstrate fringe or fingering on both

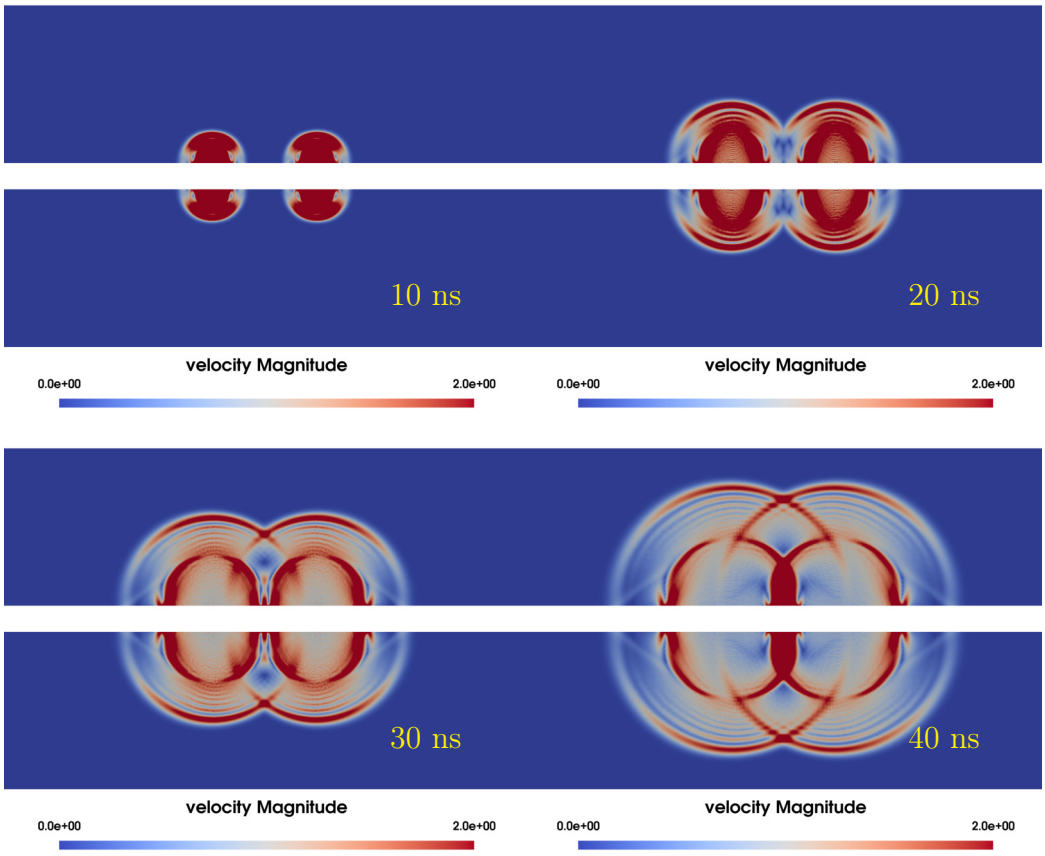

Figure B-1: Out of plane stress velocity waves in the glass slides. The boundary condition is a sustained 200 MPa Gaussian pulse pressure applied vertically along the ring. The Gaussian standard deviation is $10\mu m$, and it is centered at 100 μm. Here detailed snapshots of the computational results are presented 10 ns apart in time. Using symmetry only half of the upper glass slide is modeled.

sides of the ablation zone, which they do not.

Appendix C

Additional Experimental Results

Additional experimental results were provided by Dmitro Martynowych who conducted the new experiments at the MIT Institute for Soldier Nanotechnologies. We present them here because they demonstrate the variation the undulation amplitude and wave-number which is studied numerically in this thesis. Furthermore, they clearly demonstrate the important finding that water does not demonstrate the surface undulations of interest whereas hydrogel does.

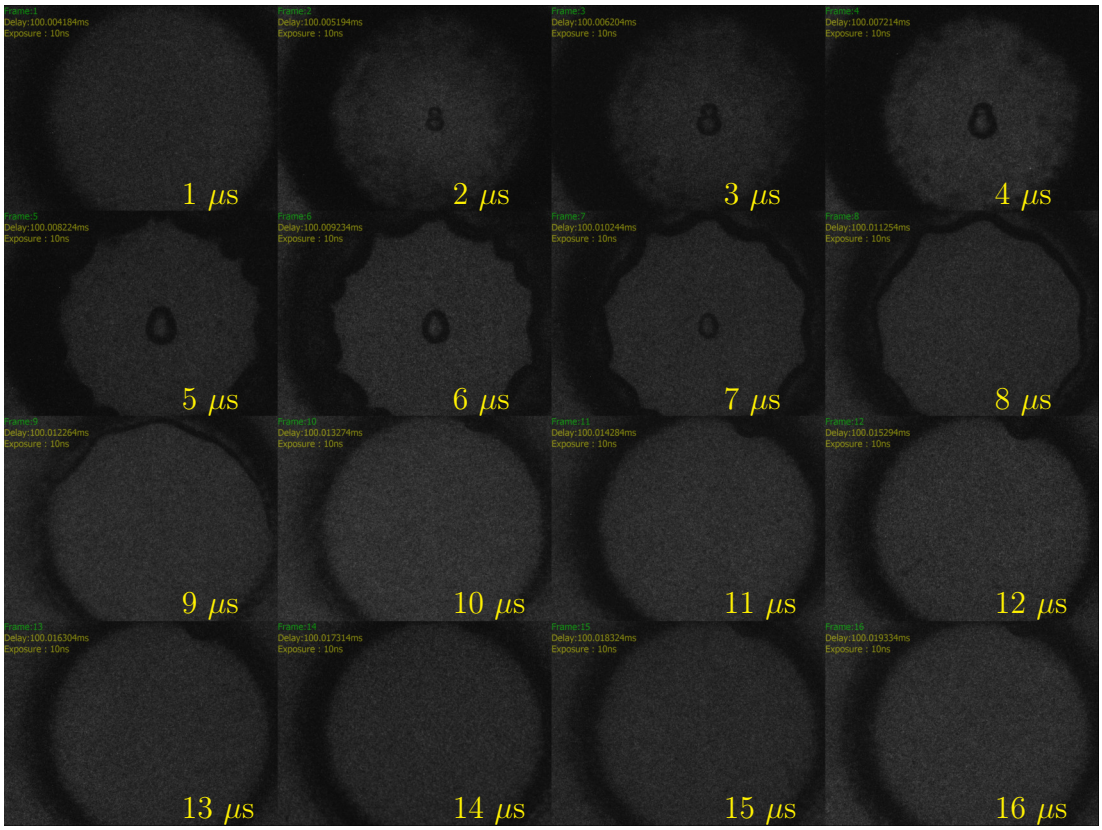

Figure C-1: The laser pulse energy is 230 μJ. The material is polyacrylamide hydrogel

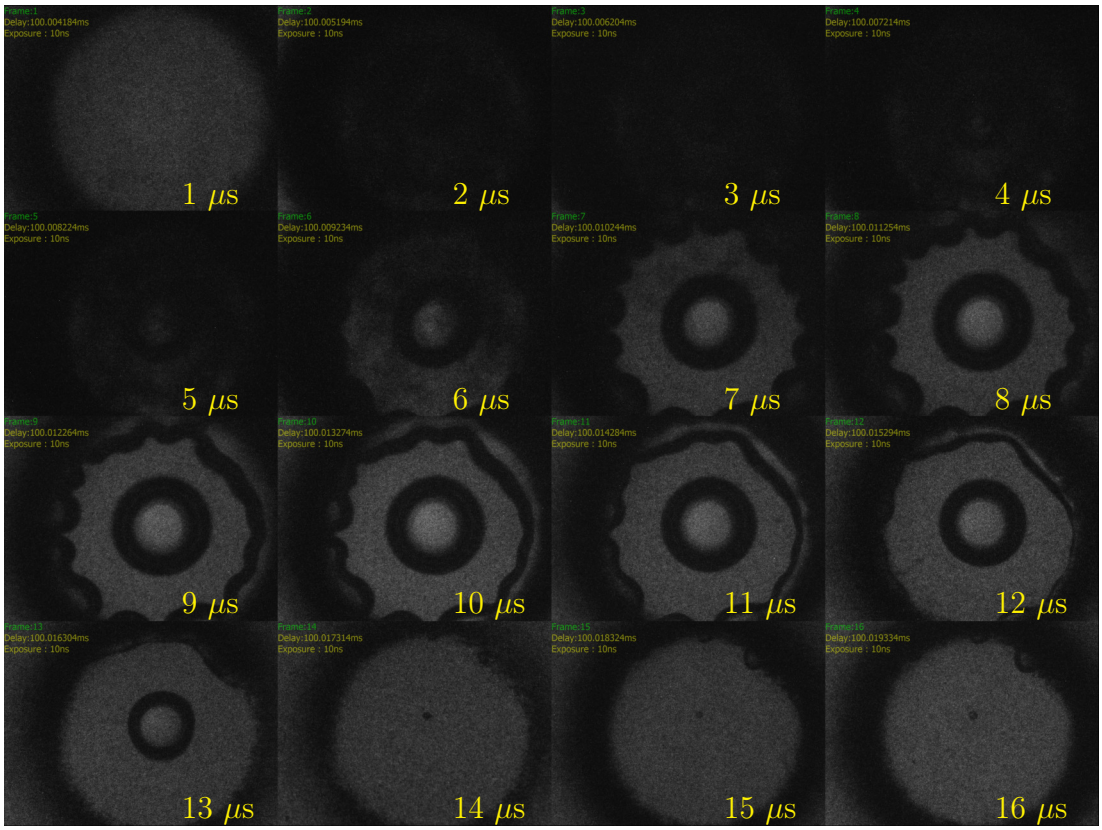

Figure C-2: The laser pulse energy is 360 μJ. The material is polyacrylamide hydrogel

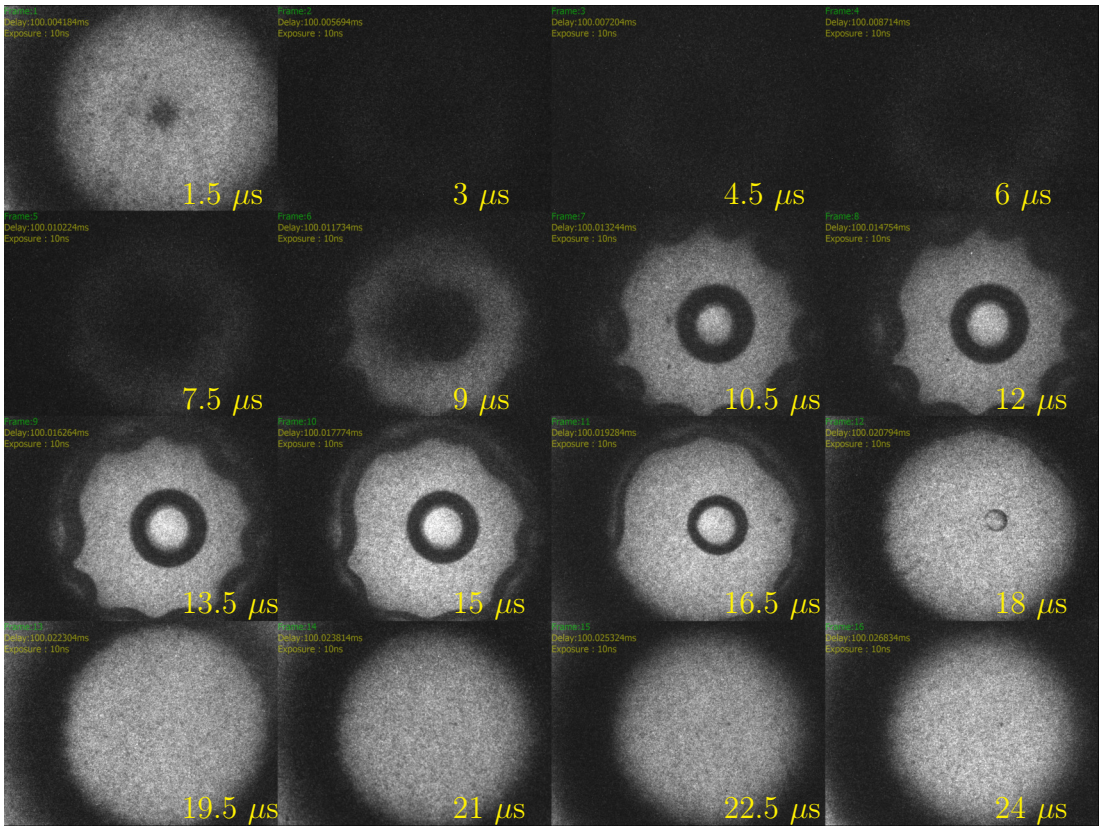

Figure C-3: The laser pulse energy is 530 μJ. The material is polyacrylamide hydrogel

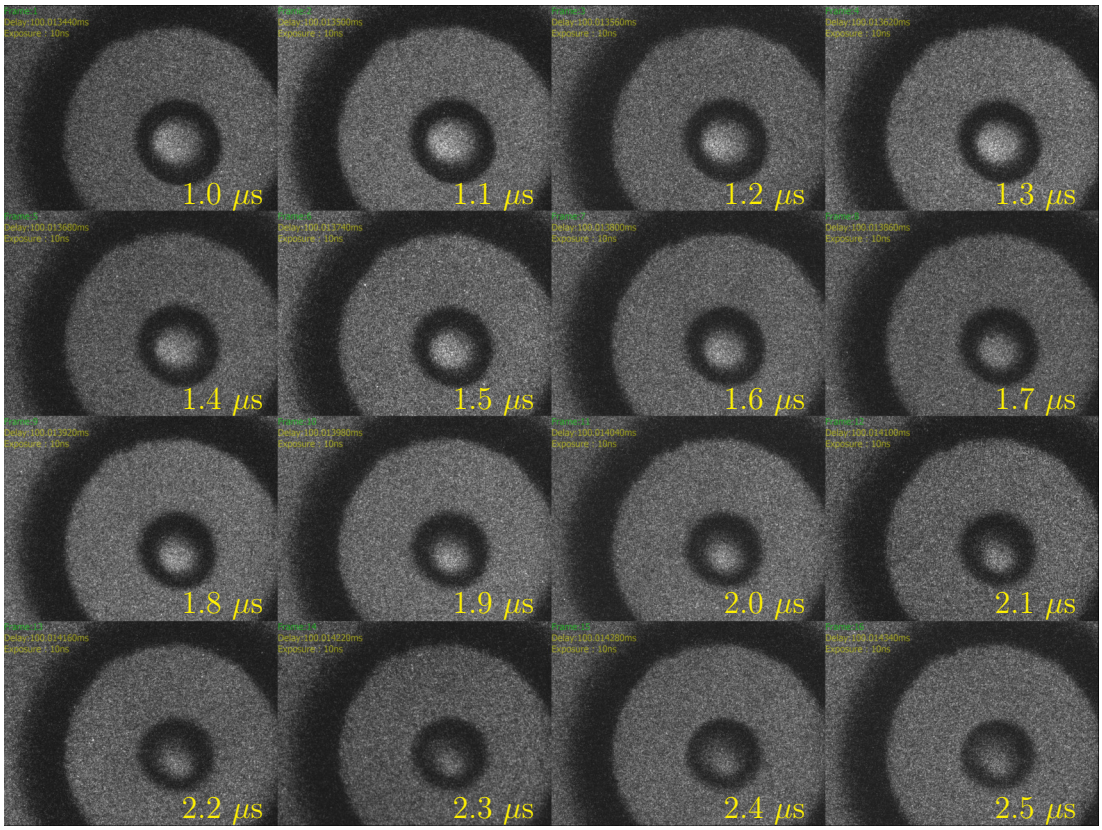

Figure C-4: The laser pulse energy is 240 μJ. The material is polyacrylamide hydrogel

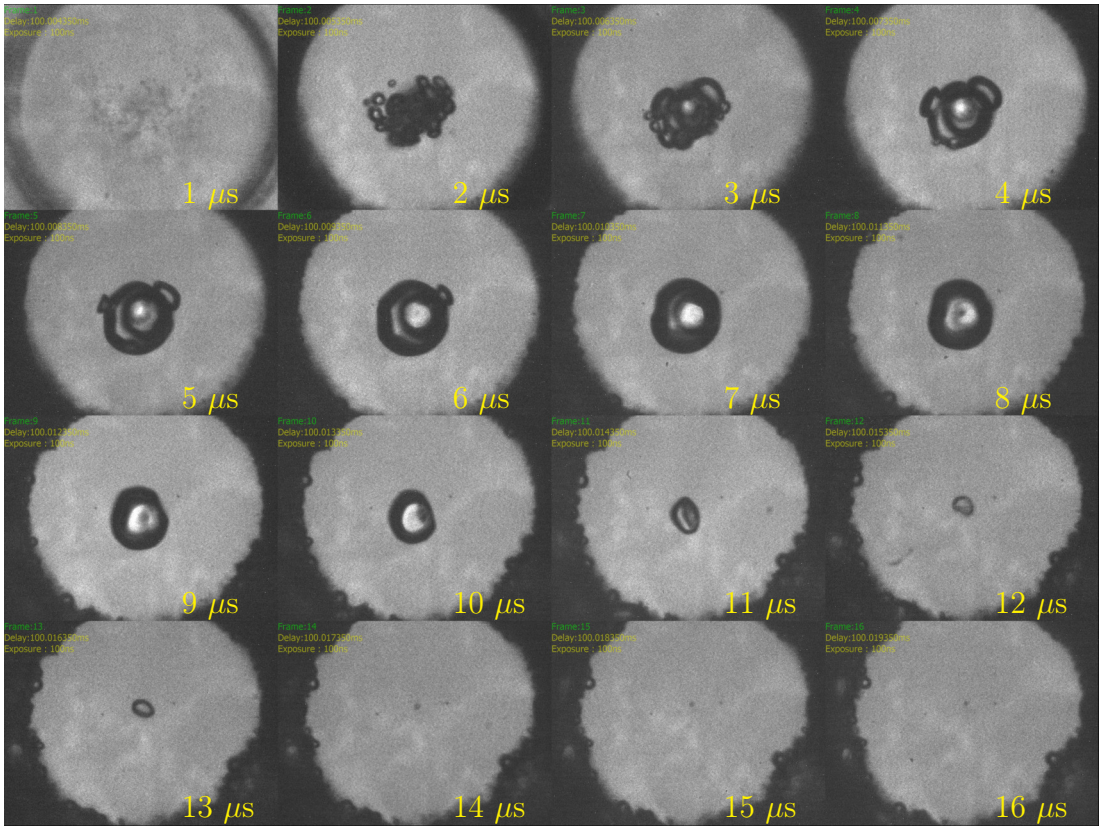

Figure C-5: The laser pulse energy is 850 μJ. Water is used for comparison with the hydrogel results. In contrast to the typically solitary gel cavities shown above, water forms many smaller cavities which coalesce into one cavity over time. Also note that water does not exhibit boundary undulations.

Bibliography

[1] Chunhui Li et al. "Determining elastic properties of skin by measuring surface waves from an impulse mechanical stimulus using phase-sensitive optical coherence tomography". In: *Journal of The Royal Society Interface* 9.70 (2012), pp. 831–841. DOI: 10.1098/rsif.2011.0583. eprint: https://royalsocietypublishing.org/doi/pdf/10.1098/rsif.2011.0583.

[2] John S. Biggins et al. "Digital instability of a confined elastic meniscus". In: *Proceeding of the National Academy of Sciences* 110 (31 2013), pp. 12545–12548. DOI: 10.1073/pnas.1302269110.

[3] Constantino Creton and Matteo Ciccotti. "Fracture and adhesion of soft materials: a review". In: *Reports on Progress in Physics* 79.4 (2016). DOI: 10.1088/0034-4885/79/4/046601.

[4] Kenneth R. Shull. "Contact mechanics and the adhesion of soft solids". In: *Materials Science and Engineering: R: Reports* 36.1 (2002), pp. 1–45. ISSN: 0927-796X. DOI: https://doi.org/10.1016/S0927-796X(01)00039-0.

[5] K. E. Garcia, C. D. Kroenke, and P. V. Bayly. "Mechanics of cortical folding: stress, growth and stability". In: *Philosophical Transactions of the Royal Society B: Biological Sciences* 373.1759 (2018), p. 20170321. DOI: 10.1098/rstb.2017.0321.

[6] Bo Li et al. "Mechanics of morphological instabilities and surface wrinkling in soft materials: a review". In: *Soft Matter* 8 (21 2012), pp. 5728–5745. DOI: 10.1039/C2SM00011C.

[7] Michel C Milinkovitch Sophie A Montandon Anamarija Fofonjka. "Elastic instability during branchial ectoderm development causes folding of the Chlamydosaurus erectile frill". In: (2019). DOI: 10.7554/eLife.44455.

[8] P. Ciarletta, M. Destrade, and A. L. Gower. "Shear instability in skin tissue". In: *Quarterly Journal of Mechanics and Applied Mathematics* 66.2 (2013), pp. 273–288. DOI: 10.1093/qjmam/hbt007.

[9] Bo Li et al. "Surface wrinkling of mucosa induced by volumetric growth: Theory, simulation and experiment". In: *Journal of the Mechanics and Physics of Solids* 59.4 (2011), pp. 758–774. ISSN: 0022-5096. DOI: https://doi.org/10.1016/j.jmps.2011.01.010.

[10] P Tracqui. "Biophysical models of tumour growth". In: *Reports on Progress in Physics* 72.5 (Apr. 2009), p. 056701. DOI: 10.1088/0034-4885/72/5/056701.

[11] Julien Dervaux et al. "Shape Transition in Artificial Tumors: From Smooth Buckles to Singular Creases". In: *Phys. Rev. Lett.* 107 (1 July 2011), p. 018103. DOI: 10.1103/PhysRevLett.107.018103.

[12] Robert M. Sutherland. "Cell and Environment Interactions in Tumor Microregions: The Multicell Spheroid Model". In: *Science* 240.4849 (1988), pp. 177–184. ISSN: 00368075, 10959203.

[13] Shengqiang Cai et al. "Osmotic collapse of a void in an elastomer: breathing, buckling and creasing". In: *Soft Matter* 6 (22 2010), pp. 5770–5777. DOI: 10.1039/C0SM00451K.

[14] Bo Li et al. "Surface Wrinkling Patterns on a Core-Shell Soft Sphere". In: *Phys. Rev. Lett.* 106 (23 June 2011), p. 234301. DOI: 10.1103/PhysRevLett.106.234301.

[15] E. Southern and A. G. Thomas. "Effect of constraints on the equilibrium swelling of rubber vulcanizates". In: *Journal of Polymer Science Part A: General Papers* 3.2 (1965), pp. 641–646. DOI: https://doi.org/10.1002/pol.

1965.100030220. eprint: https://onlinelibrary.wiley.com/doi/pdf/10.1002/pol.1965.100030220.

[16] Cui Zhibo et al. "From small wrinkles to Schallamach waves during rubber friction: In situ experiment and 3D simulation". In: *Polymer Testing* 96 (2021), p. 107084. ISSN: 0142-9418. DOI: https://doi.org/10.1016/j.polymertesting.2021.107084.

[17] E. P. Chan and A. J. Crosby. "Fabricating Microlens Arrays by Surface Wrinkling". In: *Advanced Materials* 18.24 (2006), pp. 3238–3242. DOI: https://doi.org/10.1002/adma.200601595.

[18] Dinesh Chandra, Shu Yang, and Pei-Chun Lin. "Strain responsive concave and convex microlens arrays". In: *Applied Physics Letters* 91.25 (2007), p. 251912. DOI: 10.1063/1.2827185.

[19] Ramses V. Martinez et al. "Robotic Tentacles with Three-Dimensional Mobility Based on Flexible Elastomers". In: *Advanced Materials* 25.2 (2013), pp. 205–212. DOI: https://doi.org/10.1002/adma.201203002. eprint: https://onlinelibrary.wiley.com/doi/pdf/10.1002/adma.201203002.

[20] Xuanhe Zhao and Zhigang Suo. "Theory of Dielectric Elastomers Capable of Giant Deformation of Actuation". In: *Phys. Rev. Lett.* 104 (17 Apr. 2010), p. 178302. DOI: 10.1103/PhysRevLett.104.178302.

[21] Hyunwoo Yuk et al. "Hydraulic hydrogel actuators and robots optically and sonically camouflaged in water". In: *Nature Communications* 8.1 (Feb. 2017), p. 14230. ISSN: 2041-1723. DOI: 10.1038/ncomms14230.

[22] Hyunwoo Yuk et al. "Skin-inspired hydrogel–elastomer hybrids with robust interfaces and functional microstructures". In: *Nature Communications* 7.1 (June 2016), p. 12028. ISSN: 2041-1723. DOI: 10.1038/ncomms12028.

[23] Won Mook Choi et al. "Biaxially Stretchable "Wavy" Silicon Nanomembranes". In: *Nano Letters* 7.6 (2007). PMID: 17488053, pp. 1655–1663. DOI: 10.1021/nl0706244.

[24] Dae-Hyeong Kim and John A. Rogers. "Stretchable Electronics: Materials Strategies and Devices". In: *Advanced Materials* 20.24 (2008), pp. 4887–4892. DOI: https://doi.org/10.1002/adma.200801788.

[25] Jeong-Ho Lee, Harold S. Park, and Douglas P. Holmes. "Elastic Instabilities Govern the Morphogenesis of the Optic Cup". In: *Phys. Rev. Lett.* 127 (13 Sept. 2021), p. 138102. DOI: 10.1103/PhysRevLett.127.138102.

[26] Cheng-Ji Zhou et al. "Ocular coloboma and dorsoventral neuroretinal patterning defects in Lrp6 mutant eyes". In: *Developmental Dynamics* 237.12 (2008), pp. 3681–3689. DOI: https://doi.org/10.1002/dvdy.21770. eprint: https://anatomypubs.onlinelibrary.wiley.com/doi/pdf/10.1002/dvdy.21770.

[27] Helena Lee, Rizwana Khan, and Michael O'Keefe. "Aniridia: current pathology and management". In: *Acta Ophthalmologica* 86.7 (2008), pp. 708–715. DOI: https://doi.org/10.1111/j.1755-3768.2008.01427.x. eprint: https://onlinelibrary.wiley.com/doi/pdf/10.1111/j.1755-3768.2008.01427.x.

[28] Simon E. Skalicky et al. "Microphthalmia, Anophthalmia, and Coloboma and Associated Ocular and Systemic Features: Understanding the Spectrum". In: *JAMA Ophthalmology* 131.12 (Dec. 2013), pp. 1517–1524. ISSN: 2168-6165. DOI: 10.1001/jamaophthalmol.2013.5305. eprint: https://jamanetwork.com/journals/jamaophthalmology/articlepdf/1763217/eoi130171.pdf.

[29] M. A. Biot and Geoffrey Ingram Taylor. "Folding instability of a layered viscoelastic medium under compression". In: *Proceedings of the Royal Society of London. Series A. Mathematical and Physical Sciences* 242.1231 (1957), pp. 444–454. DOI: 10.1098/rspa.1957.0187. eprint: https://royalsocietypublishing.org/doi/pdf/10.1098/rspa.1957.0187.

[30] M. A. Biot. "Surface instability of rubber in compression". In: *Applied Scientific Research, Section A* 12.2 (Mar. 1963), pp. 168–182. ISSN: 1573-1987. DOI: 10.1007/BF03184638.

[31] J.M. Ball. "Convexity conditions and existence theorems in nonlinear elasticity". In: *Arch. Rat. Mech. Anal.* 63 (1977), pp. 337–403.

[32] Bernard D. Coleman and W Noll. "On the thermostatics of continuous media". In: *Archive for Rational Mechanics and Analysis* 4.1 (1959). DOI: 10.1007/BF00281381.

[33] Clifford Truesdell and Walter Noll. *The Non-Linear Field Theories of Mechanics*. Springer, 1965.

[34] George J. Minty. "On the monotonicity of the gradient of a convex function." In: *Pacific Journal of Mathematics* 14.1 (1964), pp. 243–247. DOI: pjm/1103034377.

[35] Bianca Giovanardi et al. "A path-following simulation-based study of elastic instabilities in nearly-incompressible confined cylinders under tension". In: *Journal of the Mechanics and Physics of Solids* (2019). DOI: 10.1016/j.jmps.2019.06.020.

[36] X. Chen and John W. Hutchinson. "Herringbone Buckling Patterns of Compressed Thin Films on Compliant Substrates ". In: *Journal of Applied Mechanics* 71.5 (Nov. 2004), pp. 597–603. ISSN: 0021-8936. DOI: 10.1115/1.1756141. eprint: https://asmedigitalcollection.asme.org/appliedmechanics/article-pdf/71/5/597/5471575/597_1.pdf.

[37] Z.Y. Huang, W. Hong, and Z. Suo. "Nonlinear analyses of wrinkles in a film bonded to a compliant substrate". In: *Journal of the Mechanics and Physics of Solids* 53.9 (2005), pp. 2101–2118. ISSN: 0022-5096. DOI: https://doi.org/10.1016/j.jmps.2005.03.007.

[38] Fabian. Brau et al. "Multiple-length-scale elastic instability mimics parametric resonance of nonlinear oscillators". In: *Nature Physics* (Jan. 2011). DOI: 10.1038/nphys1806.

[39] Luka Pocivavsek et al. “Stress and Fold Localization in Thin Elastic Membranes”. In: *Science* 320.5878 (2008), pp. 912–916. DOI: 10.1126/science.1154069.

[40] Geoffrey Ingram Taylor. “The instability of liquid surfaces when accelerated in a direction perpendicular to their planes. I”. In: *Proceedings of the Royal Society of London. Series A. Mathematical and Physical Sciences* 201.1065 (1950), pp. 192–196. DOI: 10.1098/rspa.1950.0052. eprint: https://royalsocietypublishing.org/doi/pdf/10.1098/rspa.1950.0052.

[41] Aditi Chakrabarti et al. “Selection of hexagonal buckling patterns by the elastic Rayleigh-Taylor instability”. In: *Journal of the Mechanics and Physics of Solids* (2018). DOI: 10.1016/j.jmps.2018.07.024.

[42] Serge Mora et al. “The shape of hanging elastic cylinders”. In: *Soft Matter* 15 (27 2019), pp. 5464–5473. DOI: 10.1039/C9SM00625G.

[43] Serge Mora et al. “Capillarity Driven Instability of a Soft Solid”. In: *Phys. Rev. Lett.* 105 (21 Nov. 2010), p. 214301. DOI: 10.1103/PhysRevLett.105.214301.

[44] Giulia Bevilacqua et al. “Faraday waves in soft elastic solids”. In: *Proceedings of the Royal Society A: Mathematical, Physical and Engineering Sciences* 476.2241 (2020), p. 20200129. DOI: 10.1098/rspa.2020.0129. eprint: https://royalsocietypublishing.org/doi/pdf/10.1098/rspa.2020.0129.

[45] X. Shao. In: *Soft Matter* 14 (2018), pp. 7347–7353.

[46] George I. Bell. *Taylor instability on cylinders and spheres in the small amplitude approximation*. Tech. rep. Los Alamos Scientific Laboratory of the University of California, 1951.

[47] Robert D. Richtmyer. “Taylor instability in shock acceleration of compressible fluids”. In: *Communications on Pure and Applied Mathematics* 13.2 (1960), pp. 297–319. DOI: https://doi.org/10.1002/cpa.3160130207. eprint: https://onlinelibrary.wiley.com/doi/pdf/10.1002/cpa.3160130207.

[48] E. E. Meshkov. "Instability of the interface of two gases accelerated by a shock wave". In: *Fluid Dynamics* (1969), pp. 101–104. DOI: 10.1007/BF01015969.

[49] Xu Guo et al. "Effects of transverse shock waves on early evolution of multi-mode chevron interface". In: *Physics of Fluids* 32.10 (2020), p. 106101. DOI: 10.1063/5.0023100.

[50] A. López Ortega et al. "Richtmyer-Meshkov instability for elastic-plastic solids in converging geometries". In: *Journal of the Mechanics and Physics of Solids* 76 (Mar. 2015), pp. 291–324. ISSN: 00225096. DOI: 10.1016/j.jmps.2014.12.002.

[51] Y. B. Sun et al. "Effects of viscosity and elasticity on the Richtmyer-Meshkov instability". In: *Phys. Rev. E* 98 (3 Sept. 2018), p. 033102. DOI: 10.1103/PhysRevE.98.033102.

[52] Qian Chen et al. "Effects of the Atwood number on the Richtmyer-Meshkov instability in elastic-plastic media". In: *Phys. Rev. E* 99 (5 May 2019), p. 053102. DOI: 10.1103/PhysRevE.99.053102.

[53] Michael B. Prime et al. "Tantalum strength at extreme strain rates from impact-driven Richtmyer-Meshkov instabilities". In: *Phys. Rev. E* 100 (5 Nov. 2019), p. 053002. DOI: 10.1103/PhysRevE.100.053002.

[54] Y. B. Sun, R. H. Zeng, and J. J. Tao. "Elastic Rayleigh-Taylor and Richtmyer-Meshkov instabilities in spherical geometry". In: *Physics of Fluids* 32.12 (2020), p. 124101. DOI: 10.1063/5.0027909.

[55] Y. B. Sun, C. Wang, and A. R. Piriz. "A unified model to study the effects of elasticity, viscosity, and magnetic fields on linear Richtmyer-Meshkov instability". In: *Journal of Applied Physics* 128.12 (2020), p. 125901. DOI: 10.1063/5.0021223.

[56] Y. B. Sun, R. H. Zeng, and J. J. Tao. "Effects of viscosity and elasticity on Rayleigh-Taylor instability in a cylindrical geometry". In: *Physics of Plasmas* 28.6 (2021), p. 062701. DOI: 10.1063/5.0050629.

[57] T. J. Vogler and M. C. Hudspeth. "Tamped Richtmyer-Meshkov Instability Experiments to Probe High-Pressure Material Strength". In: *Journal of Dynamic Behavior of Materials* 7.2 (Feb. 2021). DOI: 10.1007/s40870-020-00288-y.

[58] S. H. R. Hosseini and K. Takayama. "Experimental study of Richtmyer-Meshkov instability induced by cylindrical shock waves". In: *Physics of Fluids* 17.8 (2005), p. 084101. DOI: 10.1063/1.1964916.

[59] A. R. Piriz et al. "Richtmyer-Meshkov instability in elastic-plastic media". In: *Phys. Rev. E* 78 (5 Nov. 2008), p. 056401. DOI: 10.1103/PhysRevE.78.056401.

[60] A. M. Binnie. "The stability of the surface of a cavitation bubble". In: *Mathematical Proceedings of the Cambridge Philosophical Society* 49.1 (1953), pp. 151–155. DOI: 10.1017/S0305004100028152.

[61] Y. Wang and Lydia Bourouiba. "Unsteady sheet fragmentation: droplet sizes and speeds". In: *Journal of Fluid Mechanics* 848 (2018), pp. 946–967.

[62] Qingyun Zeng et al. "Jetting of viscous droplets from cavitation-induced Rayleigh-Taylor instability". In: *Journal of Fluid Mechanics* 846 (2018), pp. 916–943. DOI: 10.1017/jfm.2018.284.

[63] Huidan Yu and Daniel Livescu. "Rayleigh-Taylor instability in cylindrical geometry with compressible fluids". In: *Physics of Fluids* 20.10 (2008), p. 104103. DOI: 10.1063/1.2991431.

[64] A. Antkowiak et al. "Short-term dynamics of a density interface following an impact". In: *Journal of Fluid Mechanics* 577 (2007), pp. 241–250. DOI: 10.1017/S0022112007005058.

[65] G. L. Chahine. "Interaction Between an Oscillating Bubble and a Free Surface". In: *Journal of Fluids Engineering* 99.4 (Dec. 1977), pp. 709–716. ISSN: 0098-2202. DOI: 10.1115/1.3448889. eprint: https://asmedigitalcollection.asme.org/fluidsengineering/article-pdf/99/4/709/5899794/709_1.pdf.

[66] J. M. Boulton-Stone and J. R. Blake. "Gas bubbles bursting at a free surface". In: *Journal of Fluid Mechanics* 254 (1993), pp. 437–466. DOI: 10.1017/S0022112093002216.

[67] M. S. Plesset. "On the Stability of Fluid Flows with Spherical Symmetry". In: *Journal of Applied Physics* 25.1 (1954), pp. 96–98. DOI: 10.1063/1.1721529.

[68] M. S. Plesset and T. P. Mitchell. "On the Stability of the Spherical Shape of a Vapor Cavity in a Liquid". In: *Quarterly of Applied Mathematics* 13.4 (1956), pp. 419–430. ISSN: 0033569X, 15524485.

[69] Andrea Prosperetti and Giovanni Seminara. "Linear stability of a growing or collapsing bubble in a slightly viscous liquid". In: *The Physics of Fluids* 21.9 (1978), pp. 1465–1470. DOI: 10.1063/1.862408. eprint: https://aip.scitation.org/doi/pdf/10.1063/1.862408.

[70] Y. Hao and A. Prosperetti. "The effect of viscosity on the spherical stability of oscillating gas bubbles". In: *Physics of Fluids* 11.6 (1999), pp. 1309–1317. DOI: 10.1063/1.869996.

[71] Kazuya Murakami, Renaud Gaudron, and Eric Johnsen. "Shape stability of a gas bubble in a soft solid". In: *Ultrasonics Sonochemistry* 67 (2020), p. 105170. ISSN: 1350-4177. DOI: https://doi.org/10.1016/j.ultsonch.2020.105170.

[72] Kazuya Murakami. "Spherical and Non-spherical Bubble Dynamics in Soft Matter". PhD thesis. The University of Michigan, 2020.

[73] Jin Yang et al. "Predicting complex nonspherical instability shapes of inertial cavitation bubbles in viscoelastic soft matter". In: *Phys. Rev. E* 104 (4 Oct. 2021), p. 045108. DOI: 10.1103/PhysRevE.104.045108.

[74] Fumiya Hamaguchi and Keita Ando. "Linear oscillation of gas bubbles in a viscoelastic material under ultrasound irradiation". In: *Physics of Fluids* 27.11 (2015), p. 113103. DOI: 10.1063/1.4935875.

[75] Michel Versluis et al. "Microbubble shape oscillations excited through ultrasonic parametric driving". In: *Phys. Rev. E* 82 (2 Aug. 2010), p. 026321. DOI: 10.1103/PhysRevE.82.026321.

[76] Yuning Zhang et al. "Instability of interfaces of gas bubbles in liquids under acoustic excitation with dual frequency". In: *Ultrasonics Sonochemistry* 23 (2015), pp. 16–20. ISSN: 1350-4177. DOI: https://doi.org/10.1016/j.ultsonch.2014.07.021.

[77] Kalman Klapcsik and Ferenc Hegedus. "Study of non-spherical bubble oscillations under acoustic irradiation in viscous liquid". In: *Ultrasonics Sonochemistry* 54 (2019), pp. 256–273. ISSN: 1350-4177. DOI: https://doi.org/10.1016/j.ultsonch.2019.01.031.

[78] Andrea Prosperetti. "Viscous Effects on Perturbed Spherical Flows". In: *Quarterly of Applied Mathematics* 34.4 (1977), pp. 339–352. ISSN: 0033569X, 15524485.

[79] A. Francescutto and R. Nabergoj. "Pulsation amplitude threshold for surface waves on oscillating bubbles". In: *Acustica* 41 (1978), pp. 215–220.

[80] Thomas Pezeril et al. "Direct Visualization of Laser-Driven Focusing Shock Waves". In: *Physical Review Letters* 106 (May 2011), p. 214503. DOI: 10.1103/PhysRevLett.106.214503.

[81] Dmitro Martynowych. "Materials in Extreme Conditions: Experimental Developments and Studies of Systems Far From Equilibrium". PhD thesis. The University of Michigan, 2021.

[82] D. Veysset et al. "Single-bubble and multibubble cavitation in water triggered by laser-driven focusing shock waves". In: *Phys. Rev. E* 97 (5 May 2018), p. 053112. DOI: 10.1103/PhysRevE.97.053112.

[83] Shaoting Lin et al. "Journal of the Mechanics and Physics of Solids Instabilities in confined elastic layers under tension: Fringe, fingering and cavitation". In: *Journal of the Mechanics and Physics of Solids* 106 (2017), pp. 229–256. DOI: 10.1016/j.jmps.2017.05.011.

[84] Jonathan B. Estrada et al. “High strain-rate soft material characterization via inertial cavitation”. In: *Journal of the Mechanics and Physics of Solids* 112 (2018), pp. 291–317. ISSN: 0022-5096. DOI: https://doi.org/10.1016/j.jmps.2017.12.006.

[85] Jin Yang, Harry C. Cramer, and Christian Franck. “Extracting non-linear viscoelastic material properties from violently-collapsing cavitation bubbles”. In: *Extreme Mechanics Letters* 39 (2020), p. 100839. ISSN: 2352-4316. DOI: https://doi.org/10.1016/j.eml.2020.100839.

[86] Emil-Alexandru Brujan et al. “Dynamics of laser-induced cavitation bubbles near an elastic boundary”. In: *Journal of Fluid Mechanics* 433 (2001), pp. 251–281. DOI: 10.1017/S0022112000003347.

[87] Eric Johnsen and Tim Colonius. “Numerical simulations of non-spherical bubble collapse”. In: *Journal of Fluid Mechanics* 629 (2009), pp. 231–262. DOI: 10.1017/S0022112009006351.

[88] Outi Supponen et al. “Shock waves from nonspherical cavitation bubbles”. In: *Phys. Rev. Fluids* 2 (9 Sept. 2017), p. 093601. DOI: 10.1103/PhysRevFluids.2.093601.

[89] B. Saintyves, O. Dauchot, and E. Bouchaud. “Bulk Elastic Fingering Instability in Hele-Shaw Cells”. In: *Phys. Rev. Lett.* 111 (4 July 2013), p. 047801. DOI: 10.1103/PhysRevLett.111.047801.

[90] S. Mora and M. Manna. “Saffman-Taylor instability of viscoelastic fluids: From viscous fingering to elastic fractures”. In: *Phys. Rev. E* 81 (2 Feb. 2010), p. 026305. DOI: 10.1103/PhysRevE.81.026305.

[91] R. Radovitzky and M. Ortiz. “Lagrangian Finite Element Analaysis of Newtonian Fluid Flows”. In: *ijnme* (1998), pp. 607–619. DOI: 10.1002/(SICI)1097-0207(19981030)43:4<607::AID-NME399>3.0.CO;2-N.

[92] G. B. Whitham. *Linear and Nonlinear waves*. John Wiley and Sons, Inc, 1974.

[93] Grigory Isaakovich Barenblatt. *Scaling*. Cambridge Texts in Applied Mathematics. Cambridge University Press, 2003. DOI: 10.1017/CBO9780511814921.

[94] G. Ben-Dor. *Shock Wave Reflection Phenomena*. Berlin: Springer, 2007.

[95] Rohan Abeyaratne. "An admissibility condition for equilibrium shocks in finite elasticity". In: *Journal of Elasticity* 2 (July 1983). DOI: 10.1007/BF00041234.

[96] Qiang Zhang and Mary Jane Graham. "A numerical study of Richtmyer-Meshkov instability driven by cylindrical shocks". In: *Physics of Fluids* 10.4 (1998), pp. 974–992. DOI: 10.1063/1.869624.

[97] Michael Ortiz, Bernd Schmidt, and Ulisse Stefanelli. "A variational approach to Navier–Stokes". In: *Nonlinearity* 31.12 (Nov. 2018), pp. 5664–5682. DOI: 10.1088/1361-6544/aae722.

[98] R. Radovitzky and M. Ortiz. "Error estimation and adaptive meshing in strongly nonlinear dynamic problems". In: *Computer Methods in Applied Mechanics and Engineering* 172.1–4 (1999), pp. 203–240. DOI: 10.1016/S0045-7825(98)00230-8.

[99] J.E. Marsden and T.J.R. Hughes. *Mathematical foundations of elasticity*. Dover Publications, 1994.

[100] M. E. Gurtin, E. Fried, and L. Anand. *The Mechanics and Thermodynamics of Continua*. Cambridge University Press, 2010.

[101] Pooya Movahed et al. "Cavitation-induced damage of soft materials by focused ultrasound bursts: A fracture-based bubble dynamics model". In: *The Journal of the Acoustical Society of America* 140.2 (2016), pp. 1374–1386. DOI: 10.1121/1.4961364.

[102] Jin Yang et al. "Probing Inertial Cavitation Damage in Viscoelastic Hydrogels Using Dynamic Bubble Pairs". In: *Dynamic Behavior of Materials, Volume 1*. Ed. by Steven Mates and Veronica Eliasson. Cham: Springer International Publishing, 2022, pp. 47–52. ISBN: 978-3-030-86562-7.

[103] Joseph B. Keller and Michael Miksis. "Bubble oscillations of large amplitude". In: *The Journal of the Acoustical Society of America* 68.2 (1980), pp. 628–633. DOI: 10.1121/1.384720.

[104] Michel Versluis et al. "How Snapping Shrimp Snap: Through Cavitating Bubbles". In: *Science* 289.5487 (2000), pp. 2114–2117. ISSN: 00368075, 10959203.

[105] Xinmai Yang and Charles C. Church. "A model for the dynamics of gas bubbles in soft tissue". In: *The Journal of the Acoustical Society of America* 118.6 (2005), pp. 3595–3606. DOI: 10.1121/1.2118307.

[106] Yuan-Hui Li. "Equation of state of water and sea water". In: *Journal of Geophysical Research (1896-1977)* 72.10 (1967), pp. 2665–2678. DOI: https://doi.org/10.1029/JZ072i010p02665. eprint: https://agupubs.onlinelibrary.wiley.com/doi/pdf/10.1029/JZ072i010p02665.

[107] S. Mora et al. "Surface instability of soft solids under strain". In: *Soft Matter* 7.22 (2011), pp. 10612–10619. DOI: 10.1039/c1sm06051a.

[108] P. Ciarletta. "Wrinkle-to-fold transition in soft layers under equi-biaxial strain: A weakly nonlinear analysis". In: *Journal of the Mechanics and Physics of Solids* 73 (2014), pp. 118–133. DOI: 10.1016/j.jmps.2014.09.001.

[109] Shaoting Lin et al. "Material-stiffening suppresses elastic fingering and fringe instabilities". In: *International Journal of Solids and Structures* 139-140 (2018), pp. 96–104. ISSN: 00207683. DOI: 10.1016/j.ijsolstr.2018.01.022.

[110] John S. Biggins and L. Mahadevan. "Meniscus instabilities in thin elastic layers". In: *Soft Matter* 14 (37 2018), pp. 7680–7689. DOI: 10.1039/C8SM01033A.

[111] The **ΣMIT** Development Group. ***ΣMIT**, A scalable computational framework for large-scale simulation of complex mechanical response of materials*. 2021.

[112] Klaus-Jürgen Bathe. *Finite Element Procedures*. New Jersey: Prentice Hall, 1996.

[113] O. C. Zienkiewicz and R. L. Taylor. *The Finite Element method, 4th edn.* New York: McGraw-Hill, 1994.

[114] K J Bathe. *Finite Element Procedures*. Prentice Hall, Pearson Education, Inc, 2014.

[115] C. Kane et al. "Variational integrators and the Newmark algorithm for conservative and dissipative mechanical systems". In: *International Journal for Numerical Methods in Engineering* 49.10 (2000), pp. 1295–1325. DOI: 10.1002/1097-0207(20001210)49:10<1295::AID-NME993>3.0.CO;2-W.

[116] A. Lew, R. Radovitzky, and M. Ortiz. "An artificial-viscosity method for the lagrangian analysis of shocks in solids with strength on unstructured, arbitrary-order tetrahedral meshes". In: *Journal of Computer-Aided Materials Design* 8.2-3 (2001), pp. 213–231. DOI: 10.1023/A:1020064403005.

[117] VonNeumann, J. and Richtmyer, R.D. "A method for the numerical calculation of hydrodynamic shocks". In: *Journal of Applied Physics* 21 (1950), pp. 232–237.

[118] Brandon Talamini, Yunwei Mao, and Lallit Anand. "Progressive damage and rupture in polymers". In: *Journal of the Mechanics and Physics of Solids* 111 (2018), pp. 434–457. ISSN: 0022-5096. DOI: https://doi.org/10.1016/j.jmps.2017.11.013.

[119] Bianca Giovanardi, Anna Scotti, and Luca Formaggia. "A hybrid XFEM - Phase field (Xfield) method for crack propagation in brittle elastic materials". In: *Computer Methods in Applied Mechanics and Engineering* 320 (2017), pp. 396–420. DOI: 10.1016/j.cma.2017.03.039.

[120] S. Balay et al. *PETSc Users Manual*. Tech. rep. ANL-95/11 - Revision 3.7. Argonne National Laboratory, 2016.

[121] Weinberg, K. and Ortiz, M. "Shock Wave Induced Damage in Kidney Tissue". In: *Computational Materials Science* 32.3–4 (2005), pp. 588–593. DOI: 10.1016/j.commatsci.2004.09.005.

[122] M. Shane Hutson and Xiaoyan Ma. "Plasma and Cavitation Dynamics during Pulsed Laser Microsurgery in vivo". In: *Phys. Rev. Lett.* 99 (15 Oct. 2007), p. 158104. DOI: 10.1103/PhysRevLett.99.158104.

[123] K. Jach et al. "2D MHD simulation of spontaneous magnetic fields generated during interaction of 1315.2-nm laser radiation with copper slabs at 1016 W/cm2". In: *Physics of Plasmas* 28.9 (2021), p. 092704. DOI: 10.1063/5.0054283.

[124] I. Akhatov et al. "Collapse and rebound of a laser-induced cavitation bubble". In: *Physics of Fluids* 13.10 (2001), pp. 2805–2819. DOI: 10.1063/1.1401810.

[125] Werner Lauterborn. "Numerical investigation of nonlinear oscillations of gas bubbles in liquids". In: *The Journal of the Acoustical Society of America* 59.2 (1976), pp. 283–293. DOI: 10.1121/1.380884.

[126] C. Geuzaine and J.-F. Remacle. "Gmsh: a three-dimensional finite element mesh generator with built-in pre- and post-processing facilities". In: *International Journal for Numerical Methods in Engineering* 79.11 (2009), pp. 1309–1331. DOI: 10.1002/nme.2579.

[127] J.M. Ball. "Discontinuous equilibrium solutions and cavitation in nonlinear elasticity". In: *Philosophical Transactions in the Royal Society A* 306 (1496 1982), pp. 557–611. DOI: 10.1098/rsta.1982.0095.

[128] Christopher W. Barney et al. "Cavitation in soft matter". In: *Proceedings of the National Academy of Sciences* 117.17 (2020), pp. 9157–9165. DOI: 10.1073/pnas.1920168117. eprint: https://www.pnas.org/doi/pdf/10.1073/pnas.1920168117.

[129] James E. Lingeman. "Extracorporeal Shock Wave Lithotropsy: Development, Instrumentation, and Current Status". In: *Urologic Clinics of North America* 24.1 (1997), pp. 185–211. ISSN: 0094-0143. DOI: https://doi.org/10.1016/S0094-0143(05)70363-3.

[130] Michael Bailey et al. “Progress in Lithotripsy Research”. In: *Acoustics Today* 2 (Apr. 2006). DOI: 10.1121/1.2961131.

[131] Theodore J. Dubinsky et al. “Histotripsy: The Next Generation of High-Intensity Focused Ultrasound for Focal Prostate Cancer Therapy”. In: *Journal of Ultrasound in Medicine* 39.6 (2020), pp. 1057–1067. DOI: https://doi.org/10.1002/jum.15191. eprint: https://onlinelibrary.wiley.com/doi/pdf/10.1002/jum.15191.

[132] Alissa Hendricks-Wenger et al. “Histotripsy Ablation in Preclinical Animal Models of Cancer and Spontaneous Tumors in Veterinary Patients: A Review”. In: *IEEE Transactions on Ultrasonics, Ferroelectrics, and Frequency Control* 69.1 (2022), pp. 5–26. DOI: 10.1109/TUFFC.2021.3110083.

[133] Alissa Hendricks-Wenger et al. “Immunological Effects of Histotripsy for Cancer Therapy”. In: *Frontiers in Oncology* 11 (2021). ISSN: 2234-943X. DOI: 10.3389/fonc.2021.681629.

[134] Franck C. “Microcavitation: the key to modeling blast traumatic brain injury?” In: *Concussion* (2017). DOI: 10.2217/cnc-2017-0011.

[135] A. Jean et al. “An animal-to-human scaling law for blast-induced traumatic brain injury risk assessment”. In: *Proceedings of the National Academy of Sciences of the United States of America* 111 (43 2014), pp. 15310–15315. DOI: 10.1073/pnas.1415743111.

[136] Cummings J. et al. “A virtual test facility for the simulation of dynamic response in materials”. In: *Journal of Supercomputing* 23 (2002), pp. 39–50. DOI: 10.1023/A:1015733102520.

[137] G.I. Barenblatt. “The mathematical theory of equilibrium cracks in brittle fracture”. In: *Advances in Applied Mechanics* 7 (1962), pp. 55–129. DOI: 10.1016/S0065-2156(08)70121-2.

[138] N. K.-R. Kevlahan. “The vorticity jump across a shock in a non-uniform flow”. In: *Journal of Fluid Mechanics* 341 (1997), pp. 371–384. DOI: 10.1017/S0022112097005752.